Physics Department. Annual progress report 1 January - 31 December 1990

Als-Nielsen, Jens Aage; Pedersen, J.S.; Lebech, Bente

Publication date:
1991

Document Version
Publisher's PDF, also known as Version of record

RISØ

Riso-R-582

Physics Department Annual Progress Report 1 January – 31 December 1990

Edited by J. Als-Nielsen, J. Skov Pedersen and B. Lebech

Risø National Laboratory, DK-4000 Roskilde, Denmark
January 1991

RISØ-R-582

PHYSICS DEPARTMENT ANNUAL PROGRESS REPORT

1 January - 31 December 1990

edited by J. Als-Nielsen, J. Skov Pedersen and B. Lebech

Abstract

Research in the Physics Department covers the field of condensed matter physics. The principal activities of the department are presented in this Progress Report covering the period from 1 January to 31 December 1990.

The condensed matter physics research is predominantly experimental utilising diffraction of neutrons and X-rays. The research topics range from studies of two- and three-dimensional structures, magnetic ordering, heavy fermions, phase transitions in model systems to studies of texture and recrystallization kinetics and with a more applied nature. The discovery of the high T_c superconductors in 1986 has opened an important new research area, where neutron and X-ray diffraction are used to elucidate the basic mechanism responsible for the superconductivity and in the analysis of the solid state syntheses used when producing the materials.

January 1991

Risø National Laboratory, DK-4000 Roskilde, Denmark

This report contains unpublished results and should not be quoted without permission from the authors.

ISBN 87-550-1703-7
ISSN 0106-2840
ISSN 0107-8348

Grafisk Service Risø, 1991

Contents

1 INTRODUCTION 7

1.1 Nuclear Order in Copper: New Type of Antiferromagnetism in an Ideal fcc System . . . 8

1.2 Neutron Diffraction on K_3PdD_3 . . . 10

1.3 The Magnetic Structure of $CsCo_2S_2$ and $TlCo_2S_2$ . . . 12

1.4 Neutron Powder Diffraction in Rare Earth Dimer Compounds $Cs_3R_2X_9$ (X = Cl, Br, I) . . . 14

1.5 Crystal and Magnetic Structure of $KMnCl_3$ . . . 15

1.6 Weak Ferromagnetism and Crystal Structure of Layered Perovskites Studied by Neutron Diffraction . . . 17

1.7 The Vortex Lattice of Superconducting UPt_3 Studied by SANS . . . 19

1.8 Commensurate–Incommensurate Magnetic Phase Transitions in dhcp Neodymium Metal and Nd-Pr Metal Alloys . . . 21

1.9 Neutron Diffraction Studies of the Magnetic Structure of Er – Y Alloys in Applied Magnetic Fields . . . 23

1.10 Neutron Diffraction Studies of the Magnetic Structure of Er under the Influence of Hydrostatic Pressure . . . 25

1.11 Magnetic Structures of the Rare Earth Alloy HoEr . . . 27

1.12 Magnetic X-ray Scattering Studies of a HoEr Alloy . . . 28

1.13 Investigations of Systems Containing Very Short Hydrogen Bonds . . . 29

1.14 NiAs Type Related Phases in the Ni-Ga-As System . . . 31

1.15 Structural Investigation of $NaCr_3O_8$ and $LaMnO_3$ Using Neutron Powder Diffraction . . . 32

1.16 Superconducting Cuprates and Related Compounds . . . 33

1.17 Incommensurate Inelastic Neutron Scattering from $La_{1.9}Sr_{0.1}CuO_4$ . . . 34

1.18 The Crystal Structure of $Pb_2Sr_2HoCu_3O_8$ Studied by Neutron Powder Diffraction . . . 36

1.19 A Study of Structural Properties, Thermopowder and Superconductivity of $Nd_{1.85}Ce_{0.15}CuO_{4+\delta}$ . . . 37

1.20 Structural and Thermodynamic Properties of Oxygen Ordering in $YBa_2Cu_3O_{6+x}$ . . . 39

1.21 A Model of the Static and Dynamic Relationships between Oxygen Ordering and Superconductivity in $YBa_2Cu_3O_{6+x}$ . . . 41

1.22 Magnetic Correlations in Superconducting $YBa_2Cu_3O_{6+x}$ . . . 43

1.23 Preparation of High-T_c Superconductors by RF Sputtering . . . 45

1.24 Measurement of Texture in YBCO Thin Films . . . 46

1.25 Melting, Growth and Faceting of Lead Precipitates in Aluminium . . . 47

1.26 Sputtering Yields and Energy Distributions from Ion-Bombarded Condensed Gases . . . 49

1.27 Luminescence from Pure and Impure Solid Hydrogens during Electron Bombardment . . . 50

1.28 Two Dimensional Solids and Liquids Influenced by a Small Corrugation Potential: A Monte Carlo Simulation Study . . . 51

1.29 Large Corrugation Potential Effect on Two Dimensional Solids and Liquids: A Continous Monte Carlo Simulation Study towards the Potts Model . . . 52
1.30 Pinning Effects on Domain Growth Kinetics . . . 53
1.31 A Symmetry Principle for Epitaxial Rotation . . . 54
1.32 Numerical Simulations of Crystalline Epitaxy . . . 55
1.33 Cu/Si(111) 5.6×5.6: A Silicide Precursor . . . 56
1.34 Epitaxial Rotations of Metastable Clusters of Pb on Si(111) and Ge(111) . 57
1.35 Pb/Si(111): A Liquid Pb Monolayer at Room Temperature . . . 58
1.36 Chemisorption of Oxygen on Cu(110): The $c6 \times 2$ Structure . . . 59
1.37 Chemisorption of Oxygen on Cu(111) . . . 61
1.38 The structure of Sulphur on Cu(111) . . . 62
1.39 X-ray Reflectivity of Free-standing Smectic Films . . . 63
1.40 Structural Properties of DPPC in a Monolayer at the Air/Water Interface: A Neutron Reflectivity Study . . . 65
1.41 Grazing Incidence X-Ray Diffraction Measurements on Uncompressed Monolayers of Long Chain Alcohols and Carboxylic Acids Relevance to Ice Nucleation . . . 67
1.42 Grazing Incidence X-Ray Diffraction of Cadmium Arachidate Monolayers at 9 °C over Water in the Uncompressed State. Evidence in Favour of an Ordered Cadmium Layer . . . 69
1.43 Effect of Solvent on Growth and Dissolution of Ordered Monolayers at Air-Solutions Interfaces . . . 71
1.44 Crystalline Phases in Fatty Acid Monolayers on Water . . . 73
1.45 The Prediction of the 3-Dimensional Structure of Protein Backbones by Neural Network and a Novel Folding Routine . . . 75
1.46 Small Angle Scattering Studies on Coated Vesicles . . . 76
1.47 Kinetics of Urea-Induced Dissociation of Human Plasma α_2-Macroglobulin 77
1.48 Solution Structure and Interaction of Thiol-Ester Proteins . . . 78
1.49 Studies on Humic Acid Structure and Metal Ion Binding under Various Environmental Conditions . . . 79
1.50 Evolution of the Structure of Bicontinous Microemulsion . . . 80
1.51 Effect of Alcohols on the Properties of Micellar Systems . . . 81
1.52 Small-Angle Scattering of Poly(Vinylchloride) . . . 82
1.53 Ordered Phases in Block-Co-Polymer Melts . . . 83
1.54 Structural Studies of the Aggregation of Co-Block-Copolymers in Aqueous Solution . . . 84
1.55 Small Angle Neutron Scattering Study of PDMS Gels Cross-linked by Electron Irradiation and Swollen to Equilibrium . . . 85
1.56 Structural and Thermal Studies of Silica Aerogel . . . 87
1.57 A Comparison of Results from SANS, PAT and TEM for Bulk Cu Containing Krypton During Isochronal Annealing . . . 90
1.58 Cavity Growth Rates in Fatigued Copper . . . 92
1.59 Results of Flux and Resolution Function Calculation for SAXS Setups Using the Gaussian Formulation of Phase-Space Analysis . . . 94
1.60 Beam Deflection in Laue and Bragg Monochromator Geometries . . . 96
1.61 A Synthtetic Multilayer Crystal-Mirror Beam Deflector . . . 98

1.62 The Liquid Surface Neutron Reflectometer at Risø 100
1.63 Intensity versus Resolution. A Comparison between the "Symmetrical" and "Asymmetrical" SANS Spectrometers 102
1.64 In Situ X-ray Diffraction Experiments on Copper Containing Catalyst Samples 104
1.65 The Growth of Pb on MgO(100) 105
1.66 The Liquid He Plant 106

2 PARTICIPANS IN THE WORK IN THE DEPARTMENT 107

3 PUBLICATIONS AND EDUCATIONAL ACTIVITIES IN THE DEPARTMENT 110
3.1 Publications 110
3.2 Conferences 116
3.3 Lectures 122
3.4 Organization of Conferences, Schools 124

1 INTRODUCTION

The condensed matters physics research is predominantly experimental utilising diffraction of neutrons and X-rays. The neutron scattering experiments are carried out at the DR3 reactor, where the Physics Department operates seven spectrometers, including a small angle neutron scattering facility. The experiments using synchrotron X-ray radiation take place at HASY-laboratory, at DESY in Hamburg, Germany.

Neutron and X-ray diffraction are complementary techniques. The neutron has several unique properties. It can penetrate matter; the energies of neutrons are comparable to that of typical excitations in condensed matter, and so the neutron can probe such excitations. In scattering experiments, the neutron is sensitive to the magnetic moments of atoms and to nuclear isotopes and at ultralow temperatures the neutron can even be used to determine the orientation of nuclear spins. The main advantage of X-ray diffraction in our research program stems from the astounding X-ray intensity one can obtain from synchrotron sources. This allows an improvement of resolution in diffraction experiments by several orders of magnitude over possibilities with neutron scattering, and/or a minute volume of the diffracting sample such as a single atomic or molecular layer on a surface.

The research topics described in this report cover studies of two- and three-dimensional structures, magnetic ordering, heavy fermions, phase transitions in model systems, studies of high T_c superconductivity and studies of inorganic and biological materials by small angle scattering.

1.1 Nuclear Order in Copper: New Type of Antiferromagnetism in an Ideal fcc System

(A.J. Annila, O.V. Lounasmaa, A.S. Oja and J.T. Tuoriniemi, *Low Temperature Laboratory, Helsinki University of Technology, Espoo, Finland*, K.N. Clausen and P.-A. Lindgård, *Physics Department, Risø National Laboratory, Denmark*, K. Siemensmeyer, M. Steiner, *Johannes Gutenberg Universität, Mainz, Germany*, and H. Weinfurter, *Hahn-Meitner Institute, Berlin, Germany*)

In the first neutron diffraction experiments[1] on copper, the nuclear antiferromagnetic (100) Bragg peak, X (see Fig. 1), was observed in two regions of the external magnetic field, applied along the $[01\bar{1}]$ crystalline direction: near zero field and around 0.15 mT. It was puzzling that no neutron intensity was found at intermediate fields around $B = 0.10$ mT, even though the simultaneously measured longitudinal susceptibility indicated order. The interpretation is that the spin structure at intermediate fields is characterized by a yet unknown propagation vector.

On the basis of first principles calculations[2] it has been shown that the fundamental ordering vector is expected at X corresponding to the observed (100) reflection. Another vector along ΓK, $(0\eta\eta)$ (see Fig. 1), is very close in energy, in particular if the strength of the Rudermann-Kittel interaction relative to the dipolar force is slightly reduced from the experimental value. Fluctuations could stabilize a ΓK structure at the boundary between the two (100) phases.

We attempted to find this possible new reflection. The extremely low nuclear ordering temperature (58 nK) in copper imposes severe experimental restrictions which make it difficult to use conventional $\omega - 2\theta$ scans, traditionally employed in similar investigations of electronic magnetism at higher temperatures. Only scans along small sections of selected lines in reciprocal space, could be performed during the warm-up of the sample.

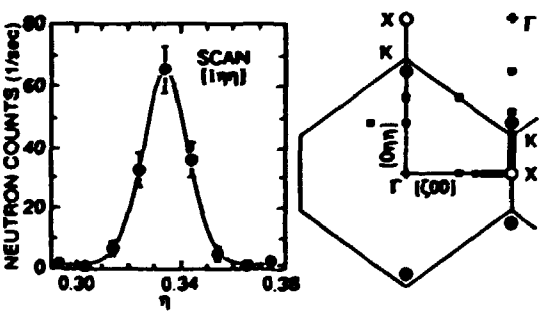

Fig. 1. Left: Neutron intensity vs. position along ΓK, $[1\eta\eta]$, showing the discovery of the $(1\frac{1}{3}\frac{1}{3})$ Bragg reflection. Right: The scattering plane in the Brillouin zone of an fcc lattice. The search scans are marked with thick lines, the observed $\pm(0\frac{2}{3}\frac{2}{3}),(1\frac{1}{3}\frac{1}{3})$ and $(1-\frac{1}{3}-\frac{1}{3})$ reflections by • and the (100)-type reflections by ○. No intensity was observed at the commensurate positions indicated by ■.

The intervals of the high symmetry lines and some additional commensurate points which were investigated are shown in Fig. 1: the search scans were performed at $B = 0$ and $B \approx 0.8$ mT.

Our search for a new reflection was rewarded when a very clear Bragg peak was found at $(1\eta\eta)$, with $\eta = 0.33 \pm 0.01$, in the external field $B = 0.07$ mT (see Fig. 1). The order is, within the experimental accuracy, commensurate with the lattice structure. Later the equivalent $\pm(0\frac{2}{3}\frac{2}{3})$ and $(1 - \frac{1}{3} - \frac{1}{3})$ reflections were observed as well.

The commensurate ordering vector $(0\frac{2}{3}\frac{2}{3})$, has not previously been observed in any electronic fcc antiferromagnet.

[1] T.A. Jyrkkiö, M.T. Huiku, O.V. Lounasmaa, K. Siemensmeyer, K. Kakurai, M. Steiner, K.N. Clausen, and J.K. Kjems, (1988). Phys. Rev. Lett. **60**, 2418.
[2] P.-A. Lindgård, X.-W. Wang, and B.N. Harmon, (1986). J. Magn. & Magn.Mater. **54-57**, 1052.

1.2 Neutron Diffraction on K_3PdD_3

(W. Bronger, G. Auffermann, and P. Müller, *Institut für Anorganische Chemie der RWTH Aachen, Germany* and K.N. Clausen, *Physics Department, Riso National Laboratory, Denmark*)

The ternary hydride K_3PdH_3 has been synthesized by the reaction of potassium hydride with a palladium sponge in a pure hydrogen atmosphere at a temperature of 620 K. The reaction product is yellow and extremely sensitive to moisture and air.

The structure was derived from X-ray investigations on powdered samples and from a neutron diffraction experiment on the deuterated compound[1]. Investigations led to a tetragonal unit cell (space group $P4_2/mnm$, $Z=8$). The structure contains two differently bonded types of hydrogen atoms, the one forming isolated linear $[PdD_2]^{2-}$ - groups similiar to those we found in Na_2PdH_2 [2], whereas the other hydrogen atoms are octahedrally surrounded by six potassium atoms in the same manner as in potassium hydride. The structure of K_3PdD_3 is shown in Fig. 1.

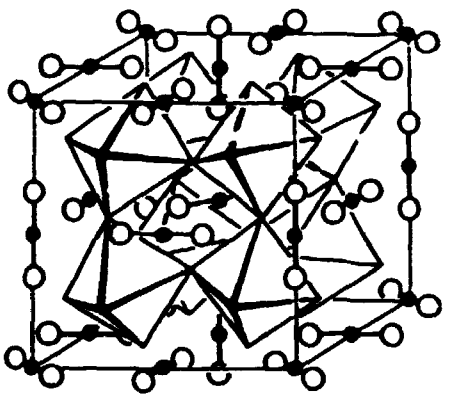

Fig. 1. K_3PdD_3; the structure of the tetragonal low temperature modification, representation of the linear $[PdD_2]^{2-}$-dumbbells and the corner-sharing potassium octahedra centered by deuterium ions.

Table: K_3PdD_3 : atomic parameters of the tetragonal low temperature modification at 295 K.
a=10.700(8) Å c=10.535(9) Å

Pd1(2a)		
Pd2(2b)		
Pd3(4c)		
K1(4f)	x=0.300(7)	
K2(4g)	x=0.300(7)	
K3(16k)	x=0 y=0.250(3)	z=0.197(3)
D1(8j)	z=$\frac{1}{4}$	
D2(4f)	x=0.111(3)	
D3(4e)	z=0.340(5)	
D4(8i)	x=0.843(4) y=$\frac{1}{2}$	

$B_{overall}$ = 3.0 Å^2, R-value: 0.14

X-ray investigations at higher temperatures show a reversible phase transition. Above 500 K K_3PdH_3 becomes cubic (space group Pm3m: a=5.410(1) Å; Z=1). The transition is caused by the movements of the $[PdH_2]^{2-}$ groups, which cancel the tilts of the hydride ion centered potassium octahedra in the low temperature modification (Fig. 2).

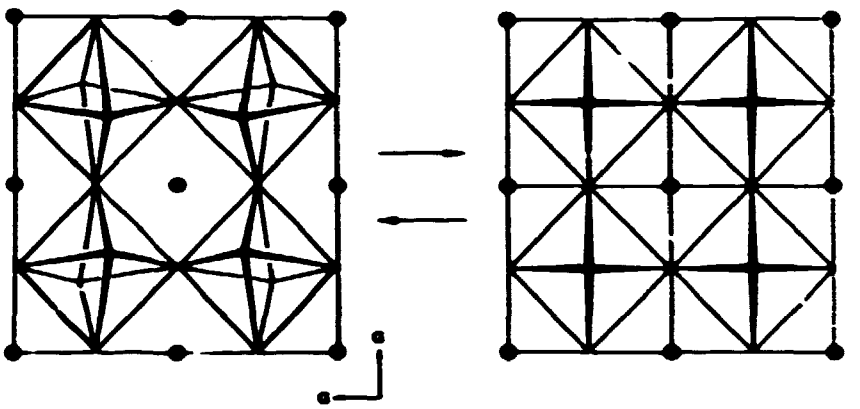

Fig. 2 K_3PdD_3: atomic arrangement of the potassium octahedra and the palladium atoms in the tetragonal low temperature modification (left) and in the cubic high temperature modification (right).

[1] W. Bronger, and G. Auffermann, (1990). Journal Less Common Met. **158**, 163.
[2] D. Noréus, K. Törnroos, A. Börje, T. Szabó, W. Bronger, H. Spittank, G. Auffermann, and P. Müller, (1988). Journal Less Common Met. **139**, 233.

1.3 The Magnetic Structure of $CsCo_2S_2$ and $TlCo_2S_2$

(C. Bomba, W. Bronger, P. Müller, *Institut für Anorganische Chemie der RWTH, Aachen, Germany*, and K. N. Clausen, *Physics Department, Risø National Laboratory, Denmark*)

The series of compounds ACo_2X_2 with A = K,Rb or Cs and X = S or Se has been prepared by reacting alkali metal carbonate with a cobalt sponge and sulphur in a hydrogen atmosphere at 950 K [1]. $TlCo_2S_2$ was synthezised by the reaction of Tl_2S with a cobalt sponge and sulphur at 600 K. The structure of these compounds is characterized by sheets of edge-sharing $[CoS_4]$ - tetrahedra. The alkaline or thallium atoms are separating these layers (*cf.* Fig. 1). Measurements of the conductivity of $CsCo_2S_2$ showed that it is metallic (resistivity at room temperature 3×10^{-2} Ωcm). Susceptibility data revealed ferromagnetism below 70 K. The paramagnetic moment was determined to be 2.21 μ_B.

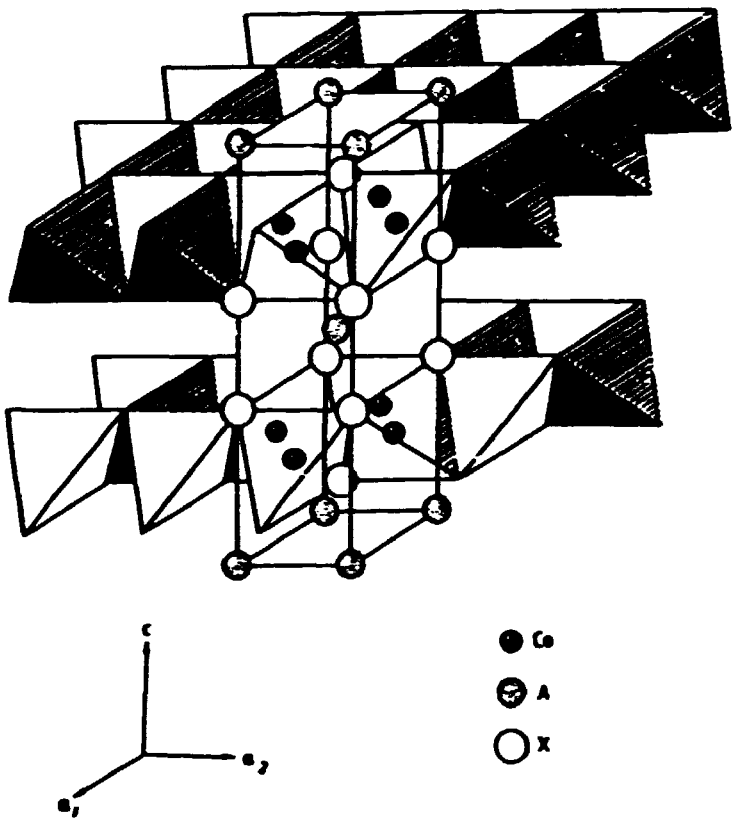

Fig. 1: Atomic arrangement of ACo_2X_2.

Neutron diffraction experiments on $CsCo_2S_2$ and $TlCo_2S_2$ at room temperature and 9.5 K (16 K) showed weak magnetic intensities in some reflections due to ferromagnetic ordering. The results of the Rietveld refinements are shown in table 1. The magnetic moments are aligned in the $a - b$– plane. Due to the tetragonal symmetry the direction can not be determined using powdered samples.

Table 1: Results of Rietveld refinement on $CsCo_2S_2$ and $TlCo_2S_2$ (Space group I4/mmm; A in 2a, Co in 4d, S in 4e).

Compound	$CsCo_2S_2$		$TlCo_2S_2$	
Temperature [K]	295	9.5	295	16
λ [Å]	2.0094	2.0094	2.395	2.395
a [Å]	3.796(1)	3.782(1)	3.7480(3)	3.7425(6)
c [Å]	14.042(5)	13.948(5)	12.982(2)	12.895(3)
z_S	0.338(1)	0.341(1)	0.3463(8)	0.348(1)
B_A [Å^2]	3.5(5)	2.2(5)	2.4(3)	
B_{Co} [Å^2]	2.1(5)	0.3(5)	0.2(3)	
B_S [Å^2]	1.2(4)	0.7(4)	1.8(3)	
$B_{overall}$ [Å^2]				1.2(3)
μ [μ_B]		0.62(5)		0.3(1)
R_{nuc}	5.1	5.1	2.4	4.7
R_{mag}		13.2		16.2
R_{prof}	27.5	28.9	7.1	11.6

[1] C. Bomba, Thesis, RWTH Aachen, (1989).

1.4 Neutron Powder Diffraction in Rare Earth Dimer Compounds $Cs_3R_2X_9$ (X = Cl, Br, I)

(L. Keller, A. Dönni, P. Fischer, *Laboratory for Neutron Scattering, ETH Zürich, Switzerland*, and B. Lebech *Physics Department, Risø National Laboratory, Denmark*)

Compounds of the general composition $Cs_3R_2X_9$ (R = rare earth, X = Cl, Br) have only recently become available for investigations. The compounds crystallize in the trigonal space group $R\bar{3}c$ with $Z = 6$[1]. The structure contains the dimeric units $R_2X_9^{3-}$, which are built up of two face-sharing RX_6^{3-} octahedra as illustrated in the figure below. Powder neutron diffraction data were collected at room temperature for $Cs_3Yb_2Br_9$ and $Cs_3Yb_2Cl_9$, and at 4.8 K for the highly neutron absorbing $Cs_3Dy_2Br_9$ compound using incident neutrons of wavelength 1.113 Å. The diffraction patterns were analyzed using a modified version of the computer programme (DBW3.2S)[2] and the results have been summarized by Keller[3].

For $Cs_3R_2Br_9$ (R = Tb, Ho, Er) the resulting rare earth - rare earth (d_{R-R}) and rare earth - bromide (d_{R-X}) intra dimeric distances confirmed the empirical law[4]:

$$d_{R-R} = 2 \cdot I_X \text{ and } d_{R-X} = I_R + I_X,$$

where I_R and I_X refer to the ionic radii of the rare earth and the bromide, respectively.

$Cs_3Dy_2I_9$ crystallizes in the hexagonal space group $P6_3/mmc$ and is expected to order magnetically below 1.6 K. Using a triple-axis diffractometer in the elastic mode and incident neutrons of 4 or 2 Å, an attempt was made to detect magnetic ordering in $Cs_3Dy_2I_9$. No magnetic Bragg peaks were observed when comparing the spectra observed at 1.6 and 0.6 K indicating that $Cs_3Dy_2I_9$ remains paramagnetic down to 0.6 K.

[1] G. Meyer and A. Schönemund, (1980). Mat. Res. Bull. **15**, 89.
[2] D.B. Wiles and R. A. Young, (1981). J. Appl. Cryst **14**, 149.
[3] L. Keller, (1990). LNS report 153, Laboratory for Neutron Scattering ETH Zürich.
[4] A. Dönni, A. Furrer and H.U. Güdel, (1989). J. Solid State Chem. **81**, 278.

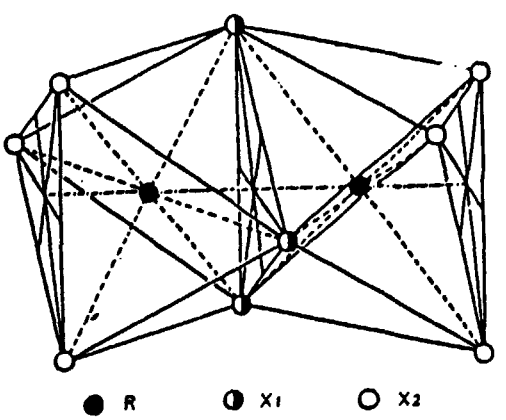

The structure of the dimeric unit $R_2X_9^{3-}$. The R-R direction is parallel to the c-axis of the hexagonal cell.

1.5 Crystal and Magnetic Structure of $KMnCl_3$

(P. Harris, S. Larsen, *Chemistry Department, University of Copenhagen, Denmark*, and B. Lebech, *Physics Department, Risø National Laboratory, Denmark*)

At room-temperature $KMnCl_3$ can exist in two different crystal forms: α-$KMnCl_3$ and β-$KMnCl_3$. Both crystallize in the space group Pnma[1] with cell dimensions $a = 7.08$ Å, $b = 9.97$ Å and $c = 6.98$ Å in the α–phase and $a = 8.77$ Å, $b = 3.88$ Å and $c = 14.42$ Å in the β–phase. There is no simple transformation between the two structures.

Based on measurements of optical luminescence on a large, almost cylindrical (diameter $\sim$ 5.6 mm, length $\sim$5.2 mm) single crystal of $KMnCl_3$, Pawlowska *et al.*[2] suggested that in the single crystal, the structure might be a mixture of α– and β-$KMnCl_3$ in an incommensurate composite structure instead of just one of the two Pnma forms. Such a composite structure would give rise to nuclear satellite Bragg reflections in a diffraction experiment. Furthermore, it is known from neutron powder diffraction experiments[3] that α-$KMnCl_3$ orders magnetically at 102 K into a simple antiferromagnetic structure. The magnetic moment determined from the powder data is 4.6(5) μ_B, but the direction of the moment was not determined. β-$KMnCl_3$ orders magnetically at 2.1 K. In this case, the magnetic structure is a spiral propagating along the b–axis with a repeat distance of 3.17 *b*. The magnetic moment in the β–phase is 3.8(2) μ_B.

In order to search for evidence for the possible incommensurate composite structure and its magnetic structure, a neutron diffraction study was performed on the same crystal as used for the optical measurements. Neutron diffraction data were collected at three temperatures (300, 110 and 10 K) using a four-circle diffractometer. All three data sets show reflections from α-$KMnCl_3$ only. No trace of either β-$KMnCl_3$ or an incommensurate phase was found.

The analysis of the diffraction data was complicated by two experimental observations: **(1)** many reflections were split and **(2)** several reflections, which are systematically absent in the Pnma space group, were present. In the Pnma space group, the $(0kl)$ $(k+l = 2n+1)$ and $(hk0)$ $(h = 2n + 1)$ reflections should be systematically absent. However, only the $(0kl)$ $(k + l = 2n + 1, l = 2n + 1)$ and $(hk0)$ $(h = 2n + 1, h + k = 2n + 1)$ reflections were systematically absent. This is *not* in agreement with any space group. When combining the observation of split Bragg peaks with the fact that the a– and c–axes have almost equal lengths a possible interpretation of the data is that the crystal is twinned. Therefore, the data was analysed assuming a twinned model structure where the axes of the twin components were oriented as shown in Fig. 1.

The *R*-factor, which compares the observed and calculated structure factors, was rather large before the twin description was incorporated in the crystal structure refinement. At 110 K, $R(|F|) = 22$ % and $R_w(|F|) = 21$ %. where, $R(|F|)$ and $R_w(|F|)$ refer to the unweighted and weighted *R*-factors, respectively. After incorporating the twin description the corresponding *R*-factors were reduced to $R(|F|) = 12$ % and $R_w(|F|) = 8$ %. This is a significant reduction, which strongly favours the assumption of a twinned crystal. As a result of the structure refinement we therefore conclude that the investigated single crystal is single phase α-$KMnCl_3$. From the structural refinement we find that the crystal

contained about 60 % of one twin component and 40 % of the other. The cell dimensions at 110 K are $a = 7.05$ Å, $b = 9.98$ Å and $c = 7.00$ Å which agree well with the results of powder diffraction[3].

As mentioned above, α-$KMnCl_3$ undergoes a magnetic phase transition at 102 K. Below 102 K it is antiferromagnetic. Conventional $\omega - 2\theta$ scans were collected at 10 K and 110 K and the temperature dependencies of selected reflections were determined. The transition seems to be of second order and no hysteresis appears. Reflections caused by the magnetic scattering could be indexed as (hkl) $(h + l = 2n + 1,\ k = 2n + 1)$, which means that the magnetic structure is a simple antiferromagnetic structure in which each Mn^{2+} moment is antiferromagnetically coupled to its six nearest neighbours. This agrees with the conclusions from the powder data[3]. The analysis of the single crystal data shows (using the magnetic form factor for Mn^{2+} of Watson and Freeman[4]) that the magnetic moments on the Mn sites are directed along the c-axis with a magnitude of 4.0(2) μ_B.

[1] A. Horowitz, M. Amit, J. Makovsky, L. Ben Dor, and Z. H. Kalman, (1982). J. Solid State Chem. **43**, 107.
[2] M. Pawlowska, W. Streck and I. Trabjerg, (1989), unpublished.
[3] E. Gurewitz, M. Melamud and A. Horowitz, (1982). Phys. Rev. B **25**, 5220.
[4] R.E. Watson and A.J. Freeman, (1961). Acta Cryst. **14**, 27.

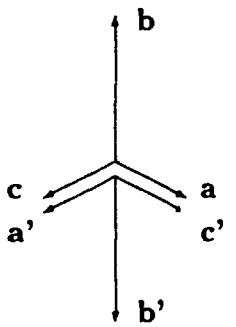

Fig. 1. Possible orientation of the crystallographic axes of the twin components (marked and unmarked, respectively) in the model structure. Because the space group is centrosymmetric, other orientations are equivalent.

1.6 Weak Ferromagnetism and Crystal Structure of Layered Perovskites Studied by Neutron Diffraction

(N. Achiwa, *Kyushu University, Fukuoka, Japan*, S. Kawano, *Kurri Research Reactor Institute, Kyoto University, Osaka, Japan* and B. Lebech, *Physics Department, Risø National Laboratory, Denmark*)

The layered perovskites $(C_nH_{2n+1}NH_3)_2MnCl_4$ with $n = 1$ (MANC), $n = 2$ (EAMC) and $n = 3$ (PAMC) are known as good examples of quasi *2-d* Heisenberg antiferromagnets with a Mn moment of $\sim 5\ \mu_B$. In PAMC and EAMC weak ferromagnetism along the a-axis has been observed and this canting of the spins is known to be caused by antisymmetric Dzyaloshinskii-Moriya exchange interactions[1]. As function of temperature, these family compounds exhibit several structural phase transitions which are related to reorientation of the alkylammonium group and tilting of $MnCl_6$ octahedra which alternately rotate about the b-axis. In order to understand the mechanisms leading to the experimentally observed weak ferromagnetism it is important to study the symmetry relation between the magnetic and the monoclinic crystal structure. It is therefore important to note that in the lowest temperature phase, the antiferromagnetic spin arrangement in all the three compounds is consistent with the chemical cell of the $MnCl_6$ octahedra, *i.e.* the antiferro-

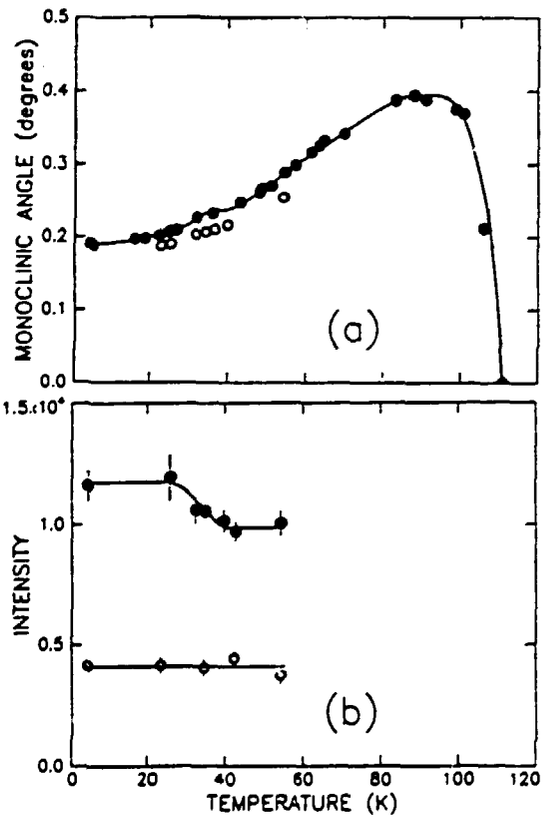

(a) *shows the temperature dependence of the mononoclinic angle α in the η-phase of PAMC.* • *and* o *indicate data collected at the Kyoto University research reactor and the DR3 reactor at Risø, respectively.* **(b)** *shows the temperature dependence of two weak satellites* (o $(0\ 1{+}\frac{1}{3}\ 5{-}\frac{1}{3})$ and • $(0\ 1{+}\frac{1}{3}\ 3{-}\frac{1}{3})$).

magnetic spin arrangement and the crystal structure have the same unit cell. If the tilting of the $MnCl_6$ octahedron and the direction of the spin can couple through an antisymmetric exchange interaction, the above mentioned symmetry relation allows the appearance of weak ferromagnetism caused by the spin canting[1].

Among the compounds, PAMC shows a commensurately modulated crystal structure in the η-phase which appears below 112.5 K. The modulation vector is $q = \frac{1}{3}\cdot(\mathbf{b}^* - \mathbf{c}^*)$ and the structure belongs to the super space group $P^{P2_1/b}(\bar{1}1)$[2]. In this phase, the positional modulation of the Mn ion and the rotational modulation of the $MnCl_6$ octahedron are expected to be the same as in the incommensurately modulated ϵ-phase of PAMC[3]. If a positional modulation of the Mn ion exits in the η-phase and magnetic ordering occurs, the magnetic Bragg reflections should be accompanied by magnetic satellites coinciding with the lattice satellites. In order to study the coupling of the magnetic and the lattice systems in the η-phase of PAMC we have initiated neutron diffraction measurements on a single crystal of PAMC. Examples of these measurements are shown in the figures; **(a)** shows the monoclinic angle as function of temperature and **(b)** the intensity variations of two weak satellites, one with a magnetic contribution (•) and one without (o). Above the Néel temperature ($T_N \sim 40$ K) the monoclinic angle α decreases with temperature, whereas the temperature dependency is less pronounced below T_N **(a)**. In fact, there seems to be a tendency of lock-in of the monoclinic angle which could be caused by the magnetic order. The data in **(b)** was used to estimate the modulated part (weak ferromagnetism) of the ordered magnetic moment. It was found to be $(0.5 \pm 0.2)\ \mu_B$. In order to make this estimate, the difference between the intensity in the $(0\ 1+\frac{1}{3}\ 5-\frac{1}{3})$ satellite at 4.2 K and 45 K was assumed to be of magnetic origin and scaled to the intensity at 4.2 K of the purely magnetic (011) reflection.

[1] N. Achiwa, T. Matsuyama and T. Yoshinari, (1990). In: Phase Transitions (in the press).
[2] W. Depmeier and S.A. Mason, (1983). Solid State Commun. **46**, 409.
[3] W. Steurer and W. Depmeier, (1988). Acta Cryst. **B45**, 555.

1.7 The Vortex Lattice of Superconducting UPt_3 Studied by SANS

(C. Broholm, R.N. Kleimann, G. Aeppli, E. Bucher, N. Stücheli, D.J. Bishop, *AT&T Bell Laboratories, Murray Hill, U.S.A.*, K.N. Clausen, B. Howard, K. Mortensen and J. Skov Pedersen, *Physics Department, Riso National Laboratory, Denmark*)

The superconducting state of UPt_3 develops from a heavy Fermion metal with renormalized electron masses, weak antiferromagnetic order and strong antiferromagnetic fluctuations. Each of these properties inhibits conventional phonon-mediated s-wave superconductivity. An alternative mechanism is the exhange of antiferromagnetic spin-fluctuations which can promote d-wave superconductivity. Two classes of experiments have shown that the superconductivity of UPt_3 indeed is different from conventional s-wave superconductivity. Firstly the temperature dependence of bulk properties in the superconducting state are not exponentially activated as is the case of s-wave superconductors. Instead, power-law temperature dependences are found which indicate the existence of nodes in the superconducting gap, as expected for d-wave superconductors. Secondly, anomalies have been identified in the field and temperature dependence of several bulk properties below $T_c(B)$ which have been interpreted as phase transitions within the superconducting state not previously found in any (s-wave) superconductors. UPt_3 is a type II superconductor, so to understand the nature of the phase transitions which occur at finite field it is important to characterize the vortex lattice in the different phases.

We have used SANS to study the vortex lattice of UPt_3 as a function of applied field, in the basal plane at $T = 50$ mK. Neutrons are Bragg scattered by the vortex lattice due to the interaction of the dipolar moment of the neutron with the inhomogeneous internal field. The cross-section is proportional to $< \Delta B^2 > \propto (q\lambda)^{-4}$ for $\lambda^{-1} << q << \xi^{-1}$, where q is the momentum-transfer, λ the magnetic penetration depth, and ξ the superconducting coherence length. For UPt_3, as a concequence of the large effective electron mass, λ is two orders of magnitude larger and the cross-section therefore four orders of magnitude smaller than in conventional superconductors where SANS previously has been used to probe the vortex lattice. The key elements which made this first measurement of the vortex lattice in a heavy Fermion system possible were the use of a large and perfect single crystalline sample and choice of the optimal compromise between incident neutron flux and q-resolution. The experiment was performed in the newly commissioned AT&T dilution refrigerator with fields applied along the incident neutron beam.

Figure 1 shows difference between data taken at $H = 3$ kG and $H = 0$ which has been radially averaged in two 45° wedges. The resolution limited peak at $q \approx 0.0090$ Å^{-1} is the result of diffraction from the vortex lattice. Figure 2 shows the azimuthal dependence of the intensity in a ring centered at the peak of Fig. 1. Four of the six peaks are clearly distinguished in Fig. 2 and prove the existense of an epitaxial, distorted hexagonal vortex lattice with a characteristic angle $\alpha = 38 \pm 2°$.

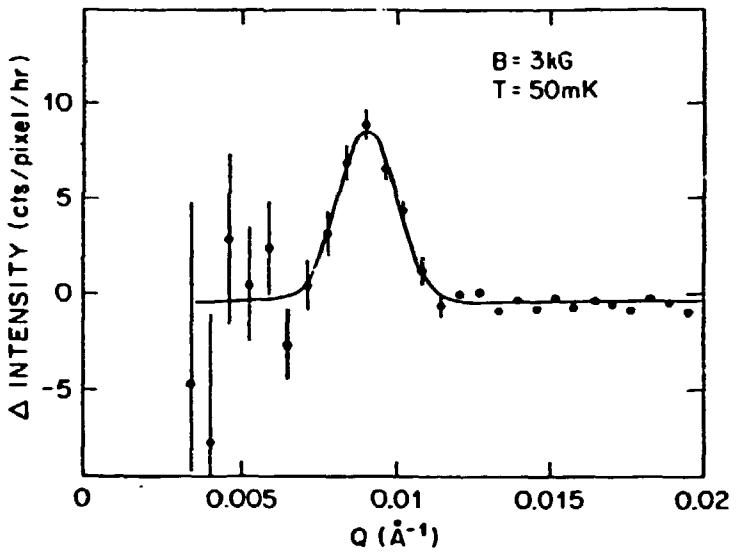

Fig. 1. Radially averaged difference data I(3kG)-I(0).

From the data we deduce the area of the unit-cell $A = (7.7 \pm 0.3) \times 10^{-11}$ cm^2 and the flux which passes through each unit cell, $\Phi = BA = (1.1 \pm 0.05)\ \Phi_0$ where $\Phi_0 = 2.068 \times 10^{-7}$ Gcm^2 is the flux quantum. We conclude that the vortex lattice is singly quantized. Similar data have been obtained for several applied fields 1.25 kG$< B <$ 10 kG. We found no indications of a change in the vortex lattice at the 6 kG phase transition previously reported. More specifically a single crystalline and singly quantized disorted hexagonal vortex-lattice with $\alpha = 42° \pm 10°$ was observed at all fields. This result is not at odds with the existence of a phase transition but indicates that in contrast to theoretical suggestions this transition is not driven by, nor does it give rise to changes in the structure of, or quantization of flux in the vortex lattice.

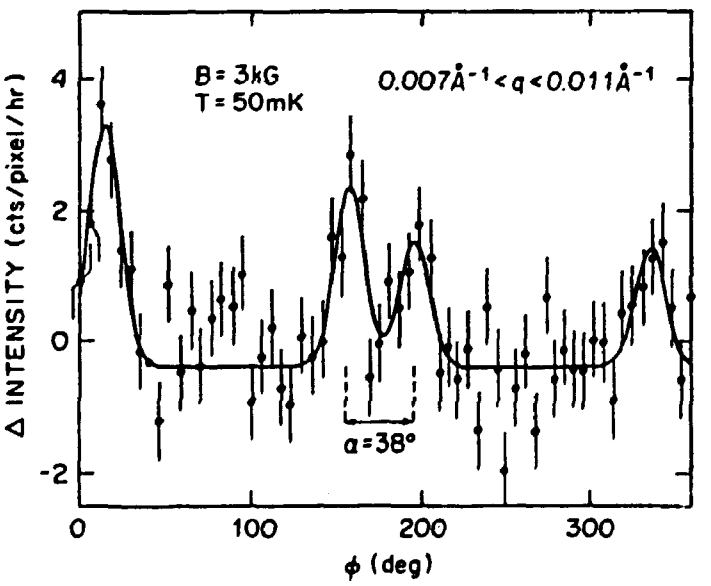

Fig. 2. Azimuthal dependence of difference intensity in a ring (I(3kG)-I(0)).

1.8 Commensurate–Incommensurate Magnetic Phase Transitions in dhcp Neodymium Metal and Nd–Pr Metal Alloys

(B. Lebech, *Physics Department, Riso National Laboratory, Denmark* and J. Wolny, *Institute of Physics and Nuclear Techniques, Academy Mining and Metallurgy Mining, Cracow, Poland*)

The light rare elements Nd and Pr crystallizes in the double hexagonal close packed structure (*dhcp*). They form a complete range of solid solutions with the *dhcp* crystal structure. However, their magnetic ordering properties differ. Pure Pr has a singlet magnetic ground state and orders magnetically at very low temperature (50 mK[1]). In contrast pure Nd and the Nd-rich Nd–Pr alloys orders at relatively high temperatures (20 to 10 K[2,3]) and pass through a sequence of multi-q modulated magnetic structures below T_N[4]. The modulation vectors describing the magnetic structures lie in the basal plane of the *dhcp* structure and may in general be described by components $(q_x,q_y,0)$, where q_x and q_y are components parallel and perpendicular, respectively, to the three equivalent [100] reciprocal lattice vectors $\mathbf{a}^*$.

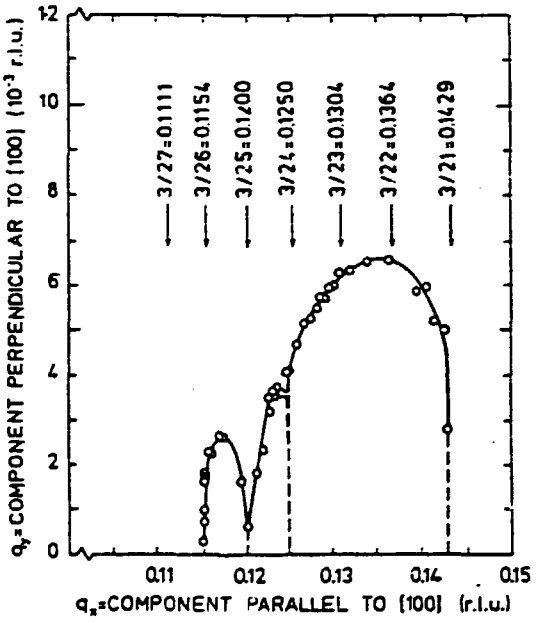

Fig. 1. Components of the modulation vector describing the magnetic structure in pure Nd metal. The q_y component is shown as function of the q_x component in Nd metal. Temperature is an implicit parameter for both axes and T_N corresponds to $(q_x,q_y) = (\frac{1}{7}q_0,0)$. The numbers n above the arrows indicate the commensurate and higher order commensurate values of q_x in terms of the natural length scale $q_0 = 2/\sqrt{3}$ used to describe the magnetic structure[5].

We have examined the temperature dependence of the modulation vectors in Nd and the Nd-rich Nd–Pr alloys in detail. In general, the modulation vectors are incommensurate, *i.e.* both q_x and q_y have finite values. However, when q_x (as a function of temperature) pass through a commensurate value $q_x = q_0/n$, $q_y = 0$, *i.e.* the magnetic structure tends to become commensurate with the modulation vectors parallel to the three equivalent symmetry directions ($\mathbf{a}^*$), where $q_0 = 2/\sqrt{3}$ is a natural length scale for describing

the modulation vector in the *dhcp* structure[5]. This is illustrated in the figure which shows the q_y component of the modulation vector as function of the q_x component in Nd metal. Temperature is an implicit parameter for both axes and T_N corresponds to $(q_x, q_y) = (\frac{1}{2}q_0, 0)$. The numbers n above the arrows indicate the commensurate and higher-order commensurate values of q_x. It seems that the tendency to lock-in at higher order commensurate values of the modulation vector increases with decreasing temperature. Similar behaviors are observed in the Nd-rich Nd–Pr alloys although the number of commensurate–incommensurate transitions are considerably reduced. The data shown in Fig. 1 was obtained during cooling. However, there is pronounced temperature temperature hysteresis in both q_x and q_y, and although it is not evident from the data in Fig. 1, we do have a somewhat less complete data set during heating, which lend support to the postulated commensurability for $(q_x, q_y) = (\frac{1}{8}q_0, 0)$ (see Fig. 1).

We may understand the commensurability by considering the symmetry of the *dhcp* structure. This structure has a four layer stacking sequence ABAC along the c-axis. The atoms in the A-layers have a nearly face centered arrangement of nearest neighbour atoms (cubic sites) whereas the atoms in the B and C layers have a hexagonal close-packed arrangement of nearest neighbours (hexagonal sites). From a symmetry point of view the most important difference between these two sites is the lack of inversion symmetry for the hexagonal sites. Therefore, the directions of highest symmetry in the basal plane are perpendicular to the real space a-axes, *i.e.* the symmetry directions are along the reciprocal cell a*-axes. Thus, it is not surprising that the modulation vectors describing the magnetic structure lie preferably close to these directions. At high temperatures only the hexagonal sites order[2], and close to T_N the magnetic interaction is relatively weak. Therefore we expect the modulation vectors of the magnetic phase to lock-in along the symmetry directions as observed in pure Nd with $q_x = q_0/n$, $n = 7$ and $q_y = 0$. With decreasing temperature q decreases and becomes incommensurate until the next commensurate value is reached ($q_y = 0$). It is worth noticing that the behavior described above is analogous to the one reported for monolayer films on solid surfaces[6] (orientational epitaxy). Whenever the structure of adsorbed material on a homogeneous substrate becomes incommensurate with the lattice of the substrate, the lattice produced by the adsorbed atoms is twisted in relation to the super-lattice of the substrate. In the magnetic case considered, the spins are analogous to the adsorbed atoms. The ground state for these systems is an incommensurate solid with static distortion waves.

[1] K. A. McEwen and W.G. Stirling (1981). J. Phys. C: Solid State Physics **14**, 157.
[2] B. Lebech, (1981). J. Appl. Phys. **52**, 2019.
[3] B. Lebech, K.A. McEwen and P.-A. Lindgård,(1975). J. Phys. C: Solid State Physics **8**, 1684.
[4] E.M. Forgan, E.P. Gibbons, K.A. McEwen and D. Fort, (1989). Phys. Rev. Lett. **62**, 470.
[5] B. Lebech and J. Wolny (1991), *in preparation.*
[6] A.D. Novaco and J.P. McTague, (1977). Phys. Rev. Letters **38**, 1286.

1.9 Neutron Diffraction Studies of the Magnetic Structure of Er – Y Alloys in Applied Magnetic Fields

(S. Kawano, *Kurri Research Reactor Institute, Kyoto University, Osaka, Japan*, B. Lebech, *Physics Department, Risø National Laboratory, Denmark*, and N. Achiwa, *Kyushu University, Fukuoka, Japan*)

At low temperatures ($T \leq T_c = 18$ K), the magnetic structure of Er metal is a c-axis cone structure with a periodicity close to eight atomic c-axis layers ($Q_c \sim 0.24$ Å^{-1}). This structure is suppressed when alloying Er with Y, and instead the low temperature ($T < 34$ K) magnetic structure may be described as a c-axis modulated ellipsoidal cycloidal structure in which the moments are confined to the a–c plane of the hexagonal closed packed crystal structure[1]. Both in the pure Er metal and in the alloys, a strong axial anisotropy exixts, causing a large c-axis spin component. When applying a magnetic field parallel to the easy c-axis in the cone phase, Er becomes ferromagnetic at a rather low critical field H_c[2]. However, in the cycloidal phase, H_c i relatively large ($H_c = 5$ T at 30 K[3]). In the Er–Y alloys it is similarly expected that the field will modify and eventually destroy the cycloidal spin structure and align the spins along the c-axis.

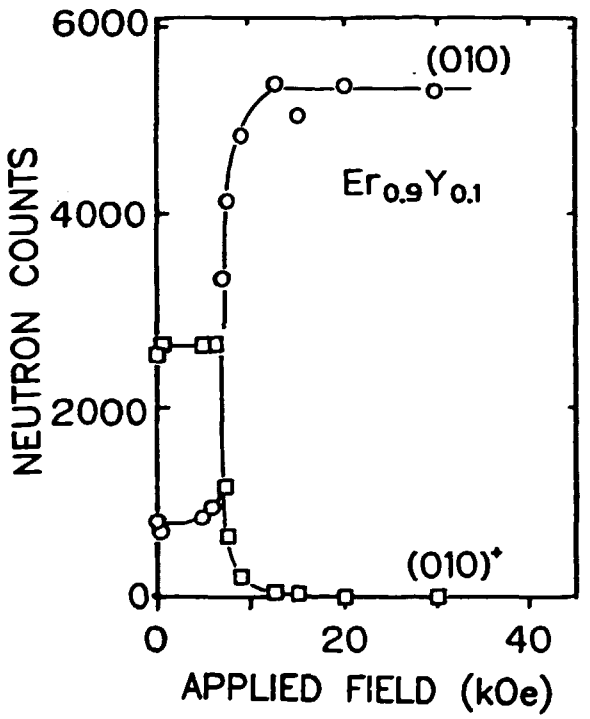

Applied magnetic field dependence of the intensities in the $(01\bar{1}0)$ and the $(01\bar{1}q)$ Bragg peaks (marked by (010) and (010)$^+$ for simplicity) in $Er_{0.9}Y_{0.1}$ at 4.2 K. The $(01\bar{1}0)$ peak is combined nuclear and magnetic Bragg peak which monitors the ferromagnetic spin component along the hexagonal axis and the $(01\bar{1}q)$ peak monitors the modulated spin component in the cycloidal low-field low-temperature phase.

In zero applied field, the magnetic phase diagram (x, T, H) has been extensively studied[4] in the $Er_{0.9}Y_{0.1-x}La_x$ alloy system, but the influence of an applied magnetic field has not been studied experimentally in detail. In order to establish the magnetic phase diagram (x, T, H) of these alloys in sufficient detail to serve as a basis for theoretical studies, a neutron diffraction study of $Er_{1-x}Y_x$ was initiated. The single crystal sample was mounted in a vertical field ($H \leq 4.5$ T) cryo-magnet. The sample was oriented with the c-axis vertical, *i.e.*, parallel to the applied magnetic field. The diffraction measurements were done on a two-axis diffractometer equipped with a detector arm which can be tilted somewhat out of the horizontal plane. Hereby, the instrument allows monitoring of magnetic and nuclear Bragg reflections in the a-b plane of the hexagonal closed packed structure as well as monitoring of the magnetic satellite Bragg peaks (evidence of the cycloidal structure) close to the horizontal a–b plane. As an example, the figure shows the field dependence of the $(01\bar{1}0)$ and the $(01\bar{1}q)$ Bragg reflections in $Er_{0.9}Y_{0.1}$ obtained at 4.2 K. With increasing applied field the $(01\bar{1}q)$ reflection decreases abruptly whereas the $(01\bar{1}0)$ increcreases abruptly at the critical field $H_c = 0.7$ T. As expected, there is a field induced transition from the cycloidal zero field structure to the ferromagnetic c-axis aligned structure at H_c. The modulation vector $Q_c = 0.275$ Å^{-1} describing the cycloidal structure shows no field dependence at 4.2 K.

[1] S. Kawano and N. Achiwa, (1989). Physica B **156 & 157**, 771.
[2] J.J. Rhyne, S. Foner, E.J. McNiff, Jr. and R. Dolco, (1968). J. Appl. Phys. **39**, 892.
[3] J.L. Feron, (1969). Thesis Grenoble 1969.
[4] S. Kawano, (1989). J. Magn. Magn. Mat. **79**, 338.

1.10 Neutron Diffraction Studies of the Magnetic Structure of Er under the Influence of Hydrostatic Pressure

(S. Kawano, *Kurri Research Reactor Institute, Kyoto University, Osaka, Japan*, B. Lebech, *Physics Department, Risø National Laboratory, Denmark*, and N. Achiwa, *Kyushu University, Fukuoka, Japan*)

Er metal crystallizes in the hexagonal closed packed structure. It orders magnetically at $T_N \sim 84$ K into a c-axis modulated sinusoidal structure. Below $T_{cy} \sim 54$ K the moments are confined to an a–c plane and modulated to form an cycloidal arrangement which can be described by a fundamental modulation vector Q_c parallel to the hexagonal axis[1,2]. With decreasing temperature, Q_c increases between T_N and T_{cy}, whereas Q_c decreases from $\sim 0.29\text{Å}^{-1}$ to $\sim 0.24\text{Å}^{-1}$ between T_{cy} and $T_c \sim 18$ K. At T_c, the magnetic structure changes once more, this time to a conical phase with a large c-axis ferromagntic component and an almost temperature independent turn angle of the basal plane moment component. In the cycloidal phase a large number of higher harmonic magnetic satellite peaks are observed at $(h, k, \overline{2h} + \overline{2k}, l) \pm (000\ nq)$, $n = 1, 3, 5$ *etc.* These higher order harmonics are *not* observed in the conical phase.

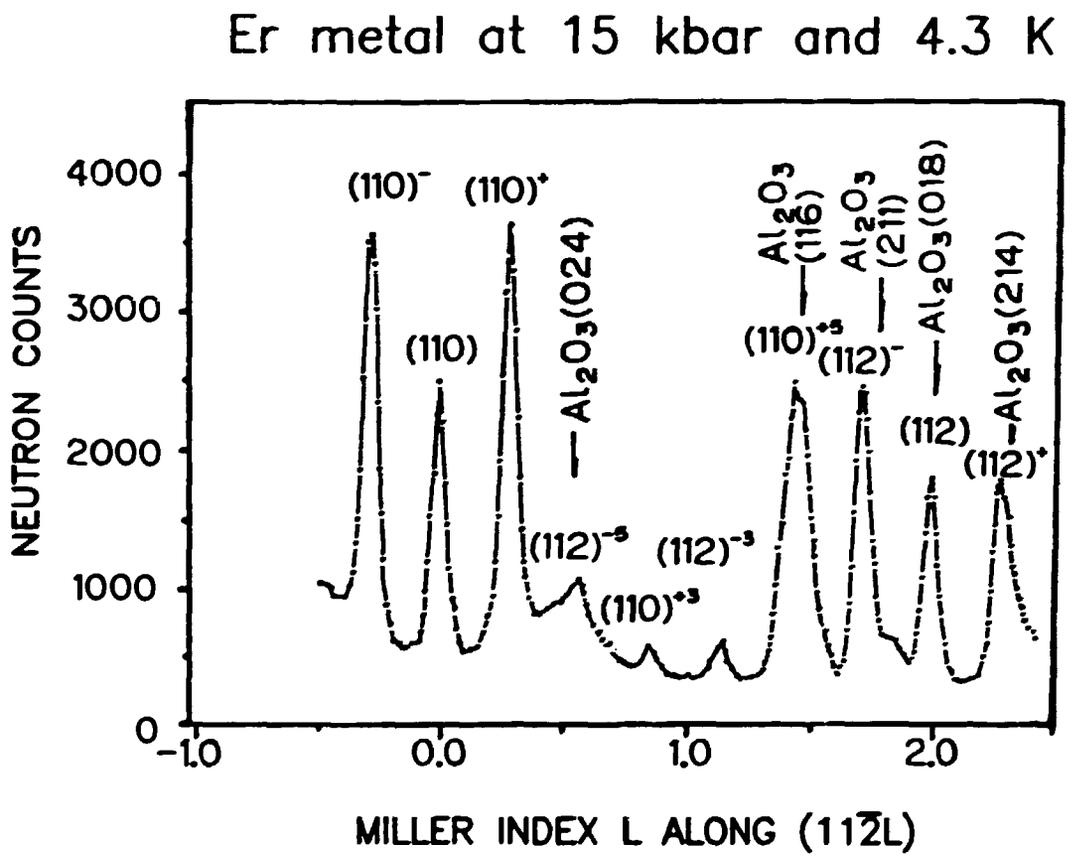

Neutron diffraction scan along the c-axis through the $(11\bar{2}0)$ reciprocal lattice point in an Er single crystal at 4.3 K and $\sim$ 15 kbar hydrostatic pressure. The arrows show the powder peaks from scattering from the hot-pressed, alumina cylinder inner-part of the high pressure cell.

The magnetic (H,T) phase diagram of Er metal has been studied extensively by neutron diffraction and it is of interest to extend these studies to include pressure effects as well. Neutron diffraction studies of the magnetic structure of Er metal using a clamp-type high pressure cell have therefore been initiated. The high-pressure cell was developed by Onodera *et al.*[3] under the auspices of the U.S.-Japan Cooperative Program in Neutron Scattering supported by the U.S. DOE and the Ministry of Education, Science and Culture, Japan. The cell is similar to the one developed by McWhan *et al.*[4] and uses a NaCl single crystal placed close to the single crystal sample as pressure-standard material. The position of the (200) Bragg peak from NaCl can be monitored during the diffraction measurement and used to determine the hydrostatic pressure applied to the sample. The Er single crystal sample was mounted in the pressure cell with the [$\bar{1}$100] axis along the vertical cell axis. In the present investigation, the pressure was clamped at $\sim$ 15 kbar. The cell was then mounted in a variable temperature ^{4}He-cryostat placed on a neutron diffractometer. In order to determine the magnetic structure at 4.2 K and $\sim$ 15 kbar, several neutron diffraction scans (parallel to symmetry axes) were made in the horizontal scattering plane defined by the [11$\bar{2}$0] and [0001] axes.

The figure shows the result of such a scan parallel to the [0001] axis through the (11$\bar{2}$0) reciprocal lattice point. The data show the (11$\bar{2}$0) nuclear Bragg peak and a number of magnetic satellite peaks at (11$\bar{2}$0) $\pm$ (000 nq), n = 1, 3, 5 *etc.*, which are marked by $(110)^{-n}$ or $(110)^{+n}$ for simplicity. In addition several powder peaks from the inner part of the pressure cell are observed. This data set, obtained at 4.3 K and $\sim$ 15 kbar, is tentatively interpreted in terms of a magnetic structure similar to the zero pressure cycloidal structure observed in Er above T_c, although measurements of the temperature dependence of the (0002) $\pm$ (000 nq) and the (11$\bar{2}$0) peak and its satellites are needed in order to establish the magnetic structure at $\sim$ 15 kbar and 4.3 K in full detail.

[1] M. Habenschuss, C. Stassis, S.K. Sinha, H.W. Deckman and F.H. Spedding, (1974). Phys. Rev. B **10**, 1020 and references therein.
[2] J. Jensen, (1976). J. Phys. F **6**, 1145.
[3] A. Onodera, Y. Nakai, N. Kunitomi, O.A. Pringle, H.G. Smith, R.M. Niclow, R.M. Moon, F. Amita, N. Yamamoto, S. Kawano, N. Achiwa and Y. Endoh, (1987). J. Appl. Phys. **26**, 152.
[4] D.B. McWhan, D. Bloch and G. Parisot, (1974). Rev. Sci. Instrum. **45**, 643.

1.11 Magnetic Structures of the Rare Earth Alloy HoEr

(B.K. Howard and J. Bohr, *Physics Department, Risø National Laboratory, Denmark*)

The magnetic structures of a single crystal of a holmium-erbium random alloy have been investigated by means of elastic neutron diffraction measurements in the temperature range 120 K - 10 K, using the triple axis spectrometer TAS1. The system is found to order magnetically at a temperature of 104 K. Several magnetic reflections have been investigated as a function of temperature. The figure below shows the variation of the integrated intensity of the (0,0,2-q) and (1,0,q) satellites with temperature. Three distinct phases can be identified below the ordering temperature, a high temperature phase between 104 K and 47.5 K, an intermediate temperature phase between 47.5 K and 35 K and a low temperature phase. A study of the magnetic wavevector q as a function of temperature has also been performed. In the high temperature phase, q shows a steady decrease as the temperature is lowered. At the onset of the transition to the intermediate temperature phase, q appears to remain constant, at a value of 0.25 c^* between 47.5 K and 44.5 K. A lock-in transition to q=0.25 c^* is observed in pure Er between 24 K and 18 K. At the transition to the low temperature phase, q falls rapidly to a low temperature value of 0.226 c^*. The three phases are interpreted as follows; the high temperature phase is a c-axis modulated basal plane spiral, the intermediate temperature phase is a basal plane spiral and the low temperature phase is a conical spiral.

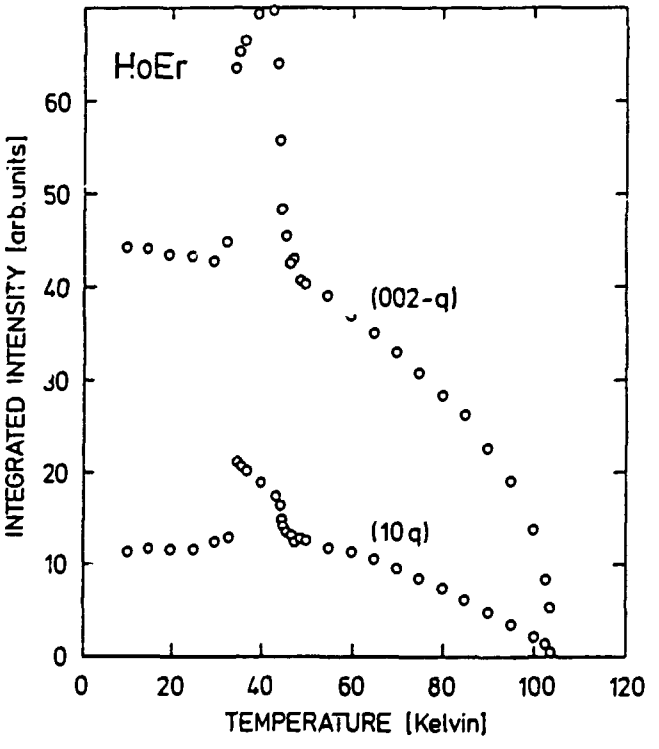

Integrated intensities of the (0,0,2-q) and (1,0,q) magnetic satellites as a function of temperature.

1.12 Magnetic X-ray Scattering Studies of a HoEr Alloy

(J. Bohr, R. Feidenhans'l, B.K. Howard, *Physics Department, Risø National Laboratory, Denmark*, and M. Wulff, *European Synchrotron Radiation Facility, Grenoble, France*)

Anomalous magnetic X-ray scattering studies of a holmium-erbium random alloy has been carried out at the W1 wiggler beam line at HASYLAB. Resonance exchange scattering was observed at both the holmium and the erbium L_{III} absorption edge. The (004^+) magnetic satellite was systematically studied as function of temperature through the temperature ranges corresponding to the three different magnetic structures of the sample; the high temperature structure is c-axis modulated, the intermediate temperature a basal plane spiral, and the low temperature a conical spiral. In all phases, it was found that the holmium and erbium magnetic moments order with the same wave vector. The figure shows the σ to π component resonance enhancement observed at the L_{III} edge of holmium in each of the three magnetic structures. For the two high temperature structures a double resonance enhancement is seen in the vicinity of the edge. This is consistent with what is observed for pure holmium where both dipole and quadrupole electronic transitions are observed. In the low temperature phase additional peaks are observed at about 30 eV below and at about 15 eV above the edge. We note that in this phase the centrosymmetry of the unit cell is broken allowing new transitions channels as well as interference scattering. The origin of these peaks is currently under investigation.

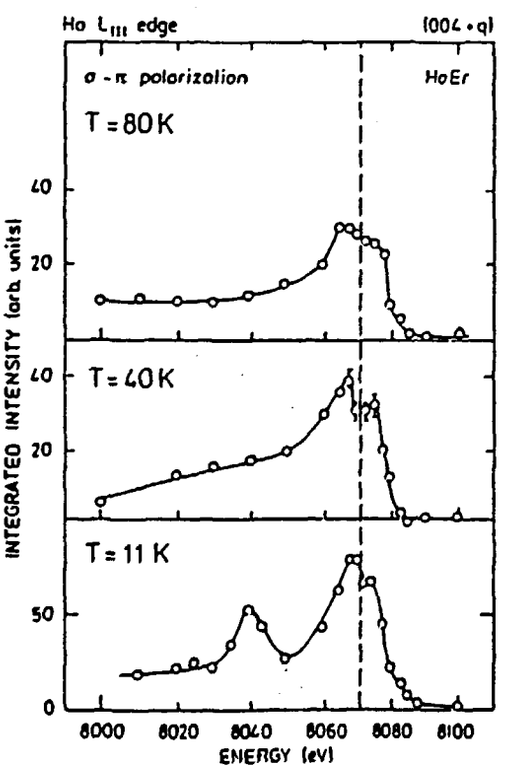

Anomalous magnetic scattering from a HoEr alloy.

1.13 Investigations of Systems Containing Very Short Hydrogen Bonds

(N. Kalsbeek, S. Larsen, *Chemistry Department, University of Copenhagen, Denmark*, B. Lebech, *Physics Department, Risø National Laboratory, Denmark*, and R. G. Hazell, *Department of Inorganic Chemistry, University of Aarhus, Denmark*)

In chemical compounds, very short hydrogen bonds (2.4–2.5 Å) can either be symmetric with the hydrogen atom positioned exactly between the two oxygen atoms or asymmetric with the hydrogen atom placed closer to one of the two oxygen atoms. Many symmetric hydrogen bonds are crystallographically symmetric, *i.e.*, the two oxygen atoms are related by crystallographic symmetry. In this case three situations can occur:

- The hydrogen atom is placed on the crystallographic symmetry element.
- The hydrogen atom is statistically disordered, *i.e.*, in half of the unit cells it is close to one oxygen atom and in the other half close to the other oxygen atom.
- The hydrogen atom is dynamically disordered, *i.e.*, moving between two positions on each side of the symmetry element.

The first situation would indicate a single minimum potential function for the hydrogen atom whereas the second and third would indicate a double minimum potential function.

The investigations of systems containing very short O–H–O hydrogen bonds have been continued. Of special interest is the position of the hydrogen atom in the short hydrogen bond. The studied compounds are acid salts of malonic acid ($H_2C_3H_2O_4$) and succinic acid ($H_2C_4H_4O_4$). The cations are Na^+ and K^+ for malonic acid and Na^+, K^+, Cs^+, $CH_3NH_3^+$, $(CH_3)_2NH_2^+$, $C_2H_5NH_3^+$ and $(C_2H_5)_2NH_2^+$ for succinic acid. To make the crystals more suitable for neutron diffraction studies some of the crystals were partially deuterated, *e.g.*, the malonic acid K^+ and the succinic acid Na^+ salts. Normally, very short symmetric hydrogen bonds link the anions into infinite chains in all the salts. However, for two of the salts asymmetric hydrogen bonds are found. These short asymmetric bonds also link the anions into infinite chains. The length of the symmetric bonds are in the range 2.4295(5)–2.4612(4) Å. The length of the single asymmetric bond found in NaH–malonate is 2.5547(9) Å. In $C_2H_5NH_3H$–succinate two asymmetric hydrogen bonds of lengths 2.456(4) and 2.483(4) Å, respectively, are found.

Low temperature X-ray investigations show that the symmetric hydrogen bonds are best described by two half populated hydrogen atom positions placed on either side of the crystallographic symmetry element. However, because of the weak scattering power of hydrogen, X-ray diffraction experiments cannot distinguish between statistical and dynamical hydrogen disorder. Therefore, four-circle neutron diffraction data have been collected at room temperature for Na(H,D)–succinate and CsH–succinate H_2O. The crystal structure refinements of the X-ray data differ from the refinements of the neutron diffraction data. In the latter case, the short hydrogen bond is best described by placing the hydrogen atom on the symmetry element (for both salts an inversion center). The greatest thermal motion of the hydrogen atom is not in the direction of the short hydrogen bond, but perpendicular to it. However, the X-ray data are of better quality than the

neutron data. From the X-ray data for the structures containing symmetric hydrogen bonds, the R-factor describing the agreement between the observed and calculated structure factors ($R(|F|)$) are in the range 2.1 % to 4.0 %, and the ratio between number of observed reflections used in the refinements and the number of refined variables in the range 21 to 69. The corresponding values from a preliminary analysis of the two neutron data sets are 6 % and 7.

The contradiction between results from X-ray and neutron diffraction studies was also observed by Thomas and Liminga[1] for the compound $N_2H_5HC_2O_4$. They point out that the difference may be an artifact because the centre of the electron distribution associated with the H atom in an X–H bond is 0.1–0.2 Å closer to atom X than the centre of the corresponding proton distribution. A separation of 0.4 Å is resolvable in an X-ray diffraction experiment and will give rise to a double peak in the short hydrogen bond, whereas one peak at the centre of the bond is found in their neutron diffraction experiment.

[1] J.O. Thomas and R. Liminga, (1978). Acta Cryst. B **34**, 3686.

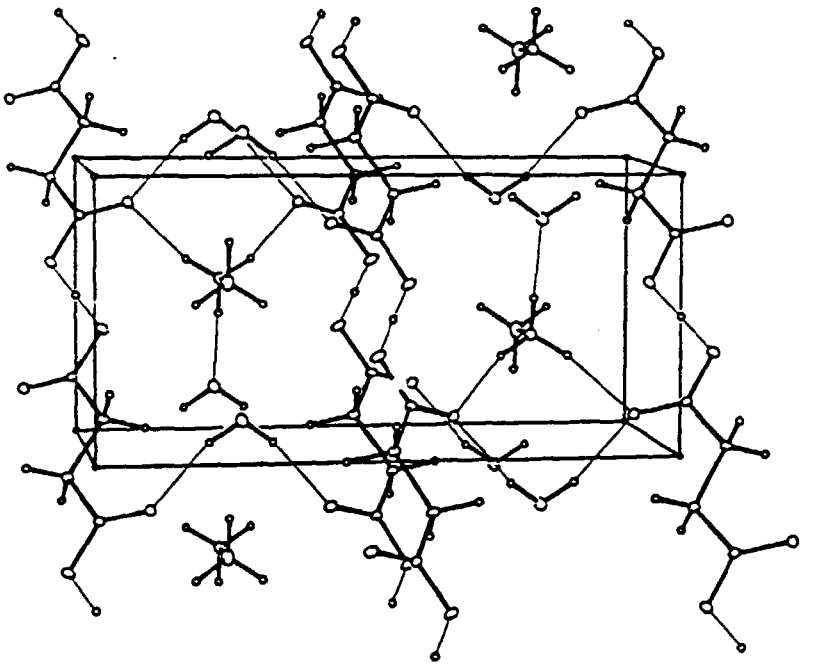

The unit cell of methylammonium hydrogen succinate monohydrate illustrating the infinite chains of anions.

1.14 NiAs Type Related Phases in the Ni–Ga–As System

(J. Fjellstad Schjerven, H. Fjellvåg, *Department of Chemistry, University of Oslo, Blindern, Norway*, and B. Lebech, *Physics Department, Risø National Laboratory, Denmark*)

Integration of III–V semiconductor circuits involves metallization of *e.g.* GaAs by *d*-metals (M). Therefore, the chemistry and structural properties of M/III–V interface have become of interest. Frequently, ternary phases are formed as reaction products. Information about the phase diagrams are far from complete for such systems, and hence the phase diagram model calculations performed so far suffer from the lack of proper experimental data to compare to. The present study concerns NiAs type related phases in the Ni–Ga–As ternary system.

Recent studies of thin films of Ni on GaAs show the presence of various ternary phases, most of which have crystal structures which are related to NiAs-type superstructures. Some of these phases cannot be obtained by standard preparation procedures (*e.g.* closed silica tube technique) and their stability and annealing features are rather confusing. At high temperatures there exist wide ranges of solid solubility which are strongly temperature dependent. The distribution of Ni, Ga and As in these phases are best studied by neutron diffraction because the similarity in the number of electrons for the actual atoms makes a structural determination from X-ray diffraction data difficult.

Bulk samples (produced by reacting of the pure elements) of the high and low temperature solid solution phases were studied by neutron powder diffraction. These studies were supplemented by powder X-ray diffraction measurements (using a Guinier Simon camera) of the thermal expansion and of temperature induced order - disorder transitions in the ternary phases. Information on the electronic properties of the different phases was obtained from magnetic susceptibility measurements between 4 and 350 K.

For samples belonging to the quenced high-temperature phase, $Ni_{1+t}As_{1-x}Ga_x$ ($0.16 \leq t \leq 0.77$), the neutron powder diffraction data proved that all the additional Ni atoms occupy trigonal bi-pyramidal holes whereas the Ga for As substitutions occur solely on the non-metal sublattice and do not introduce any long range order. For the low temperature phases, on the other hand, long range ordering of Ga, As and Ni occurs. In order to study this in detail, we have collected powder neutron data for $Ni_{13}Ga_{9-x}As_x$ ($0 \leq x \leq 3$), but the data analyses are not yet finished.

1.15 Structural Investigation of $NaCr_3O_8$ and $LaMnO_3$ Using Neutron Powder Diffraction

(P. Norby, S. Habekost, *Chemistry Department, University of Odense, Denmark*, and B. Lebech, *Physics Department, Risø National Laboratory, Denmark*)

Chromium oxides with composition MCr_3O_8 (M = Li, Na, K) are of interest as potential cathode materials in lithium batteries. The compounds contain chromium in oxidation states III and VI in a ratio of 1:2, *i.e.* $Na(CrIII)(CrVI)_2O_8$. The present study of $NaCr_3O_8$ was done in continuation of earlier studies of structural, magnetic and electrochemical properties of these materials. Magnetic measurements indicate antiferromagnetic ordering at low temperature in KCr_3O_8, whereas the susceptibility data of $NaCr_3O_8$ was not easily interpreted. In an attempt to clarify the magnetic behavior of $NaCr_3O_8$ low-temperature neutron powder diffraction data were collected and analysed. The MCr_3O_8 compounds (M = Na, K, Cs, Tl) have layered structures.The layers consist of octahedrally coordinated Cr(III) linked together by single chromate groups (Cr(VI)). The layers are held together by the cations, which control the interlayer distance and the symmetry of the structure. Although the potassium ions have ten-fold oxygen coordination, the sodium ions in $NaCr_3O_8$ have distorted octahedral coordination. Powder diffraction data were obtained for different temperatures between 12 and 325 K using incident neutrons of wavelength of 2.39 Å. However, no clear evidence of additional peaks associated with magnetic ordering was observed at low temperatures. Rietveld refinements, based on nuclear scattering only, have been performed for all the data, but the evaluation of the results are not yet completed.

$LaMnO_3$ doped with *e.g.* Sr is interesting in connection with research concerning materials for high temperature solid oxide fuel cells. The present investigation is the first in a series which will include doped and undoped lanthanum manganites. Two undoped samples, prepared by different methods, were selected for the neutron diffraction experiments. The stoichiometry of the compounds, especially the oxygen content in $LaMnO_3$, is of outmost importance for the ionic and electronic conductivity. The present study aims to determine the population of the oxygen atoms and the distribution of lanthanum and manganese in the structure by Rietveld refinement. $LaMnO_3$ has a distorted perovskite type structure at room temperature. The distortions from cubic symmetry may be of hexagonal (rhombohedral), orthorhombic or monoclinic nature. In order to have full advantage of the information from the neutron diffraction data, the samples were measured using incident neutrons of wavelength 2.39 and 1.11 Å. The larger wavelength makes a possible splitting of the Bragg peaks more visible, and may thus be advantageous in determining the correct symmetry of the unit cell. However, a reliable refinement of population parameters and temperature factors demands that data are also collected for reflections with small *d*-values, which may be obtained using the shorter wavelength. Preliminary structure refinements by profile analyses have shown that crystal structure of the investigated samples can be described in the rhombohedral spacegroup $R\bar{3}c$.

1.16 Superconducting Cuprates and Related Compounds

(A. Nørlund Christensen, *Department of Inorganic Chemistry, University of Aarhus, Denmark*, B. Lebech and N.H. Andersen, *Physics Department, Risø National Laboratory, Denmark*)

A selection of rare earth cuprates has been synthesized by solid state reactions[1] and models of their crystal structures have been tested by profile refinements of powder neutron diffraction data[2]. The parent compounds are La_2CuO_4 or $YBa_2Cu_3O_{7-x}$ and the substituted compounds are formed by substituting La and Y by Nd and Ba by Ca or Sr.

Furthermore, the solid state synthesis of $YBa_2Cu_3O_{7-x}$ from reaction mixtures of **(1)** $BaCO_3$ - CuO - Y_2BaCuO_5 and **(2)** $BaCuO_2$ - CuO - Y_2BaCuO_5 have been investigated by time resolved *in situ* neutron powder diffraction in the temperature range from 810 – 850 °C. The samples were pellets of these mixtures. A well defined sample volume was kept at the reaction temperature during the collection of several diffraction patterns. For each mixture the time needed for collecting one pattern was an order of magnitude faster than the time needed for the chemical reaction to reach a state of equilibrium. This means that at any time, the intensity ratios of selected Bragg reflections from each of the phases present, are a direct measure of the volume of a particular phase in the reaction mixture.

The formation of $BaCuO_2$ for the reaction **(1)** turned out to be faster than the formation of $YBa_2Cu_3O_{7-x}$ at temperatures up to 850 °C. At 850 °C, the formation of $YBa_2Cu_3O_{7-x}$ for both reaction mixtures was found to be slow (less than 5 % of $YBa_2Cu_3O_{7-x}$ was formed in twelve hours). Preliminary X-ray powder diffraction investigations of the reaction mixtures **(1)** and **(2)** showed that at 930 °C, 100 % and 80 % of $YBa_2Cu_3O_{7-x}$ is formed within three and one hour, respectively. At 870 °C we found that 80 % of $YBa_2Cu_3O_{7-x}$ is formed within nine hours for reaction **(2)**, and that the main reaction product from reaction **(1)**, $BaCuO_2$, is formed within nine hours. Thus, the time resolved neutron powder diffraction measurements confirm the preliminary X-ray diffraction results that the yield of $YBa_2Cu_3O_{7-x}$ is decreasing drastically with decreasing reaction temperature.

[1] A. N. Christensen, (1990). Acta Chem. Scand. **44**, 769.
[2] A. N. Christensen and B. Lebech, (1990). Acta Chem. Scand. **44**, 902.

1.17 Incommensurate Inelastic Neutron Scattering from $La_{1.9}Sr_{0.1}CuO_4$

(T. Mason, G. Aeppli, S. Cheong, *AT&T Bell Laboratories, Murray Hill, USA*, Z. Fisk, *Los Alamos National Laboratory, USA*, S. Haydn, *ILL, Grenoble, France*, and K.N. Clausen, *Physics Department, Risø National Laboratory, Denmark*)

The understanding of incommensurate 2D inelastic scattering first observed in the high T_c superconductor $La_{1.85}Sr_{0.15}CuO_4$ [1] has been limited by the lack of experimental data on the momentum dependence in the $(h0l)$ plane containing the CuO_2 sheets. We have carried out measurements in this plane on TAS6 for a sample of $La_{1.9}Sr_{0.1}CuO_4$. Figure 1 shows a map of the intensity observed at 1 meV energy transfer at 12 K. Similar results were observed for E = 5 meV. The intensity is clearly peaked away from the commensurate (100) position where antiferromagnetic ordering occur for pure La_2CuO_4.

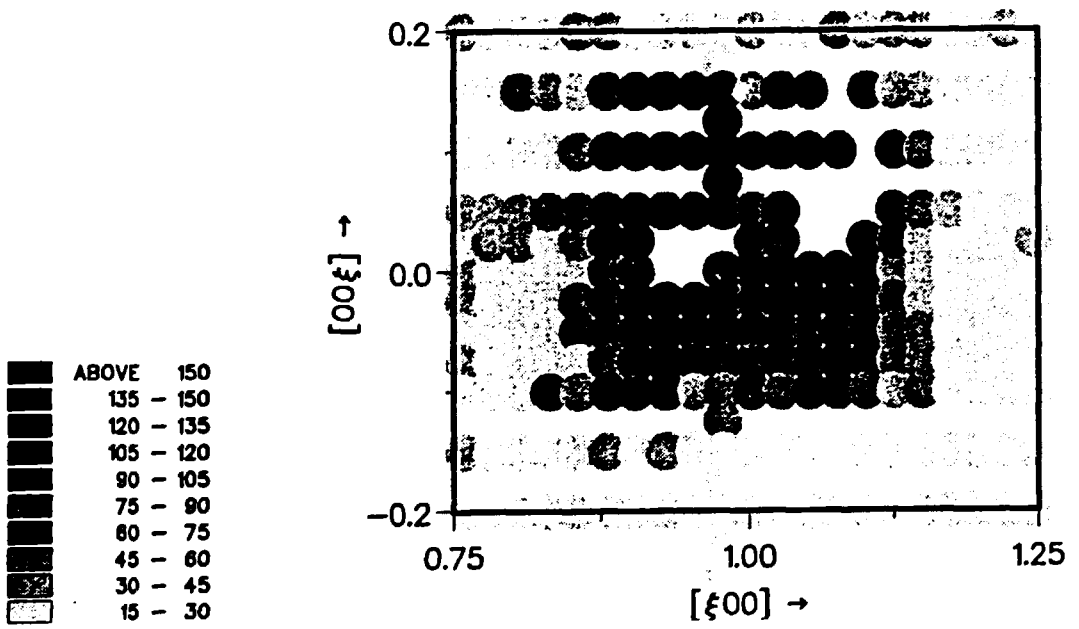

Fig. 1. Observed grid of intensity for 1 meV energy transfer, corrected for background. The counting time is approximately 30 minutes per dot. Dots are missing where spurious peaks were observed, or where no data were taken

A resolution corrected fit to a $(2Q_0 \times 2Q_0)$ box with Gaussian profile centered on (100) (Fig. 2a) or four Gaussians at (100) $\pm$ $(Q_0, 0, \pm Q_0)$. (Fig. 2b) describe the data equally well. What is remarkable is that in both cases the correlation length extracted from the fit is considerably larger than the mean spacing between holes (29 Å for a) and 21 Å for b) *vs.* 12 Å for 0.1 hole per unit cell). This suggests that the incommensurate nature of the scattering is not simply an effect due to frustration of localized Cu^{2+} moments in the presence of mobile holes. One possible explanation is that the scattering arises due to a Fermi surface instability analogous to what occurs in Cr. In this case Q_o would correspond to k_F (= 0.084 r.l.u. for a)) yielding a carrier density of n = 2

$k_F^2/\pi^2 \approx 0.002/\text{Å}^2$ *vs.* $0.1/(5.4\text{Å})^2 \approx 0.003/\text{Å}^2$ from the stoichiometry. Further experiments are required to determine the temperature dependence of the correlation length and whether or not this instability leads to incommensurate ordering at low temperatures.

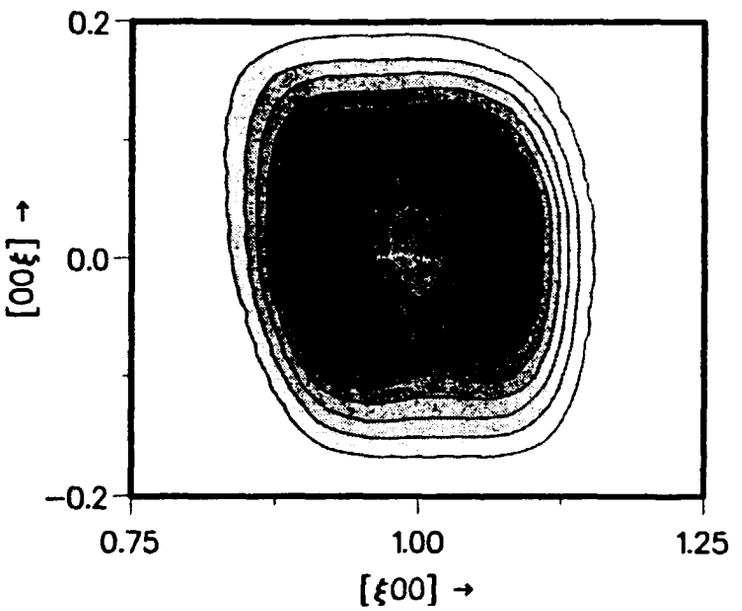

Fig. 2a. Best fit to a box centered on (100).

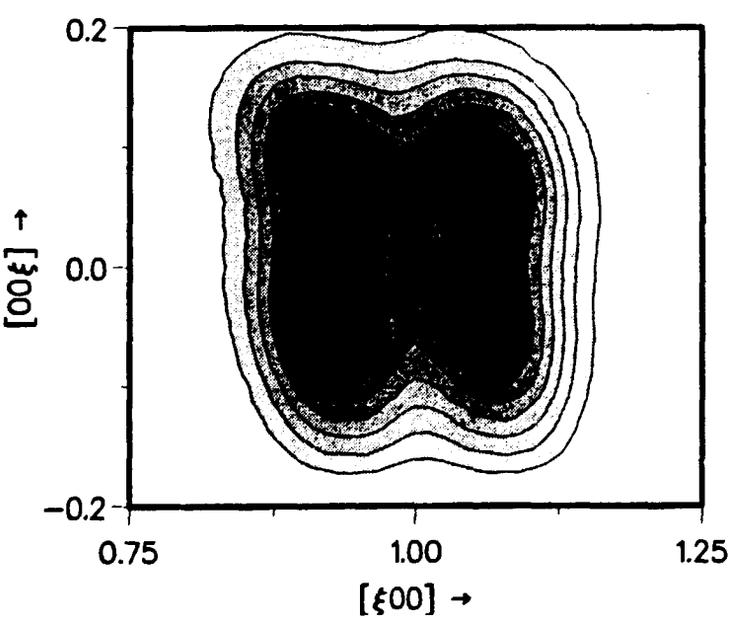

Fig. 2b. Best fit to four posts at $(100)\pm(Q_o, O \pm Q_o)$

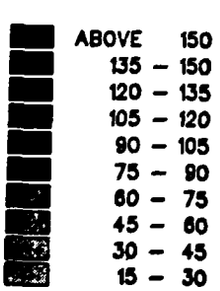

[1] G. Shirane *et al.*, (1989). Phys. Rev. lett. **63**, 330.

1.18 The Crystal Structure of $Pb_2Sr_2HoCu_3O_8$ Studied by Neutron Powder Diffraction

(J.-E. Jørgensen. *Department of Chemistry. Aarhus. University, Denmark* , and N.H. Andersen, *Physics Department, Risø National Laboratory. Denmark)*

High T_c superconductivity with critical temperatures up to 70 K has been observed in $Pb_2Sr_2LnCu_3O_8$ (PSLCO) by partial substitution of the lanthanide (Ln) by Ca or Sr. Early X-ray diffraction studies have shown that PSLCO has an orthorhombic unit cell (space group Cmmm) and a layered structure with a stacking sequence $SrO - CuO_2 - La - CuO_2 - SrO - PbO - Cu - PbO-$ (see the figure), giving a local structure around the double layers of superconducting CuO_2 planes, which is similar to the $-BaO - CuO_2 - Y - CuO_2 - BaO-$ stacking sequence in $YBa_2Cu_3O_{6+x}$ (YBCO). However, the CuO chain structure, which act as necessary charge reservoirs in YBCO, is replaced by PbO-Cu-PbO layers in PSLCO. PSLCO may be oxidized, but the additional oxygen atoms, are considered to enter and oxidize the PbO-Cu-PbO layers rather than creating holes in the CuO_2 planes. Orthorhombic symmetry is apparently necessary for high T_c superconductivity. The X-ray diffraction studies revealed orthorhombic symmetry but the symmetry breaking structural component could not be satisfactorily identified. The goal of the present neutron powder diffration study of $PbSr_2HoCu_3O_8$ was to determine the oxygen positions with higher accuracy and explain the origin of the orthorhombic distortion.

Neutron powder diffraction measurements were performed at room temperature. Structural analyses of the data were carried out by Rietveld refinements of several models. The main problem to solve was to establish the oxygen O(2) positions in the structure (see the figure). Initial refinements were performed in the orthorhombic space group Cmmm, but the results showed that the O(2) oxygens are displaced from the 4*k* *(00z)* position. The final refinements were therefore done in space group $P\bar{1}$ (a=5.378, b=5.421, and c=15.688 Å) with all atoms except the oxygen atoms in the PbO layer constrained to obey C-centering. Satisfactory result were obtained with two oxygen atoms O(2) and O(2') at the 2*i* *(xyz)* sites of $P\bar{1}$. The origin of the observed orthorhombic symmetry was in this way found to be the distortion of the oxygen atoms in the PbO layer. (More details of the study will appear in Acta Chemica Scandinavica **45**,1991).

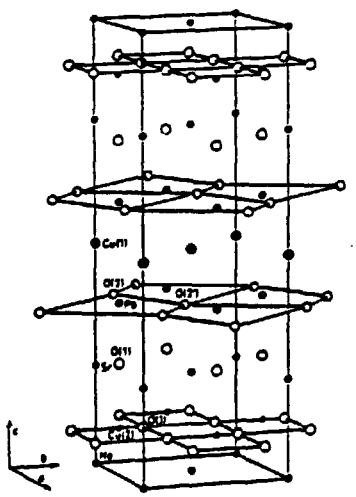

Unit cell of $Pb_2Sr_2HoCu_3O_8$. Cations are marked with filled circles, oxygen atoms with open circles. The oxygen-oxygen connections are marked in the CuO_2 and PbO layers containing the O(3), O(2) and O(2') atoms. All atoms except the O(2) and O(2') oxygen atoms in the PbO layer obey C-centering.

1.19 A Study of Structural Properties, Thermopowder and Superconductivity of $Nd_{1.85}Ce_{0.15}CuO_{4+\delta}$

(N.H. Andersen, B. Lebech, *Physics Department, Risø National Laboratory, Denmark*, C.S. Jacobsen, *Physics Laboratory III, The Technical University of Denmark, Denmark*, I. Mangelschots, *IBM Research Laboratory, Zürich, Switzerland* and A. Wisniewski, *Polish Academy of Sciences, Warszawa, Poland*)

The discovery of superconductivity in $Nd_{2-x}Ce_xCuO_{4+\delta}$ (NCCO) (T_c = 23 K for x=0.15) has attracted considerable interest. The material is derived from the archetype high T_c superconductor $La_{2-x}Ba_xCuO_4$ (LBCO) by standard substitution on the La site. However, instead of Ba^{2+}, Ce^{4+} ions are introduced in the lattice, which should result in an increased electron carrier density in the superconducting CuO_2 planes. Valence considerations assuming $\delta \leq 0$, and Hall measurements suggest that NCCO is an electron conductor, and *not* as the other high T_c materials a hole conductor. Further support for this suggestion is the observation that oxidation of the material destroys superconductivity. Neutron powder diffraction studies have revealed that NCCO (x = 0.15) has essentially full occupation on the oxygen sites O(1) and O(2) for both superconducting and non-superconducting samples[1], whereas $La_{2-x}Ba_xCuO_4$ has essentially full occupation on the sites O(1) and O(3) (see Fig. 1).

We have carried out a powder neutron diffraction study of NCCO (x = 0.15) with respect to possible occupation on the LBCO site O(3), and the structural stability as a result of oxidation and reduction. We ve combined our structural measurements with a gas volumetric technique which allows for *in-situ* oxidation and reduction of the sample and accurate determination of the oxygen concentration changes. Minor structural changes may in this way be recorded from the difference between powder diffraction patterns obtained before and after well-defined sample treatments. The superconducting properties were studied by susceptibility measurements on samples prepared in a similar way as on the neutron powder diffractometer. The nature of the charge carriers were studied for two of the sample preparations by thermopower measurements.

The sample was single phase and it was initially prepared to be superconducting with T_c = 23 K after reduction in N_2 at 890 °C for 15 hours. Analyses of the structural data obtained from this sample resulted in the structure shown in Fig. 1 with occupancies on the oxygen sites: O(1)=1.000 (fixed), O(2)=1.00(3), and O(3)=0.03(1). This gives an oxygen content δ = 0.06(8), which is close to the critical value (δ_c = 0.075) where transition from electron ($\delta < \delta_c$) to hole ($\delta > \delta_c$) conduction is expected. Oxidation of the sample at temperatures up to 800 °C did not change T_c, but gave a minor broadening of the susceptibility transition width. Oxidation at 890 °C resulted in a time evolving degredation of the superconducting properties as observed in the susceptibilty data shown in Fig. 2 (to the left). After oxidation for 60 hours superconductivity is considered to be destroyed. Reduction in N_2 at 890 °C for 15 hours recovers superconductivity. The reduction or oxidation treatments did not cause structural changes that could be observed within the statistical error of our diffraction measurements. From the gas volumetric data we determine that the absorption of oxygen after 60 hour of oxidation at 890 °C is $\Delta\delta$ = 0.02(2). Thermopower measurements carried out on the superconducting sample and after oxidation for 60 hours at 890 °C is shown in Fig. 2 (to the right). The result

is surprising because the superconducting sample has positive thermopower (hole dominated), and the non-superconducting negative thermopower at low temperatures (electron dominated). However, the electronic structure is quite complicated and a traditional single band account is definitely inappropriate. The thermopower is very small, probably indicating that the electronic system is very close to cross-over from electron to hole conduction.

[1]F. Izumi, *et al.* (1989). Physica C **158**, 433 (1989)

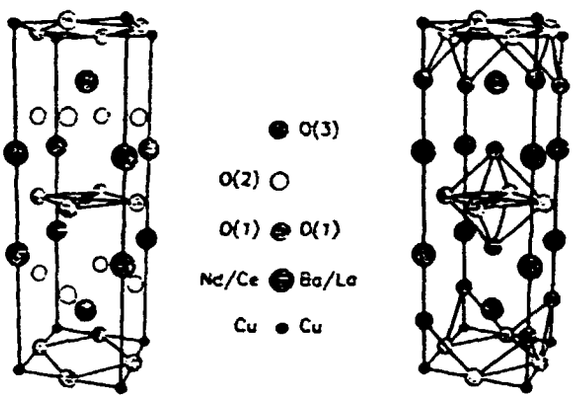

Fig. 1. Crystal structures of $Nd_{2-x}Ce_xCuO_4$ (left) and $La_{2-x}Ba_xCuO_4$ (right).

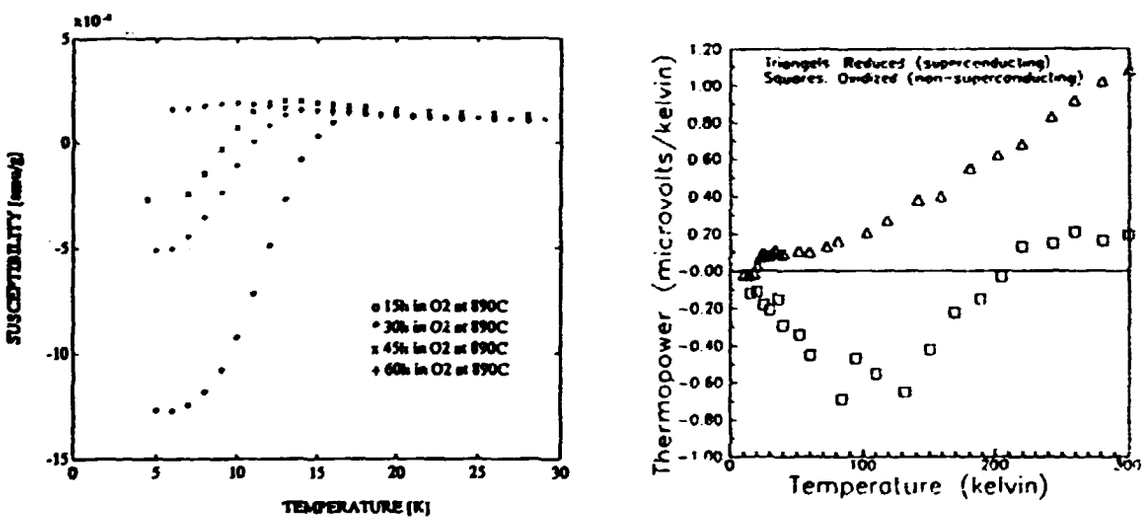

Fig. 2. Susceptibility (left) and thermopower (right) of $Nd_{1.85}Ce_{0.15}CuO_{4+\delta}$. The susceptibility data show the effect of oxidation at 890 °C for different reaction times. The thermopower data have been obtained on the superconducting sample Δ and after oxidation for 60 hours at 890 °C (□, non-superconducting).

1.20 Structural and Thermodynamic Properties of Oxygen Ordering in $YBa_2Cu_3O_{6+x}$

(N.H. Andersen, B. Lebech and H.F. Poulsen, *Physics Department, Risø National Laboratory, Denmark*)

The superconducting properties of $YBa_2Cu_3O_{6+x}$ (YBCO) are strongly dependent on the oxygen stoichiometry as manifested most significantly in the superconducting transition temperatures T_c versus x ($0 < x < 1$). Superconductivity with $T_c = 60$ K is observed for $0.4 < x < 0.8$ above which concentration range T_c raises to 90 K. This observation is interpreted to result from a charge transfer mechanism where the variable amount of oxygen in the basal plane structure creates the necessary number of holes in the superconducting CuO_2 planes for $x > 0.4$. However, details in the T_c versus x curve vary significantly on sample preparation methods, and recent results have clearly shown that the superconducting properties are directly correlated with the structural ordering of the basal plane oxygen atoms. It is therefore of significant interest to understand the oxygen defect ordering properties of YBCO.

In the present work the structural and thermodynamic properties of basal plane oxygen ordering have been studied. An experimental technique, based on neutron powder diffraction in combination with gas volumetry, has been developed and used for *in situ* preparation of YBCO samples with well-defined oxygen stoichiometry under equilibrium conditions. Simultaneous by studies of structural properties, oxygen equilibrium pressure and bulk oxygen in-diffusion kinetics in an extended part of (x,T)–space ($0.15 < x < 0.92$, $25°C < T < 725°C$) are performed.

From the structural data we have established the phase transition line separating tetragonal disordered T-phase from orthorhombic ordered O-phases (see left hand figure). Our results are in close agreement with the recent theoretical predictions by Ceder *et al.* [1] (bold curve in the left hand figure) from 2D anisotropic next-nearest-neighbour Ising model calculations (the so-called ASYNNNI model) using *ab initio* interaction parameters determined by Sterne and Wille[2]. The OI-phase corresponds to the fundamental ordered orthorhombic structure, the $\overline{\text{OI}}$-phase is a predicted orthorhombic oxygen vacancy ordered phase, and the OII-phase is the oxygen double-cell ordered structure. The dashed curves indicate the theoretical prediction of the phase lines separating the T- and $\overline{\text{OI}}$-phases and OII- and OI-phases, but the presence of the $\overline{\text{OI}}$- and the OII-phases could not be identified from the powder diffraction data, for the OII-phase probably because the ordering is two-dimensional and have a finite in-plane correlation length. Broadening of the neutron powder diffraction peaks were identified to result from twin-domain formation in two different orthorhombic phases. However, the phase line separating the two orthorhombic phases were found to be at $x = 0.51$, and not as predicted theoretically by the dashed curve in the left hand figure. The oxygen equilibrium pressure shown as isotherms in the right hand figure has significant features. Firstly, the close lying isotherms at oxygen stoichiometries $x \simeq 0.9$ and to some extend at $x \simeq 0.2$ indicate that for pressures 1 Torr $< P <$ 760 Torr the stability range of YBCO is $0.15 < x < 0.92$. Secondly, the pressure jump in the low temperature isotherms around $x = 0.5$ proves the thermodynamic stability of the OII-phase and may be used to determine one of the interaction parameters in the ASYNNNI model. Finally, the maxima or kinks in the

isothermal pressures around $x = 0.25$ are in close agreement with the recent ASYNNNI model prediction of the disorder line (dashed line in the right hand figure[3]) indicating formation of chain-like oxygen structures in the tetragonal phase.

The relaxation time τ of bulk oxygen in-diffusion has been determined from the pressure decay rate in the gas volumetric setup. Despite a rather broad particle size distribution of the ceramic sample (between 2 and 100 μm) a simple exponential decay was observed throughout. This suggest that micro-cracks and twin-domain boundaries rather than ceramic grain size determine the effective diffusion pathway. At high temperatures τ is activated with different activation energies in the tetragonal phase (0.55 eV) and the orthorhombic phase (0.25 eV). At lower temperatures τ approaches a constant level with an x-dependence which indicates that oxygen chain formation limits the diffusivity.

All our data give strong support to the validity of the ASYNNNI model description of the oxygen basal plane ordering structure, but they indicate that the *ab initio* interaction parameters[2] should be slightly modified.

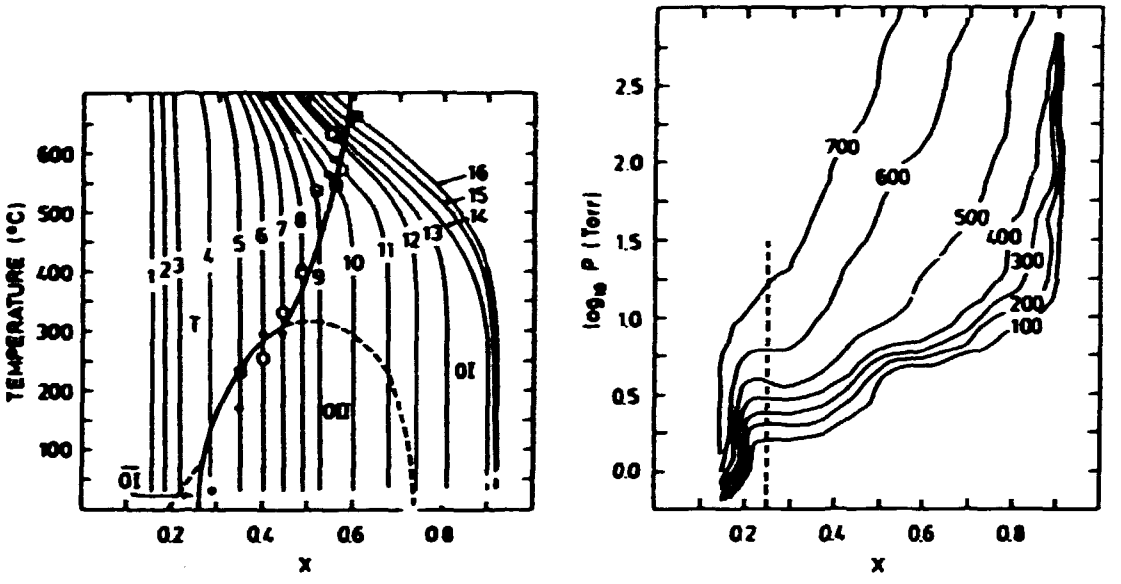

Structural phase diagram (left) and oxygen equilibrium pressure (right) of $YBa_2Cu_3O_{6+x}$.
Left: Thin curves are trajectories along which experimental data are collected. • *is experimental data indicating the transition temperature from the tetragonal (T) to orthorhombic (O) structures.* □ *marks the temperature above which there is no neutron powder diffraction peak broadening from twin-domains. The solid curves and the structural O-phases are explained in the text.*
Right: Full curves are isotherms (temperatures in °C), the dashed line is the disorder line predicted from ASYNNNI model calculations (see text).

[1]G. Ceder, M. Asta, W.C. Carter, M. Kraitchman, D. deFontaine, M.E. Mann and M. Sluiter, (1990). Phys. Rev. B **41**, 8698.
[2]P. Sterne and L.T. Wille, (1990). Physica C **162-164**, 223.
[3]P.A. Rikvold, M.A. Novotny and T. Aukrust, *to be published.*

1.21 A Model of the Static and Dynamic Relationships between Oxygen Ordering and Superconductivity in $YBa_2Cu_3O_{6+x}$

(H.F. Poulsen, N.H. Andersen *Physics Department, Riso National Laboratory, Denmark*, J.V. Andersen, H. Bohr and O.G. Mouritsen, *Department of Structural Properties of Materials, The Technical University of Denmark, Denmark*)

A minimum model is proposed to explain the variation of the superconducting transition temperature T_c with oxygen content x of the ceramic superconductor $YBa_2Cu_3O_{6+x}$ (YBCO). The model is based on the simple assumption that only ordered clusters exceeding a certain size, called *M*inimal *S*ize *C*lusters (MSC), can contribute to the charge transfer creating the holes in the necessary for superconductivity CuO_2 planes. The clusters considered are the domains of coherent orthorhombic structures OI and OII, forming thermodynamically stable phases of the material (*cf.* contribution 1.20 of this annual report). The MSC giving rise to charge transfer are taken to consist of 4×4 and 8×8 oxygen sites for the OI and OII clusters respectively. The cluster statistics needed as input to the model is calculated from Monte Carlo computer simulations on a 2D next-nearest-neighbour lattice gas model of oxygen in the basal plane (the socalled ASYNNNI model). From the simulations the relative numbers of oxygen sites belonging to the MSC of the two structural types OI and OII are determined. Assuming that T_c increases linearly with the charge transfer and that the charge transfer from the two structural types lead to superconductivity with T_c equal to 90 K and 60 K, respectively, we have established the T_c versus x curve by weighting the relative numbers of oxygen sites belonging to the two MCS with the corresponding T_c values. The comparison between the model calculation and the experimental data obtained by Cava et al.[1] is shown in Fig. 1. The agreement is striking. The result supports the conclusion of strong correlations between structural and superconducting relaxation phenomena observed by Jorgensen *et al.* [2], and suggests a simple and direct way of quantifying the influence of structural order on superconductivity.

The relaxation phenomena observed by Jorgensen et al.[2] on a sample of $YBa_2Cu_3O_{6.41}$ after being quenched from high temperatures have been studied by Monte Carlo simulations based on the ASYNNNI model. We find that the ordering dynamics obey the algebraic growth law: $L(t) \propto t^n$, where L is the length scale of structurally ordered clusters and t is time. In the OI phase we find $n \simeq 1/2$, while $n \simeq 1/4$ in the OII phase (see Fig. 2). The result from the OII phase is adequate for comparison with the experimental data obtained by Jorgensen *et al.*[2]. A reanalysis of their T_c data shows algebraic growth with $\Delta T_c \simeq t^{-1/2}$, that is: $\Delta T_c \propto L(t)^{-2}$ (see Fig. 2). This observation strongly support the basic idea of our minimum model, which suggests that the total number of oxygen sites belonging to the MSC determines the charge transfer and the superconducting transition temperature. The possibility that the basal plane oxygen atoms in $YBa_2Cu_3O_{6+x}$ form an ideal model system for studies of ordering dynamics in 2D is put forward.

[1] R.J. Cava *et al.*, (1988). Physica C **156**, 523, and (1990). Physica C **165**, 419.
[2] J.D. Jorgensen *et al.*, (1990). Physica C **167**, 571.

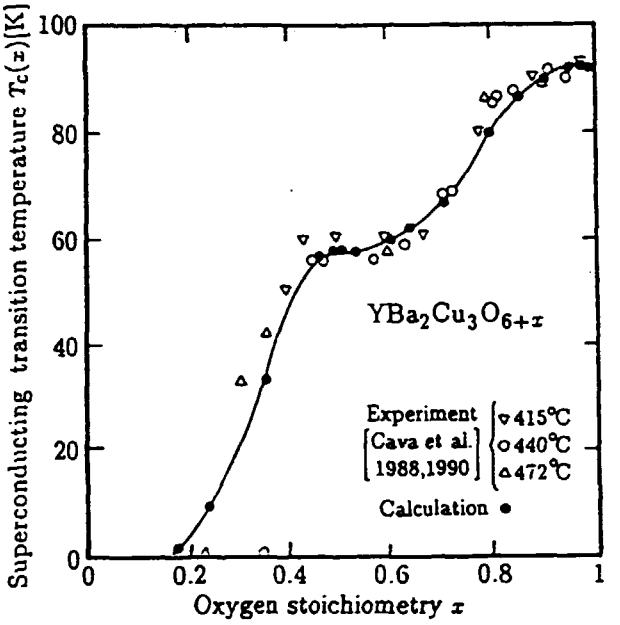

Fig. 1. Superconducting transition temperatures of $YBa_2Cu_3O_{6+x}$. Open symbols are experimental values obtained by Cava et al.[1], and the full curve is a guide to the eye of the minimum model results obtained by Monte Carlo simulations (•).

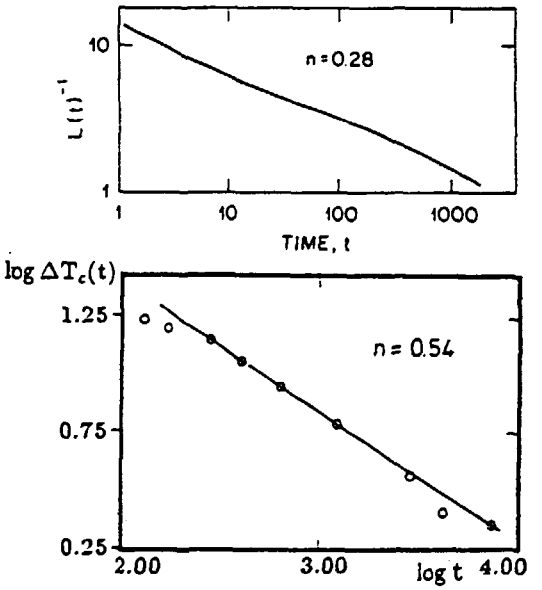

Fig. 2. Dynamics of oxygen ordering and time evolution of the superconducting transition temperature of $YBa_2Cu_3O_{6.41}$. The lower figure is a reanalysis of the experimentally observed temporal variation of the superconducting transition temperature ΔT_c obtained by quenching to 300 K [2]. The upper figure is the Monte Carlo result of the evolution of the cluster inverse length scale L^{-1} with time t. The best fits to the growth law exponents are marked on the figures.

1.22 Magnetic Correlations in Superconducting $YBa_2Cu_3O_{6+x}$

(G. Shirane, J.M. Tranquada and H. Chou, *Brookhaven National Laboratotory, Upton, New York, USA*, S. Shamoto and M. Sato, *Institute for Molecular Science, Okazaki, Japan*, J. Als-Nielsen and M. Nielsen, *Physics Department, Risø National Laboratory, Denmark*)

The spin correlations in high T_c superconducting $YBa_2Cu_3O_{6+x}$ has been studied by inelastic neutron scattering. Three large single crystals were used with oxygen concentrations x between 0.4 and 0.5, giving superconducting transition temperatures at 25, 45, and 50 K. In the x *vs.* temperature - phase diagram the three samples are represented by points in the superconducting phase region, but the points are close to the region of long range magnetic order.

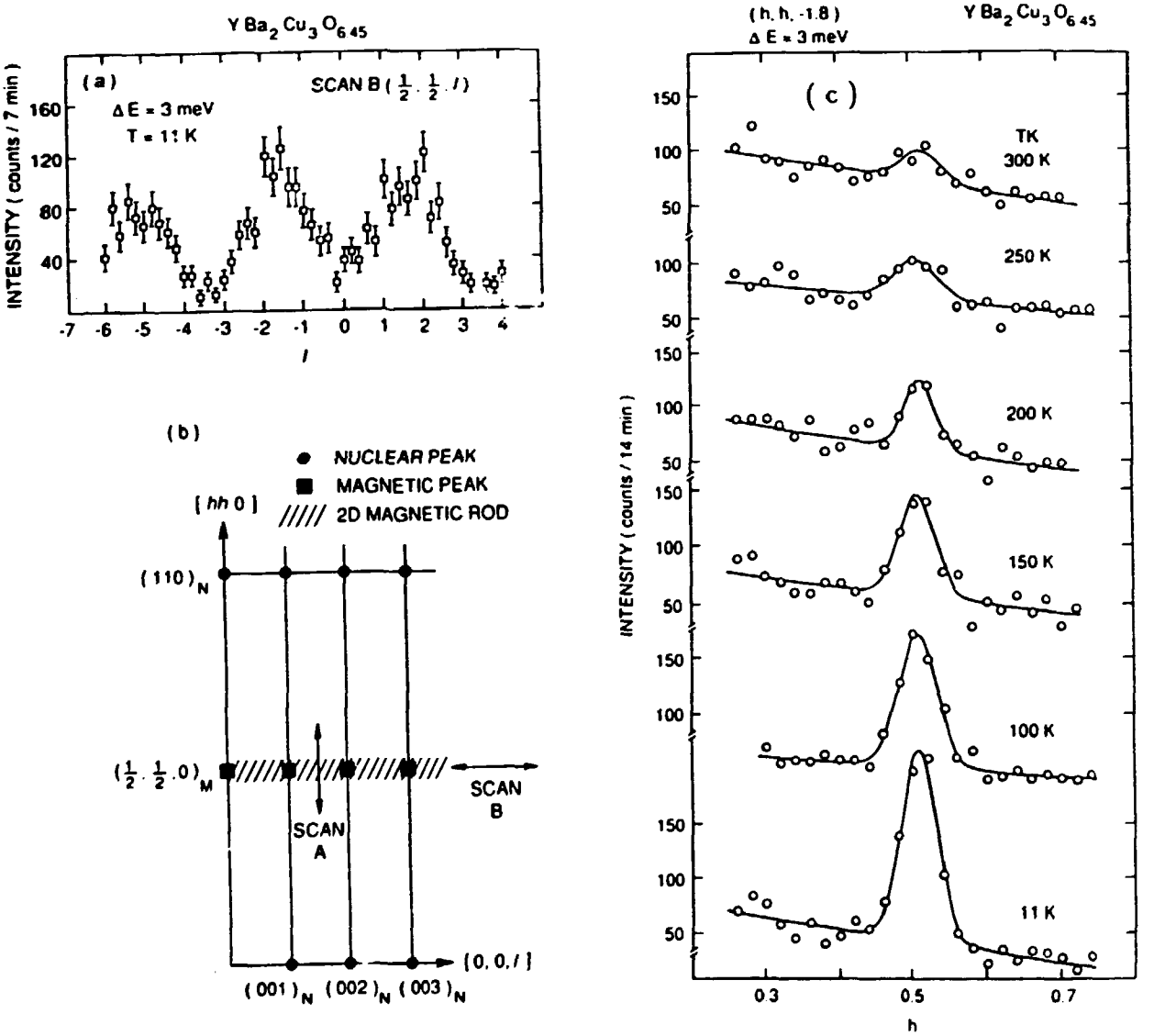

The aim of the present measurements has been to study how the magnetic correlations, present in the magnetic ordered phase, extends into the nonmagnetic superconducting phase.

Fig. 1c shows inelastic neutron scattering groups for the crystal with T_c =45 K, and it demonstrate the existense of magnetic correlations in the superconducting phase. The scattering was found to depend strongly on temperature and oxygen concentration x. The neutron scattering groups are measured in constant energy scans along the Q-direction shown as scan A in Fig. 1b. The magnetism in $YBa_2Cu_3O_{6+x}$ originates from unpaired spins in the CuO_2 double layers, and the coupling between different double layers is very weak. Therefor scan A (Fig. 1b) across the $(\frac{1}{2}\ \frac{1}{2}\ l)$ line characterizes the two dimensional correlations within the CuO_2 double layers, whereas scan B (Fig. 1b) along the ridge $(\frac{1}{2}\ \frac{1}{2}\ l)$ perpendicular to the CuO_2 layers only show the modulation given by the separation of the two CuO_2 layers of a bilayer. Fig. 1a illustrate such a scan (scan B of Fig. 1b). No long range magnetic order exists in these crystals, and the magnetic peaks referred to in Fig. 1b indicate the Bragg peaks of the ordered magnetic phase at $x < 0.4$.

1.23 Preparation of High-T_c Superconductors by RF Sputtering

(R. de Reus, R.F. Kromann and N.H. Andersen, *Physics Department, Riso National Laboratory, Denmark)*

The program on preparation of thin-film high-T_c superconductors is concentrated on epitaxial growth of $YBa_2Cu_3O_{6+x}$. This compound exhibits a critical temperature greater than the boiling point of liquid nitrogen and is relatively easy to synthesize. For reliable applications in microelectronics, superconducting thin films should not only be of submicron dimensions but also be able to carry high current densities of at least 10^{10} A/m^2. These requirements can be obtained by using single-crystalline superconducting thin films, which are grown epitaxially with respect to the preferably single crystalline silicon substrate. However, the high reactivity of the superconductor and the high processing temperatures of 700 to 900 °C make semiconductor substrates disadvantageous.

An RF sputtering technique was developed at Risø to prepare superconducting $YBa_2Cu_3O_{6+x}$ thin films without the need of post-annealing at 900 °C in oxygen ambient. This deposition method allows homogeneous deposition over relatively large areas (in our case 4×4 cm^2) of films with a thickness as thin as one unit cell (<12 Å). Stoichiometric cylindrical targets are used. Experiments with this sputter configuration started this summer and resulted in films of significantly higher quality than those obtained by the standard planary target geometry. $YBa_2Cu_3O_{6+x}$ films with a thickness of approximately 1 μm were grown epitaxially on (100) MgO substrates. As prepared the films showed an onset of superconductivity at 90 K. However, zero resistance was only obtained below 72 K, which is about 15 K lower than the best values reported in literature for films deposited on the same substrate material. The obvious reason is that our films are not stoichiometric, but contain impurity phases such as Y_2BaCuO_5. Furthermore, a substrate heater has been developed which allows heating up to 900 °C in 1 atm oxygen pressure.

Analysis techniques include X-ray diffraction (using both powder and four-circle diffractometry), scanning electron microscopy, and transmission electron microscopy for structural analysis. Furthermore, energy dispersive X-ray absorption analysis and chemical methods are applied for compositional analysis. Electrical characterization is performed using a four-point probe technique. Occasionally, Rutherford backscattering spectrometry is used for compositional depth profiling in collaboration with other laboratories.

During the year the RF-sputter equipment has been moved from the Department of Materials Science to the Physiscs Department to be integrated into the facilities for studies on thin films and surfaces. Recently the experiments were resumed. Future plans include firstly the preparation of high quality superconducting $YBa_2Cu_3O_{6+x}$ thin films (critical temperatures >85 K and critical currents of $\approx 10^{10}$ A/m^2) on (100) MgO substrates. Secondly, multilayer structures will be grown, consisting of alternating superconducting and electrically insulating layers of thicknesses down to unit cell dimensions. Also, epitaxial buffer layers will be deposited onto silicon substrates to minimize interdiffusion with superconducting $YBa_2Cu_3O_{6+x}$ overlayers. Studies of correlations between structure and electrical properties of films and multilayers are of primary interest in the program.

1.24 Measurement of Texture in YBCO Thin Films

(R. Kromann, R. de Reus and N.H. Andersen, *Physics Department, Risø National Laboratory, Denmark*)

In continuation of the activities reported last year we have performed X-ray diffraction experiments using a four-circle diffractometer on several $YBa_2Cu_3O_7$ films fabricated by laser ablation at NKT Corporate Research Center. In one experiment four films on MgO substrates were investigated of which two have a critical current density $J_c < 10^5$ A/cm^2 and the other two have $J_c > 10^6$ A/cm^2. Although a longitudinal scan indicates that all four films grow with the *c*-axis perpendicular to the substrate the pole figure measurement reveals that the low-J_c films have regions where the *a*- and *b*-axes are misaligned 45° with respect to the substrate. No misaligned regions were found in the high-J_c films. Other groups have observed this 45° misalignment also, but so far no theory exists to explain this phenomenon. Recent experiments done by NKT indicate that the problem is related to the quality of the substrate surface.

In another experiment three films on $SrTiO_3$, MgO and $LaAlO_3$ substrates were investigated. The critical current densities are 2×10^6 A/cm^2, 2×10^6 A/cm^2 and 5×10^6 A/cm^2, respectively. Generally, films on $SrTiO_3$ and $LaAlO_3$ exhibit a greater J_c than films on MgO, but the film on $SrTiO_3$ in this case is not of the best quality. The pole figure indicates very small amounts of 45° misaligned material in the film on MgO, but not on $SrTiO_3$ and $LaAlO_3$ substrates. A much larger difference between the films is found in a χ-scan on the YBCO (102)-reflection (χ is one of four variable angles in a four-circle diffractometer). This type of scan allows a determination of the relative abundance of film with the *c*-axis in the substrate plane because the (102)-reflection will show up at χ_1=56.6° or χ_2=90°-χ_1=33.4° depending on whether the *c*-axis is perpendicular or parallel to the substrate. We find that 9%, 3% and 1% of the film grows with the *c*-axis in the plane in the three cases, respectively. We may thus conclude that true epitaxial growth of the film on the substrate is of paramount importance in obtaining a high J_c and that any deviations from this behaviour such as rotations in the $a-b$ - plane and/or interchange of the *c*-axis with the $a-b$ - axes seriously degrade this crucial transport property.

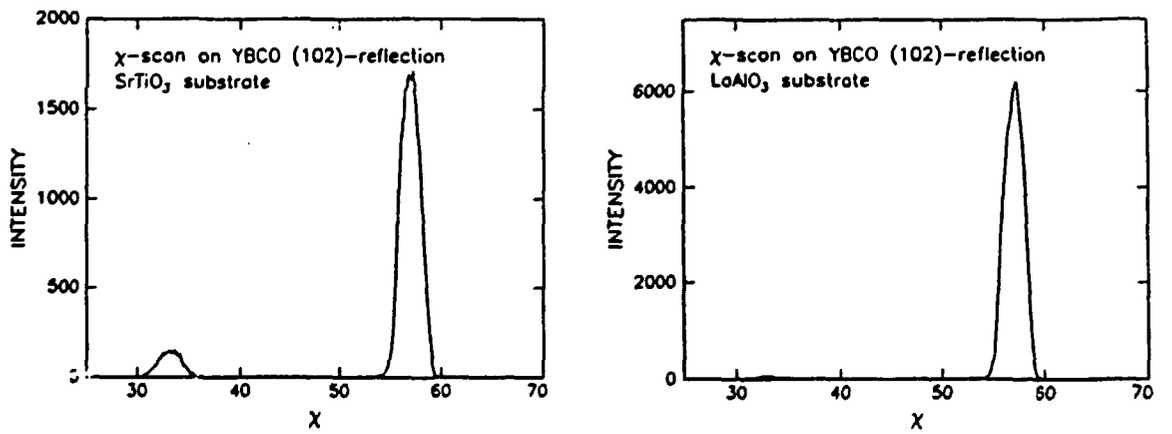

Left: χ-scan of a film with $J_c = 2 \times 10^6$ A/cm^2 and frequent occurence of the c-axis in the substrate plane. Right: χ-scan of a film with $J_c = 5 \times 10^6$ A/cm^2 and containing almost no material with the c-axis in the plane of the substrate surface.

1.25 Melting, Growth and Faceting of Lead Precipitates in Aluminium

(L. Gråbæk, J. Bohr, *Physics Department, Riso National Laboratory, Denmark*, H. H. Andersen, A. Johansen, E. Johnson, L. Sarholt-Kristensen, *Physics Laboratory, H.C. Ørsted Institute, Copenhagen, Denmark* and I. K. Robinson, *AT & T Bell Laboratories, Murray Hill, USA*)

Small precipitates of Pb in aluminium single crystals have been studied by X-ray diffraction. We focussed our investigations on melting solidification and growth of the precipitates and on phenomena at the interface between lead and aluminium.

Fig. 1 shows data from an X-ray diffraction experiment. The streak/rod of intensity originates from the (111) facets of the lead inclusions and such a streak/rod was also observed from the (100) facets. The integrated intensity in the (111) and (100) rods behave differently as a function of temperature. The difference indicate that the (100) facets premelt or roughen at 605±3 K which is ~ 15 K below the temperature where the inclusions start to melt and also the signal from the (111) facets start to vanish.

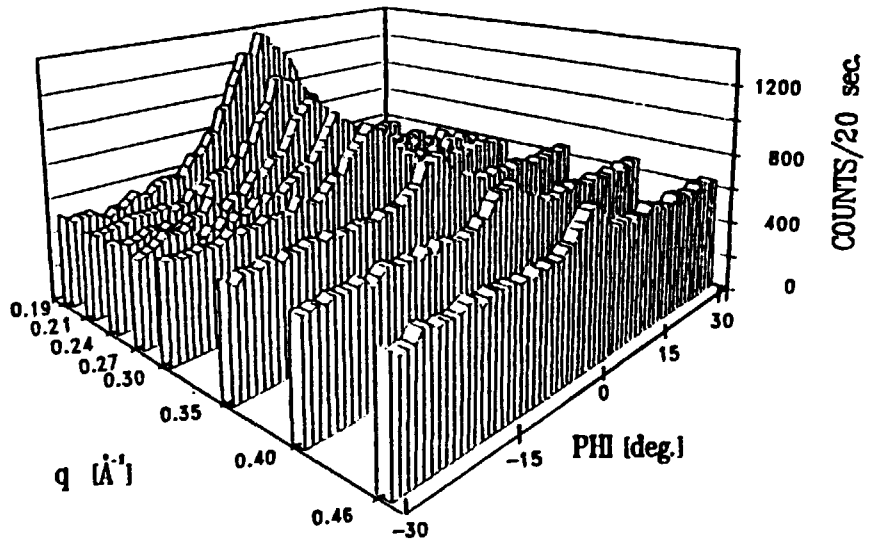

Fig. 1. Three-dimensional plot of the truncation rod originating from (111) facets at the lead inclusions, at 303 K. The scans in the plot are across the $[\bar{1}\bar{1}1]$ *direction, away from the lead (111) peak. q is the distance from the center of the scan (PHI = 0) to the center of the lead (111) peak, PHI is the angle that the sample is turned away from the* $[\bar{1}\bar{1}1]$ *direction.*

Superheating, is not normally observed for metal crystals with a free surface. However, in our study of small faceted, epitaxially oriented lead crystallites, which do not have a free surface, superheating as high as 67 K was observed. We also observed supercooling in this system, at least 18 K. The main contributions to the superheating are most likely to be the lack of a free surface and the epitaxial alignment between the inclusions and the host matrix.

To initiate melting it is necessary to create some disorder at the surface, *e.g.* by expelling an atom to the surface. In comparison to the normal situation with a free surface, a higher energy is needed to expell an atom to the surface here, since the surface is covered with aluminium. The crystallites gain some energy by the epitaxial alignment, this increases the energy barrier for melting by the same amount. Other effects may contribute to the higher melting point, *e.g.* the fact that the crystallite surfaces are primarily (111) surfaces (facets), as such surfaces do not exhibit premelting. Furthermore a pressure above ambient can not be completely ruled out, although, the measured lattice parameter is in agreement with the tabulated value for bulk lead. However, taking the worst case within the uncertainty of our data, the pressure would at most increase the melting temperature by 14 K.

Analyzing the relation between the melting temperature for the inclusions (T_r) and their size r, we find that the superheating vanishes asymptotically as $r \rightarrow \infty$. And the most likely relationship is $T_r \propto 1/r$, this indicates that the surface to volume ratio determine the melting temperature. The combined contribution from the lack of free surface, the epitaxial alignment, the extended (111) facets and a pressure above ambient stabilize the superheated state, so it may in fact be stable. However, we note that homogeneous nucleation of the melt in the superheated state would also lead to a $1/r$ relationship, and would imply that the superheated state is only metastable!

The supercooling is due to the size of the inclusions, the critical grain size for nucleation of the solid at a given temperature first matches the actual inclusion size at the temperature where the inclusions start to solidify.

With one sample we performed an isochronal annealing sequence to study the inclusion growth. Here a sample was heated to a given temperature, kept at that temperature for 90 minutes, then cooled to room temperature where measurements were performed. This process was repeated for a series of temperatures in the range 300-688 K. At 688 K all the lead in the inclusions are melted. We found that the inclusion growth was closely connected with the lead being in the molten state. Figure 2 shows the FWHM for the lead (111) peak, the discontinuity at around 600 K, indicates that there is a discontinuity in the inclusion growth rate at this temperature, as FWHM $\propto 1/r$. This indicates that the prime mechanism for inclusion growth is coalescence of inclusions.

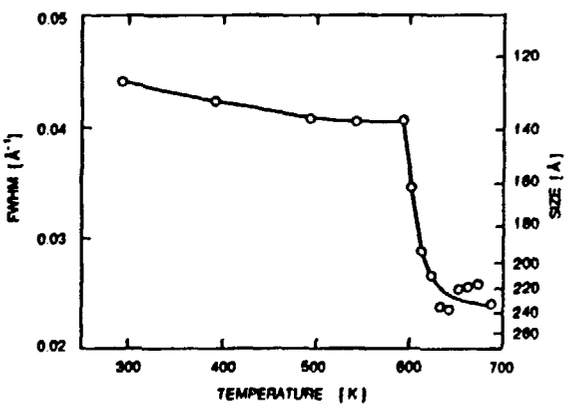

Fig. 2. Full-Width-at-Half-Maximum for the (111) lead peak (raw data), versus annealing temperature. The measurements were performed at room temperature, after cooling the sample from the temperature indicated.

1.26 Sputtering Yields and Energy Distributions from Ion-Bombarded Condensed Gases

(J. Schou, *Physics Department, Risø National Laboratory, Denmark*, B. Stenum and H. Sørensen, *Optics and Fluid Dynamics Department, Risø National Laboratory, Denmark*, O. Ellegaard, *Odense University, Denmark*, and R. Pedrys, *Institute of Physics, Jagèllonian University, Crakow, Poland*)

The studies on sputtering of the solid hydrogens have been continued at the existing setup. The collection of data for the sputtering rate of solid deuterium by hydrogen ions from 5 to 10 keV has been considerably extended. The data are important for the lifetime of fast fuel pellets of solid deuterium injected into the fusion devices. The fast hydrogen ions generated by the neutral beam heating are very efficient in eroding the deuterium pellets, since these high-energy ions in contrast to the thermal plasma particles easily penetrate the protecting gas cloud around the pellet. The sputtering yield for a 10 keV H^+ is about 150 D_2/H. This high yield is primarily caused by the low binding energy , 12 meV, of the deuterium molecules in the solid.

The yield of solid deuterium is increasing with the energy of the primary ion, a proton, a diatomic or triatomic hydrogen ion. The key quantity is the electronic stopping power of the projectiles. The total yield is determined by the sum of the stopping powers of the individual atoms in the projectile. The reason is that the atoms in the molecule are so close to each other during the passage of the first layers in the surface that one may regard a molecule as one primary particle with a stopping power equal to the sum of the the stopping power of the atoms. Then, the yield turns out to behave like a power of the total stopping power with an exponent between two and three. Actually, this behaviour is similar to the yield of solid nitrogen, which is the most volatile molecule apart from the hydrogenic molecules. This scaling with the total electronic stopping power allows us to predict the sputtering yield of protons with energy up to about 50 keV, which actually is close to the energies of the stopping power maximum.

The setup was modified by a special soldering point from the cryostat bottom to the electrode of the quartz crystal microbalance. Then the microbalance became so cold that it was possible even to erode films of solid hydrogen and deuterium hydride on it. Films of solid hydrogen have not been studied systematically before because of the extreme volatility. It turned out that it was possible to avoid beam-induced evaporation for beam currents below 4.5 nA. The sputtering yield for solid hydrogen and deuterium hydride shows the same energy dependence as solid deuterium does. The absolute value of the yield from solid hydrogen is about a factor of four larger than for solid deuterium because the binding energy of the molecules is somewhat smaller than that for deuterium.

1.27 Luminescence from Pure and Impure Solid Hydrogens during Electron Bombardment

(J. Schou, *Physics Department, Risø National Laboratory, Denmark*, B. Stenum, H. Sørensen, *Optics and Fluid Dynamics Department, Risø National Laboratory, Denmark*, P. Gürtler, *Hasylab, DESY, Hamburg, Germany*, and R. Brooks, *Department of Physics, Guelph University, Guelph, Canada*)

The study of luminescence from particle-irradiated solid deuterium does not only yield information about how the electronic excitations relax in the solid, but provide also important data for the pellet-plasma interaction. A material that emits a strong luminescence is expected to have a larger lifetime in a plasma than one without luminescence, because a considerable fraction of the deposited energy is released from the solid. Unfortunately, it turned out that the luminescence per incident electron from solid deuterium and hydrogen is weaker than from any other known condensed gas.

The previous setup was improved so that the photon detection in the VUV-regime was more efficient. The two LiF-lenses were replaced by specially coated VUV-mirrors with relatively high reflectivity around 150 nm. The photon detection was performed with a Mc Pherson VUV-monochromator equipped with a solarblind photomultiplier. Even though the setup was optimized to the regime close to Lyman-α, the detection was fairly good with a suitable photomultiplier up to about 900 nm.

The studies were mainly concentrated on the possible detection of Lyman-α in electron-irradiated solid deuterium or deuterium-neon mixtures. It is a paradox that one of the most (if *not* the *most*) common lines in the Universe never has been observed in a environment of solid hydrogen. A previous observation of Lyman-α induced by lower intensity than ours from the literature was apparently caused by an impurity rather than by an intrinsic deexcitation in pure deuterium or in deuterium-doped neon. No Lyman-α signal, which is expected to lie relatively closely to the gas value at 121.6 nm, was observed. The reason for this somewhat surprising result is that the active excited "Lyman-α"-atom is quenched by the large population of D_3^+ ions and D_3^*-neutrals with low-lying electronically excited states in a deuterium matrix. In solid neon doped with a low amount of deuterium D_3-complexes are not generated. Unfortunately, the possible Lyman-α excitations are quenched by metastable neon-deuteride that emits a strong continuum around 230 nm. One may not expect emission of Lyman-α light from deuterium in other regular condensed gases since they all have (intrinsic) electronically excited states below the Lyman-α level.

As a minor result this neon-deuteride continuum has been observed for the first time in a solid. This metastable molecule has so far only been observed in gas-phase experiments since the ground state of the molecule is not stable.

1.28 Two Dimensional Solids and Liquids Influenced by a Small Corrugation Potential: A Monte Carlo Simulation Study

(P.-A. Lindgård, *Physics Department, Riso National Laboratory, Denmark*, and E. Vives, *University of Barcelona, Spain*)

A general, continuous model for two dimensional solids and liquids on a substrate is developed and studied by means of Monte Carlo simulation for 2700 particles, subject to a Lennard-Jones interaction and a substrate potential, the socalled corrugation potential U. The results can be applied to the case of adsorbed atoms or molecules on surfaces as well as intercalated compounds and several other surface problems. We have focused on the study of the melting of a commensurate $\sqrt{3} \times \sqrt{3}$ structure on a triangular lattice with 1/3 coverage. As an example we show in Fig. 1a the melted phase and 1b the solidified phase for the case of zero corrugation potential, $U = 0$. This demonstrates *e.g.* the isotropy of our simulation. In particular we have investigated the contribution from the two dimensional liquid to the Bragg peaks corresponding to the substrate structure. Reiter and Moss have demonstrated that this gives valuable information about the substrate potential. We have further studied this and found a new universal dependence between the intensity (Debye-Waller factor) and the particle fluctuations around the substrate potential wells. This dependence may be useful for an experimental determination of the magnitude of the substrate potential from scattering experiments, in particular for weak potentials and large atomic mean square displacements.

[1] G. Reiter and C. Moss,(1986). Phys. Rev. B **33** , 7209.

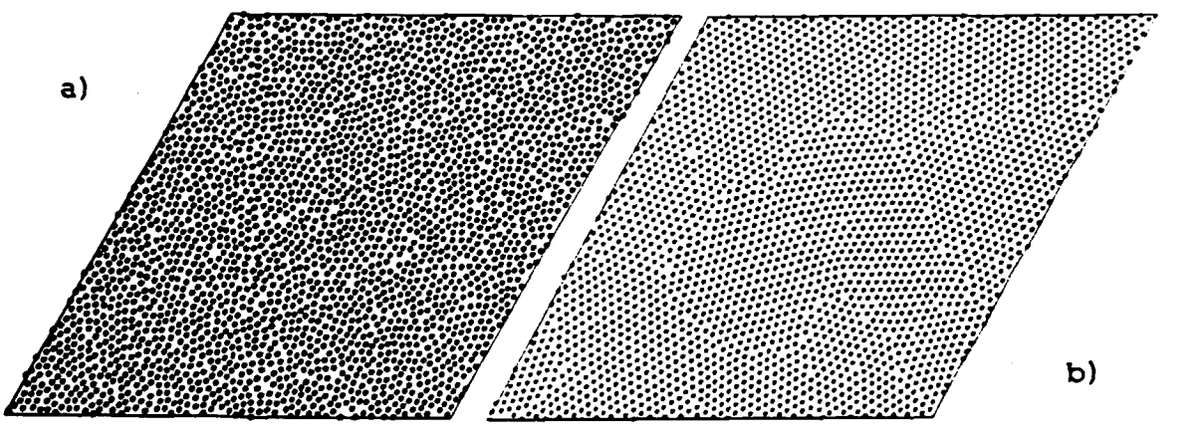

Fig. 1. a) the melted phase for 2700 particles. b) the corresponding solidified phase.

1.29 Large Corrugation Potential Effect on Two Dimensional Solids and Liquids: A Continous Monte Carlo Simulation Study towards the Potts Model

(P.-A. Lindgård, *Physics Department, Riso National Laboratory, Denmark*, and E. Vives, *University of Barcelona, Spain*)

Two limiting cases have usually been discussed in order to characterize the substrate influence on an atomic monolayer. The first assumes that the corrugation potential U is large, so that the system can be considered as a lattice gas or liquid in which the motion of the particles is restricted to a jumping between neighbouring wells, while the motion within the substrate potential wells is not considered. In this limit several theories concerning modified Potts models have been developed, discussing mainly the symmetry change between the solid and liquid phase. The Potts model is a lattice gas model which just describes the presence of atoms at the minimum energy sites of the substrate. Some of the theories seem to be in agreement with the phase diagram for Kr adsorbed on graphite. Very few calculations of the structure factor $S(q)$ have been performed for these models. Instead of the usually employed molecular dynamics method, we have developed a continuous Monte Carlo method, which allows the possibility of studying much larger systems up to 2700 atoms or more, thereby considerably reducing the finite size effects on $S(q)$. Here this study is extended by considering very large corrugation potentials, as a step towards unifying the Potts lattice description and the continuous, perturbed liquid description, which is needed in order to understand the influence of the substrate on the two dimensional solids and liquids. For large U a contracted, incommensurate liquid is found which is not at all resembling a centered Potts model. A calculation of the free energy shows that a relaxed liquid with the particles displaced in the potential wells is preferable due to the entropy gain. Nevertheless this liquid can in a cellular sense be described as a Potts lattice gas liquid. It is found that these features do show up in the structure factor $S(q)$, but only detectable as small shifts of peak positions, and intensities.

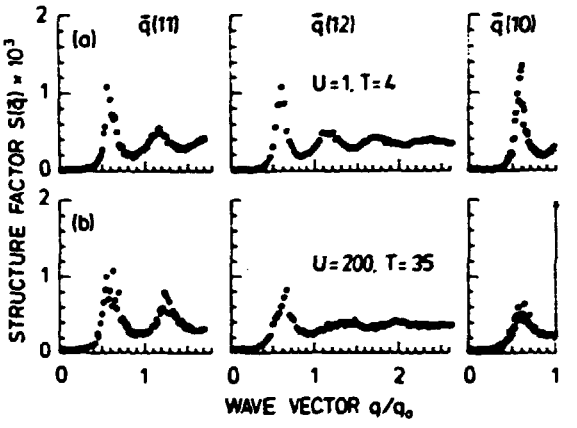

Fig. 1. Structure factor for:
a) liquid with small corrugation potential U=1, T=4;
b) liquid with very large corrugation potential U=200, T=35.

1.30 Pinning Effects on Domain Growth Kinetics

(P.-A. Lindgård, *Physics Department, Risø National Laboratory, Denmark*, and T. Castán, *University of Barcelona, Spain*)

By means of Monte Carlo computer simulation we study the domain growth kinetics after a quench across a first order line to very low and moderate temperatures in a multi-degenerate system with non-conserved order parameter. The model is a continuous spin model with general applicability. It is relevant for martensitic transformations, surface reconstructions and magnetic transitions. Although by now very much is known about the ordering kinetics of simple models as the Ising -, the Potts - and the ANNNI model and also about the effect of quenched (immobile) impurities and random fields, the effects of annealed (mobile) defects on the time evolution has received relatively little attention. The latter are often more realistic and therefore important in experimental situations. Our model has a number of intrinsic, annealable pinning mechanisms, which strongly influences the growth kinetics. It allows a study of pinning effects of three kinds: a) pinning of domain walls by defects, b) temporary pinning by stacking faults or zero-curvature domain walls and c) topological pinnings due to particular geometry of domain wall intersections. The pinning mechanisms and the depinning probability at higher temperatures are studied. A snapshot showing a number of pinning centers on domain walls is shown in Fig. 1. The excess energy of the domain walls is found to follow an algebraic decay $\Delta E(t) = E_M + At^{-n}$, with $E_M = 0$ for case b) and c) and decaying towards a metastable state with energy $E_M \neq 0$ for case a). The exponent is found to cross over from $n = 1/4$ at $T \sim 0$ to $n = 1/2$ with temperature for models with pinnings of type a) and b). For topological pinnings at $T \sim 0$, n is consistent with $n = 1/8$, a value conceivable for several levels of hierarchically interrelated domain wall movements. When the continuous spin model is reduced to a discrete Potts-like model, with the same parameters, the exponent is found to be consistent with the classical Allen-Cahn exponent $n = 1/2$.

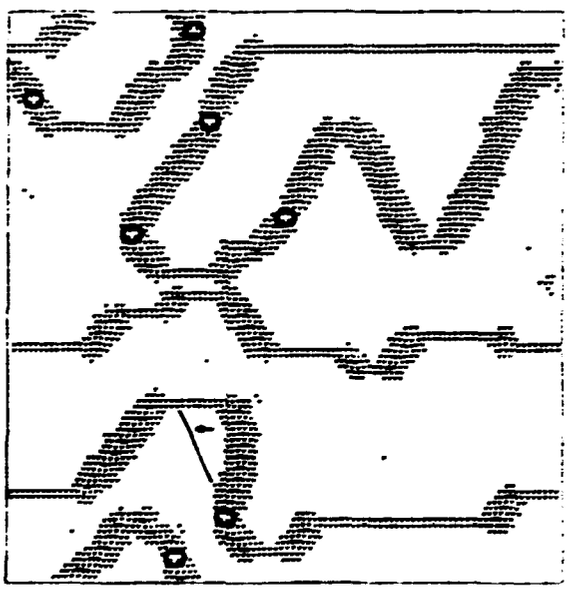

Fig. 1. Snapshot of domain walls with pinning centers (○) formed by oppositely turning domain walls. The white areas represent different antiferromagnetic domains of two kinds. The deviating spins in the domain walls are shown by small dots.

1.31 A Symmetry Principle for Epitaxial Rotation

(F. Grey and J. Bohr, *Physics Department, Riso National Laboratory, Denmark*)

We propose that a simple symmetry principle underlies the phenomenon of epitaxial rotation, where a crystalline adsorbate is rotated through a low-symmetry angle relative to the crystal axes of the substrate. The principle is that the domain structure, produced by the beating of the incommensurate adsorbate and substrate lattices, tends to align along a high-symmetry direction of either the adsorbate or the substrate.

Fig. 1a shows the domain structure formed by two incommensurate lattices superposed on each other with their principal axes aligned. In Fig. 1b, one of the triangular lattices has been rotated a small angle θ relative to the other. As a result, the domain structure has rotated by 30° - a high-symmetry angle - relative to Fig. 1a. This effect is characteristic of moiré patterns, which magnify relative translations and rotations of the lattices that generate them. It is straightforward to derive an expression for θ in terms of r_{AS}, the ratio of the adsorbate and substrate lattice parameters, and ψ_A, the high-symmetry rotation angle of the domain lattice relative to the adsorbate lattice.

$$\cos\theta = r_{AS}^{-1}\sin^2\psi_A + \cos\psi_A\sqrt{1 - r_{AS}^{-2}\sin^2\psi_A} \qquad (1)$$

In Fig. 2, this dependence of θ on r_{AS} is shown for ψ_A =30°,60°, two high symmetry rotations of the domain lattice. Experimental data for Na/Ru(100)[1] and D_2/graphite[2] are seen to agree very closely with the high symmetry solutions, where r_{AS} =1 corresponds to the commensurate $\sqrt{3} \times \sqrt{3}$R30° structure.

[1] D. L. Doering and S. Semancik, (1984). Phys. Rev. Lett. 53, 66.
[2] J. Cui and S. C. Fain, (1989). Phys. Rev. B 39, 8628.

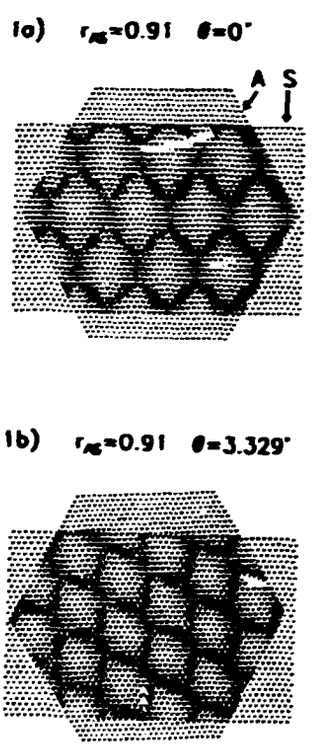

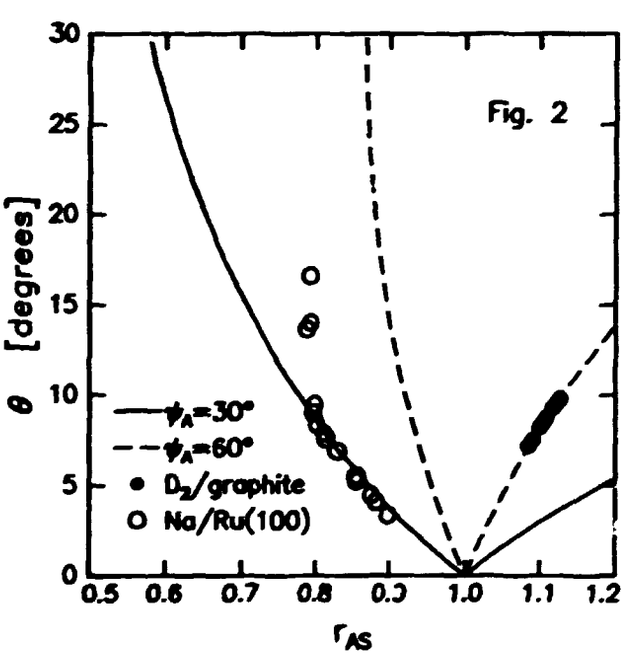

1.32 Numerical Simulations of Crystalline Epitaxy

(F. Grey and J. Bohr, *Physics Department, Riso National Laboratory, Denmark*)

We have employed a simple algorithm to study the effects of finite-size and adsorbate relaxation on the energetics of crystalline interfaces. We have considered the cases of fcc(111) (triangular) adsorbates on fcc(111) and bcc(110) substrates.

The adsorbate energy is calculated by summing three sine functions at each adsorbate atom position, the sine functions representing the fundamental Fourier components of the substrate potential. The adsorbate consists of some 7350 atoms in a hexagonal array with dense-packed [11] facets. In simulations where the adsorbate was relaxed, the new atom positions were calculated according to

$$(x_i', y_i') = (x_i, y_i) - \Delta\left(\frac{\partial V(x,y)}{\partial x}, \frac{\partial V(x,y)}{\partial y}\right) \qquad (2)$$

where Δ is typically a few percent of the interatomic distance. This form of relaxation avoids computationally cumbersome elastic coupling of atoms, but implicitly assumes an isotropic elastic restoring force on each atom.

We find that having well-defined facets on the adsorbate results in energy minima along lines in the space spanned by adsorbate mismatch and rotation (see Fig. 1). These lines are the solutions predicted on the basis of the symmetry principle we have proposed (see previous contribution). This implies that finite-size effects can drive epitaxial rotation, a physical origin of the phenomenon that has not been considered before.

Adsorbate relaxation is found to stabilize low-order commensurate structures. In particular, in the case of fcc(111)/bcc(110), we find that a low-order commensurate structure, recently observed experimentally for Ce(111)/V(110)[1], forms an energy basin in our calculations. Several other similar energy basins are observed, suggesting novel epitaxial relationships which have not yet been observed.

[1] H. Homma, K. Y. Yang and I. K. Schuller, (1987). Phys. Rev. B **36** 9435.

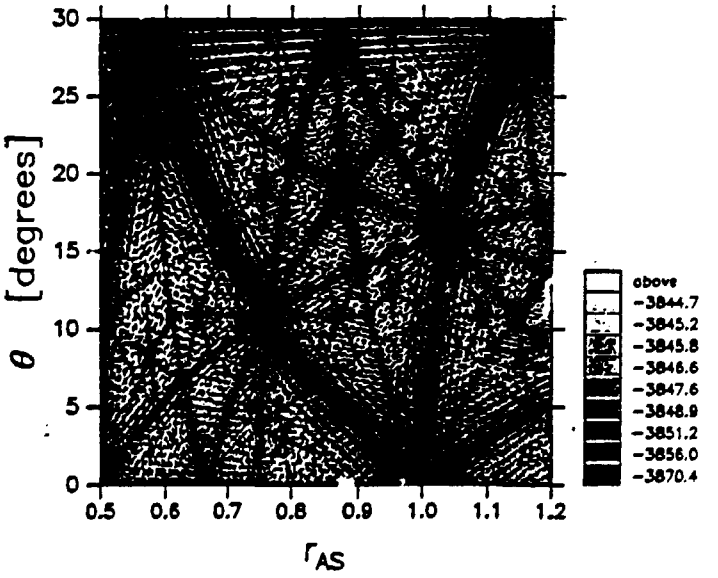

Fig. 1. Contour plot of calculated energy surface as a functions of mismatch and rotation of a triangular overlayer on on a triangular substrate.

1.33 Cu/Si(111) 5.6×5.6: A Silicide Precursor

(F. Grey, R. Feidenhans'l and M. Nielsen, *Physics Department, Risø National Laboratory, Denmark*, R. L. Johnson, *II Institute für Experimentalphysik, Universität Hamburg, Germany* and J. Zegenhagen, *Max Planck Institut für Festkörperforschung, Stuttgart, Germany*)

We have investigated the incommensurate 5.6 x 5.6 structure of Cu on Si(111) by surface X-ray diffraction. The main feature in the diffraction pattern is a pair of intense incommensurate reflections rotated ±3.1° relative to the bulk Si(220) reflection. This implies that, in units of the Si substrate, the surface has a domain structure, the domain spacing being 5.6 in units of the substrate lattice, and the domains being rotated ±3.1° relative to the substrate high symmetry axes.

The internal structure of the domains must be simple, since one peak dominates the diffraction pattern of each domain type. Models for this internal structure were least-squares fitted to the measured structure-factor intensities. The best-fit model involves domains with a triangular structure of Cu and Si atoms. The Cu-Si bond length and the degree of rotation varies within the domain: at the center there is near-perfect registry with the substrate (quasi-1 × 1 structure).

The resulting structure represents an interesting case of epitaxial rotation of an adsorbate. This phenomenon is well-documented in physisorbed gases on graphite and alkali atoms on metal surfaces, but is otherwise unknown on semiconductor surfaces. The CuSi layer is a two-dimensional precursor of the three dimensional silicide that forms when many monolayers of Cu are deposited.

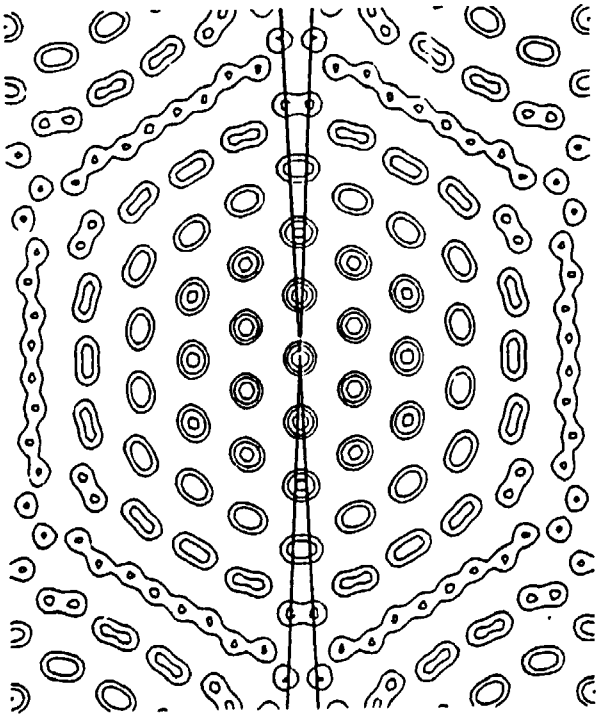

The electron density autocorrelation function of one 5.6×5.6 domain of Cu/Si(111). Domains rotated ±3.1° appear superposed, though in real space they are spatially separated on the surface.

1.34 Epitaxial Rotations of Metastable Clusters of Pb on Si(111) and Ge(111)

(F. Grey, R. Feidenhans'l and M. Nielsen, *Physics Department, Riso National Laboratory, Denmark*, R. L. Johnson, *II Institute für Experimentalphysik, Universität Hamburg, Germany*, H. Weitering and T. Hibma, *University of Groningen, The Netherlands*)

X-ray diffraction and scanning electron microscopy were used to investigate metastable Pb clusters adsorbed on Ge(111) and Si(111) at room temperature. The clusters were formed by deposition of Pb from a Knudsen cell on the clean semiconductor substrates, and the Pb(111) planes were parallel to the substrate (111) planes. In previous studies at room temperature using electron diffraction it was found that the Pb(110) planes are parallel with the substrate (110) planes. However, we observe by X-ray diffraction that a large fraction of the clusters are rotated, in the plane of the interface, through a small angle relative to the substrate [110]-equivalent directions.

In the case of Si(111), the epitaxial rotation angle is found to depend on the nature of the initial two-dimensional (2D) structure on which the clusters grow. Two different 2D structures can be formed, depending on whether or not the first deposited monolayer is annealed before further deposition of Pb to form the clusters. The unannealed 2D structure has a 7×7 unit cell, like clean Si(111), whereas the annealed 2D structure has a $\sqrt{3} \times \sqrt{3}R30°$ unit cell. For Ge(111), only the $\sqrt{3} \times \sqrt{3}R30°$ structure exists.

The epitaxial rotation angles are 4.5° for Ge(111), 6.1° for unannealed Si(111) and 3.[illegible]° for annealed Si(111). We have developed a quantitative explanation for the epitaxial rotation, in terms of the domain pattern generated by the overlapping Pb and Si or Ge lattices. A small rotation of the cluster will produce a large rotation of the domain pattern, a geometrical effect typical of moiré patterns. By considering small rotations of the clusters which produce large, high-symmetry rotations of the domain pattern, quantitative agreement with the measured epitaxial rotations is obtained.

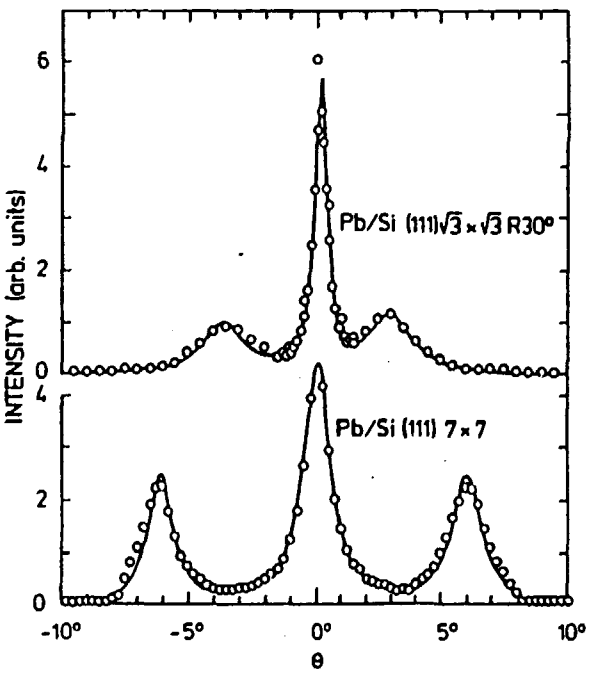

Azimuthal scan through the Pb(110) bulk reflection on Si(111). The central peak is from those clusters aligned with the substrate, the two other peaks are epitaxially rotated. The rotation angle is seen to depend on the surface structure on which the Pb clusters are grown.

1.35 Pb/Si(111): A Liquid Pb Monolayer at Room Temperature

(F. Grey, R. Feidenhans'l and M. Nielsen, *Physics Department, Riso National Laboratory, Denmark*, R. L. Johnson, *II Institute für Experimentalphysik, Universität, Hamburg, Germany*)

Pb/Si(111) is reported to have two phases with a $\sqrt{3} \times \sqrt{3}$R30° unit cell[1]. The low density phase has a simple structure with one Pb atom per $\sqrt{3} \times \sqrt{3}$R30° cell, and the high density phase is a close-packed Pb layer with four atoms per cell. Defining a monolayer (ML) as one Pb atom per surface Si atom, these phases have coverages of 1/3 and 4/3 ML. At intermediate coverages, no superstructure reflections are observed, and it has been suggested that Pb adopts a 1×1 solid phase. Our previous diffraction measurements showed that the high coverage $\sqrt{3} \times \sqrt{3}$R30° phase is in fact slightly incommensurate[2]. Also, for Pb/Ge(111), a similar system, no intermediate 1×1 phase was observed. Instead a coexistence of the two $\sqrt{3} \times \sqrt{3}$R30° phases was seen, with a triple line at 180 °C, well below the bulk melting temperature of Pb[3].

Desorbing small amounts of Pb, we observe that the disordering temperature of the incommensurate layer decreases as it becomes more dilute. Already at a coverage of 1.23 ML (as determined from the lattice parameter of the incommensurate layer), the main Bragg peak of the incommensurate phase is absent at room temperature. However, a broad, weak ring of scattering remains, similar to that seen for the liquid phase of Pb/Ge(111)[3]. Cooling the sample below room temperature, the main reflection of the incommensurate phase reappears, as shown in the figure. This behaviour is fully reversible. We conclude that at intermediate coverages between the two $\sqrt{3} \times \sqrt{3}$R30° phases, the Pb layer is in fact liquid at room temperature. We suggest that the phase diagram of Pb/Si(111) is analogous to that of Pb/Ge(111), but with a triple line below room temperature.

[1] M. Saitoh *et al.*, (1985). Surf. Sci. **154**, 395.
[2] F. Grey *et al.*, (1989). Journ. de Phys. Coll. **50**, C7-181.
[3] F. Grey *et al.*, (1990). Phys. Rev. B. **41**, 9519.

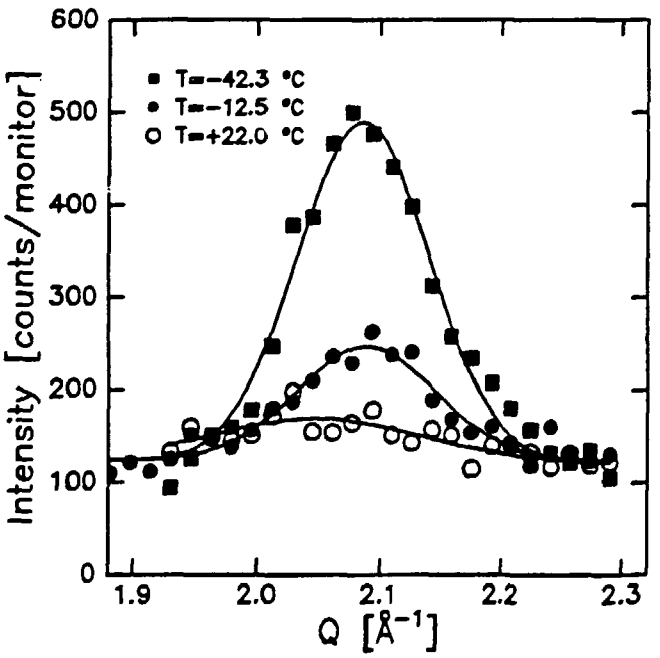

Radial scans through the position of the fundamental Bragg peak of the incommensurate phase of Pb/Si(111) at different temperatures for a coverage of 1.23 ML

1.36 Chemisorption of Oxygen on Cu(110): The c6×2 Structure

(R. Feidenhans'l, F. Grey and M. Nielsen, *Physics Department, Risø National Laboratory, Denmark*, R.L. Johnson, *II Institute für Experimentalphysik, Universität Hamburg, Germany*)

Oxidation of copper surfaces is presently of great interest. A very important aspect is the formation of Cu-O rows as found on the (100) surface for the $2\sqrt{2} \times \sqrt{2}$ structure and on the (110) surface for the 2×1 structure. On the (110) surfaces a 6×2 structure is formed at higher oxygen coverages. The relatively large unit cell makes a structural determination by conventional electron diffraction techniques untractable , so very little is known about the atomic structure and its relation to the Cu–O rows. We have studied this surface by means of surface X-ray diffraction at the W1 beamline in HASYLAB. In total, we have measured a set of 56 fractional-order and eight integer-order inequivalent in-plane reflections together with seven fractional-order rods and three Crystal Truncation Rods. The in-plane atomic structure – the structure projected onto the surface plane – was solved in a four step process.

(1) First the structure of the copper atoms was found on basis of a contour plot of the Patterson function and Scanning Tunneling Microscopy (STM) images from the Institute of Physics in Århus[1].
(2) Because copper (Z = 29) is much heavier than oxygen (Z = 8) the copper atom will dominate the phases of the structure factors. The oxygen atoms can therefore be found in a Fourier difference plot, a plot of the electron density difference between the real structure and the model structure.
(3) The atomic positions of both copper and oxygen atoms are refined in a least-square fit to the in-plane fractional-order reflections.
(4) The position of the surface layer relative to the bulk is found via the interference scattering of the surface layer and the bulk at the integer-order positions.

The basic elements of the structure is still Cu-O rows as found on the 2×1 surface, but they are more densely packed with a coverage of 2/3 monolayer compared to 1/2 for the 2×1 structure. The Cu-O rows has a 3×1 structure and are 'connected' by extra copper atoms. The latter atoms are responsible for the $c6 \times 2$ structure. 5/6 monolayer of copper atoms are displaced more than 0.25 Å away from ideal lattice sites. The oxygen coverage is 2/3 monolayer. The model is in very good agreement with the STM-measurements as well as effective medium calculations[1]. Due to the large number of free parameters the out-of-plane structure could not be determined by the X-ray diffraction data, but was instead taken from the effective medium calculations[1].

[1] R. Feidenhans'l, F. Grey, M. Nielsen, F. Besenbacher, F. Jensen, E. Lægsgaard, I. Stensgaard, K.W. Jakobsen, J.K. Nørskov and R.L. Johnson, (1990). Phys. Rev. Lett. **65**, 2027.

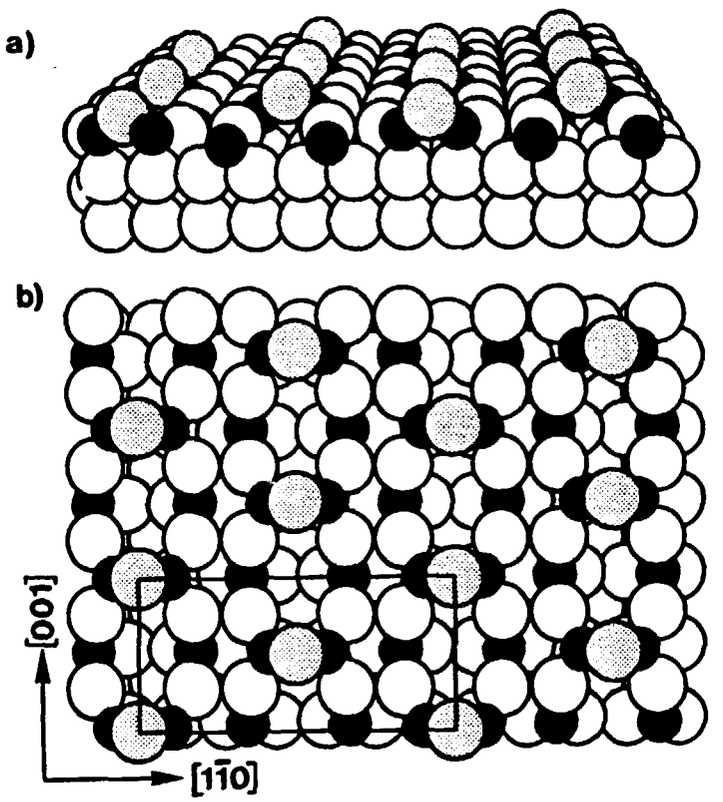

Perspective (a) and top (b) view of the Cu(110)c6 × 2-O structure. The small black circles represent the O atoms, whereas the grey and white circles represents the topmost Cu-atoms and the Cu-atoms in the layers below. The c6 × 2 unit cell is indicated.

1.37 Chemisorption of Oxygen on Cu(111)

(F. Jensen, F. Besenbacher, *Institute of Physics, University of Århus*, R.Feidenhans'l, *Physics Department, Risø National Laboratory, Denmark*, and I.K. Robinson *AT&T Bell Laboratories, Murray Hill, USA*)

Oxygen reacts with Cu(100) and Cu(110) by formation of highly stable Cu-O chains parallel with the (001) directions in the surface. (001) rows are present on the (100) and (110) surfaces, but not on the (111) surface, which makes it more inert to oxygen. We have studied the Cu(111)-O system with X-ray diffraction and Scanning Tunneling Microscopy (STM). The X-ray diffraction measurements were performed at the AT&T beamline X16A at the NSLS at Brookhaven National Laboratory. The Cu surfaces were cleaned by Ar^+ sputtering and exposed to 300 L (1 Langmuir (L) = 10^{-6} Torr-s) oxygen. Depending on the postanneal temperature, 400 °C or 450 °C, two reconstructions appeared. The unit cells were determined by STM and can only be labeled by a matrix notation. The annealing to 400 °C gives a unit cell 29 times larger than a 1 x 1 cell, annealing to 450 °C gives a cell 44 times as large. None of the structures have been correctly identified previously. Both unit cells have *p1* symmetry. Contours plots of the Patterson functions are shown in the figure, which also show the unit cell sizes. The data analysis proceeds along the steps indicatated in the Cu(110)c6 x 2-O study, starting by comparing STM-images and the contour plots of the Patterson functions.

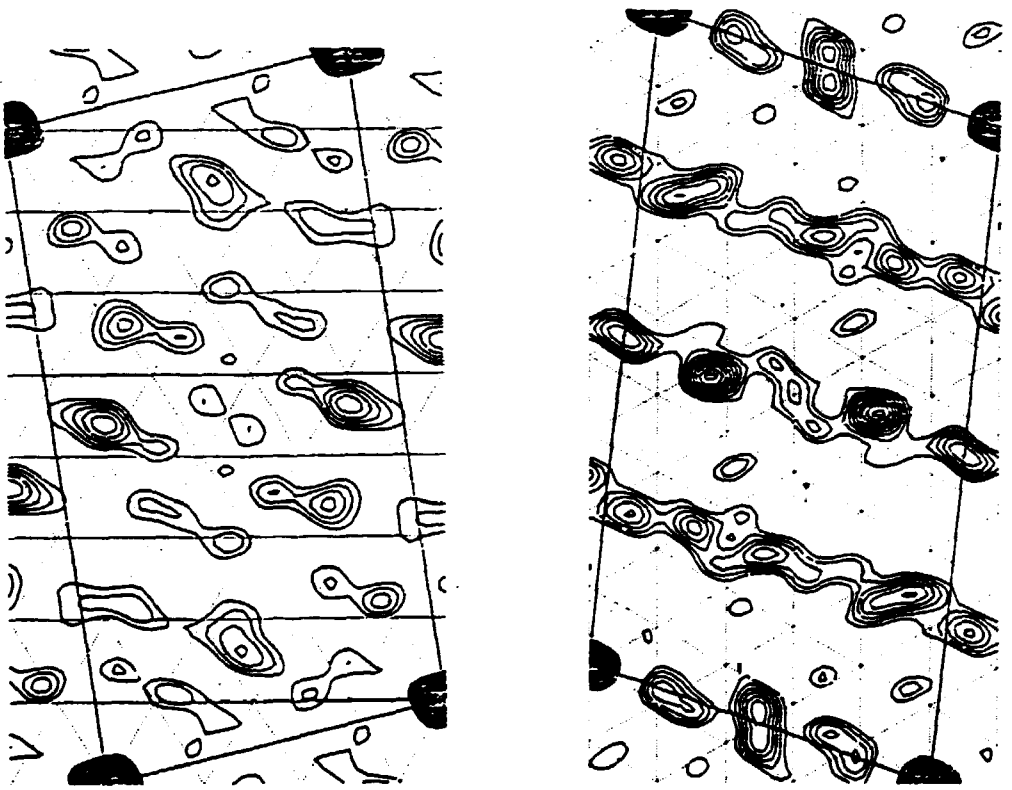

Contours plots of the Patterson function for the structure appearing after the 400 °C anneal (left) and after the 450 °C anneal (right). The unit cell sizes are indicated. Note the different scales.

1.38 The structure of Sulphur on Cu(111)

(R. Feidenhans'l, *Physics Department, Riso National Laboratory, Denmark*, F. Jensen and F. Besenbacher, *Institute of Physics, University of Århus, Denmark* and I.K. Robinson, *AT&T Bell Laboratories, Murray Hill, USA*)

Sulphur is a well known poison for many catalytic reactions. Nevertheless, often the atomic structure of sulphur induced surface reconstructions are not known. Sulphur on Cu(111) is such a case. The structure has a $\sqrt{7} \times \sqrt{7}$R19.1° unit cell. We have performed a crystallographic analysis of this surface. The measuremnts were performed at the AT&T beamline X16A the NSLS, Brookhaven National Laboratory. The structure was prepared by exposing a clean Cu(111) surface to 40 L H_2S (1 Langmuir (L) = 10^{-6} Torr·s) at 100 °C. We obtained a set of 29 non-equivalent structure factor amplitudes. Rod-scans along the fractional-order rods showed that the structure is confined to the topmost layer. The structure has *p3* symmetry. A contour plot of the Patterson function is shown in the figure, indicating four inequivalent interatomic vectors, which must be included in an atomic model.

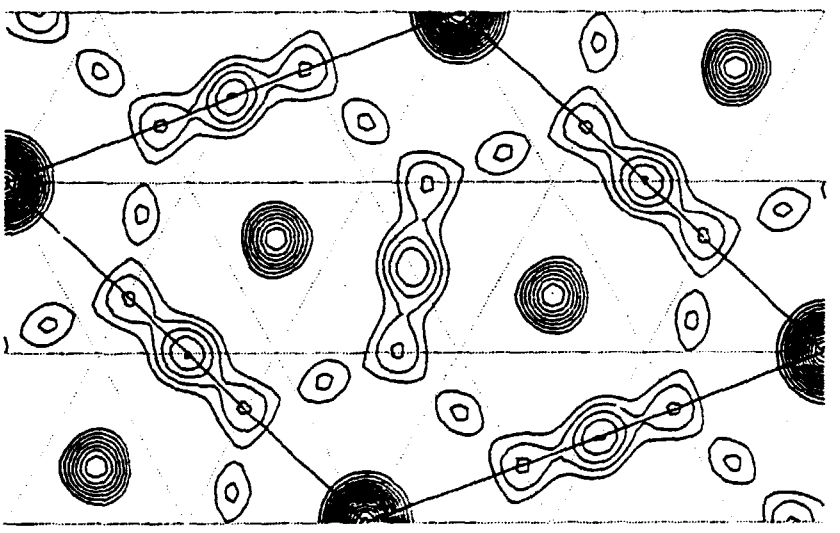

Patterson plot of the Cu(111)$\sqrt{7} \times \sqrt{7}$R19.1°-S structure. The full lines show the unit cell, dotted lines indicate the underlying 1x1 unit cells of the Cu(111) surface.

1.39 X-ray Reflectivity of Free-standing Smectic Films

(P. Lambooy, S. Gierlotka, W.H. de Jeu, *FOM-Institute for Atomic and Molecular Physics, Amsterdam, The Netherlands* and R. Feidenhans'l, *Physics Department, Risø National Laboratory, Denmark*)

In the smectic liquid crystalline phase it is possible to draw free-standing films over a hole in a substrate. In this situation the smectic layers (varying in number from two to very large numbers) are parallel to the surface of the film. Recently these films have been made large enough to allow for X-ray reflectivity measurements[1,2]. In this situation the usual Fresnel fall-off of the reflected signal[3] is modulated by (i) fringes due to the reflections against the two parallel outer interfaces of the film, (ii) the signal from the finite-size limited Bragg peaks and its satellites due to the smectic layering. Due to the interference between these two effects a very sensitive measurements of the electron density perpendicular to the film can be obtained.

The X-ray reflectivity of the free standing smectic films of various materials has been determined using the reflectometer at the beamline D4 of HASYLAB. In this situation the signal to noise ratio was about ten times larger than at a conventional rotating anode source, which allowed the reflected signal to be measured up to much higher wave-vector transfers. In particular, higher orders of the (00l) Bragg reflections could be accurately determined. This provides direct information about the deviations of the smectic layer structure from the sinusoidal density modulation which is usually assumed. This information cannot easily be obtained otherwise, as – in contrast to the present situation – in bulk samples higher-order Bragg reflections are hard to distinguish from multiple (001) reflections.

Some typical reflection curves are shown in the figures. The data indicates that for the compound 4O.8 (the molecyle is shown in Fig. 1) the ratio of the (002) and (001) reflections is in the smectic A phase about one order of magnitude smaller than in the smectic B phase.

[1]S. Gierlotka, P. Lambooy and W.H. de Jeu, (1990). Europhysics.Lett. **12**, 341.
[2]D.J. Tweet, R. Holyst, B.D. Swanson, H. Stragier and L.B. Sorensen, (1990). Phys. Rev. Lett. **65**, 2157
[3]See, for example, J. Als-Nielsen in *Handbook of Synchrotron Radiation*, Vol 3.

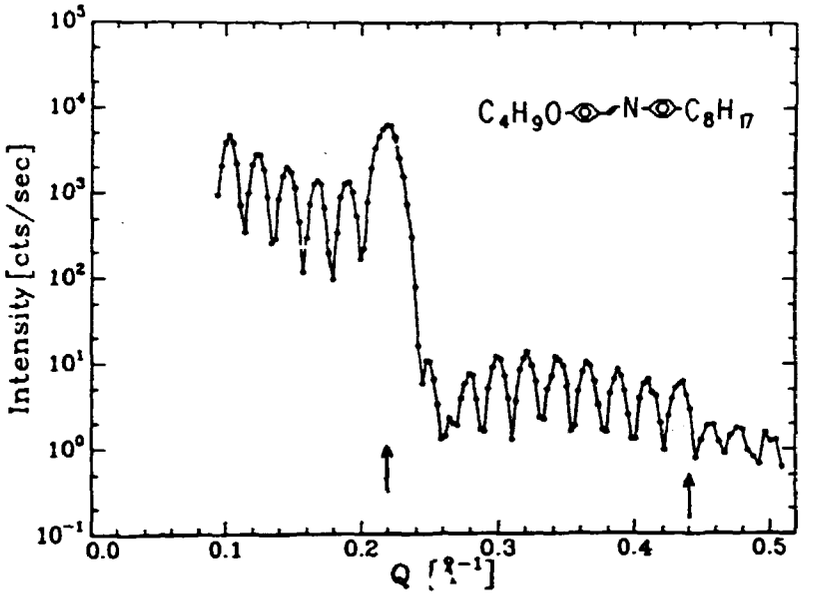

Fig. 1. Reflectivity of a 10 layer 4O.8 film in the smectic B phase at 46 °C. The arrows indicate the (001) and (002) position.

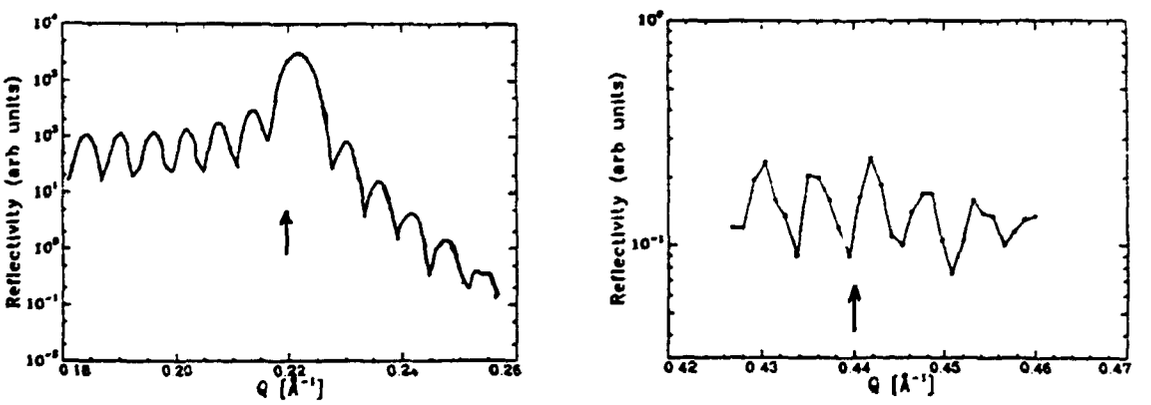

Fig. 2. Reflectivity of a 37 layer 4O.8 film in the smectic A phase at 51 °C (left) around the (001) position and (right) around the (002) position, respectively.

1.40 Structural Properties of DPPC in a Monolayer at the Air/Water Interface: A Neutron Reflectivity Study

(D. Vaknin, K. Kjær, J. Als-Nielsen, *Physics Department, Riso National Laboratory, Denmark* and M. Lösche, *University Mainz, Germany*)

The structure of phosphatidylcholine monolayers in the highly condensed LC (liquid condensed) phase on ultra pure H_2O and D_2O have been studied by the neutron reflection method. The refelctivity measuements were perfomed on a new liquid surface neutron reflectometer situated in the guide hall of the DR3 reactor.

The neutron reflectivity method is by now a widely used technique for the investigation of surfaces and interfaces and has been described in detail by Penfold and Thomas[1]. In contrast to X-ray, neutron reflectivities are rather limited in the momentum transfer range accessible, $q_z \leq 0.3\text{Å}^{-1}$, mainly due to the low incident beam intensity of neutron sources. However, this limitation can be compensated for by the possibility to collect different reflectivity data sets by isotopic substitution on the molecule composing the monolayer. Hence it is possible to concentrate on particular regions of the molecules at the surface.

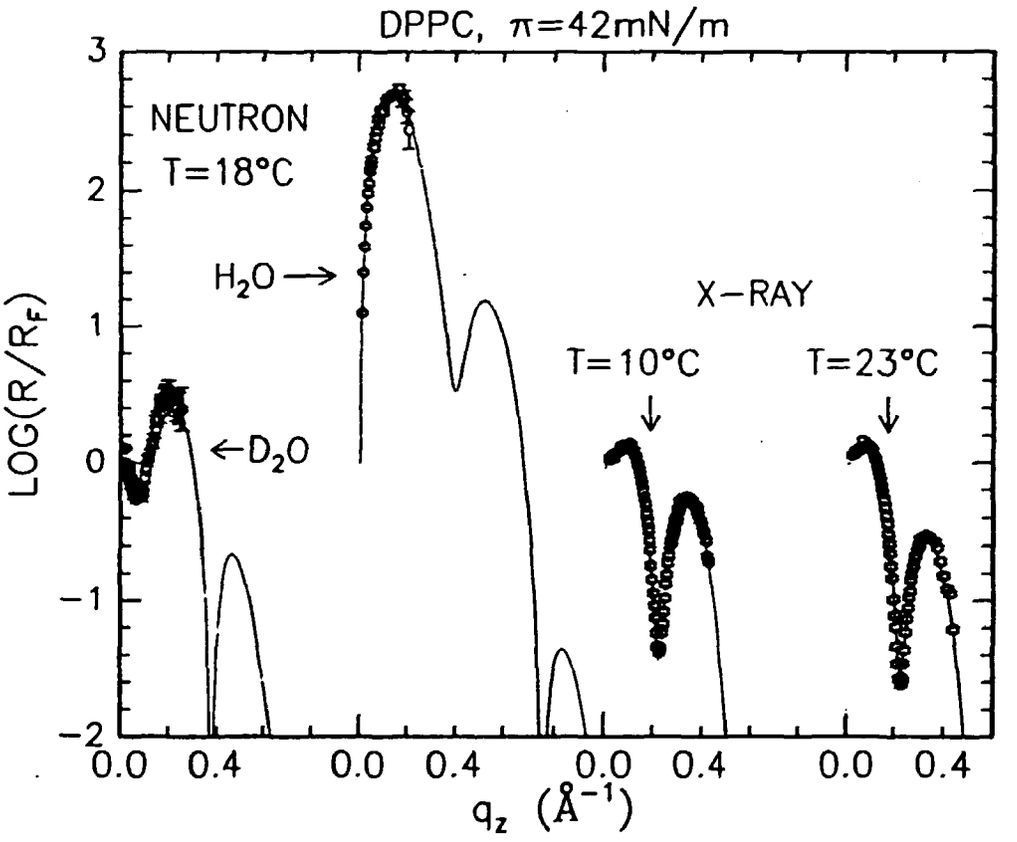

Fig. 1. Experimental reflectivities of DPPC monolayers in the highly condensed phase with calculated reflectivities (solid line) using one model (see text) for the four data sets. The data have been normalized to the calculated reflectivities, R_F, of the pure water surfaces.

Reflectivities from DPPC-d_{62} monolayers on D_2O and H_2O, taken at T = 18 °C and at π = 42 mN/m, are displayed in Fig. 1. Also shown in Fig. 1 are the Fresnel-normalized reflectivities (R/R_F) versus the momentum transfer, Q_z, of X-ray data for a monolayer of DPPC at the same pressure and at temperatures as indicated on the Fig. 1 (the X-ray data were taken from Ref. 2).

In a new approach to analyzing the data, it was demonstrated that both techniques are mutually complementing each other. We have defined a general model based on the assumption that the underlying structure is the same irrespective of technique or isotope substitution and refined a combined data set composed of the four sets depicted in Fig. 1. We have adopted the common two box model to calculate the reflectivities using the Parratt formalism[3]. The scattering length densities used were obtained from standard values of the scattering lengths and the geometric parameters of the model. The unknown parameters in the model are (i) the cross section, A_0, of a lipid molecule normal to the direction of the extended hydrocarbon chain; (ii) the tilt angle β of the chains from the surface normal; (iii) the thickness, d_{head}, of the lipid head group layer; and (iv) the number, N_W, of water molecules interpenetrating the lipid head group. A fifth parameter, the surface roughness, σ, is assigned to each data set to account for the different temperatures and set-ups. The most important conclusion from our analysis is that for this particular monolayer, neither of the two techniques by itself is capable of modeling the interface structure and only the combination of both, X-ray and neutron, leads to a model with reasonable uncertainties for the adjustable parameters. We have in particular worked out the chain packing characteristics and have quantified the head group layer thickness and water interpenetration into the lipid head group. Most of our findings are in quantitative agreement with results from structural investigations of DPPC in aqueous dispersions, and major differences are attributed to the head group arrangements and hydration[4].

[1] J. Penfold and R. K. Thomas, (1990). J. Phys. : Condens. Matter. **2**, 1369.
[2] C. H. Helm, H. Möhwald, K. Kjær and J. Als-Nielsen, (1987). Europhys. Lett. **4**, 697.
[3] L. G. Parratt, (1954). Phys. Rev., **95**, 359.
[4] For details see D. Vaknin, K. Kjær, J. Als-Nielsen and M. Lösche, *submitted.*

1.41 Grazing Incidence X-Ray Diffraction Measurements on Uncompressed Monolayers of Long Chain Alcohols and Carboxylic Acids Relevance to Ice Nucleation

(D. Jacquemain, F. Leveiller, S.P. Weinbach, M. Lahav, L. Leiserowitz, *Structural Chemistry Department, Weizmann Institute of Science, Rehorot, Israel*, K. Kjær, J. Als-Nielsen, *Physics Department, Risø National Laboratory, Denmark*)

Uncompressed monolayers of long chain alcohol $C_nH_{2n+1}OH$ were found to inhibit supercooling of water by inducing nucleation of ice[1] at temperatures approaching 0 °C. (In contrast, water-soluble alcohols are effective anti-freeze agents which lower the *equilibrium* freezing point). The induced (*non-equilibrium*) freezing point was shown to be sensitive to chain length and parity as shown in Fig. 1. The higher freezing point induced by the alcohol had been accounted for in terms of a spontaneous formation of ordered two-dimensional (2D) clusters of alcohol molecules at the surface, with a lattice close in match with the *ab* lattice of hexagonal ice[1]. The corresponding carboxylic acids monolayers $C_nH_{2n+1}COOH$ do not nucleate ice as efficiently as the alcohol films, inducing freezing at temperatures as much as 12 °C lower (Fig. 1). It was suggested that the structural match between the *ab* lattice of hexagonal ice and the acid molecules lattice is not as good as with the alcohol lattice[1].

We thus carried out grazing incidence X-ray diffraction measurements (GID) on uncompressed monolayers $C_nH_{2n+1}X$ (n = 23, 30, 31, X = OH; n = 29, X = COOH) at the air-water interface at 5 °C [2]. The results indicate spontaneous molecular aggregation into large crystalline clusters at ~ zero surface pressure. The diffraction pattern for one alcohol (n = 30) and for the acid are shown in Fig. 2a and 2b respectively. The diffraction groups for the three alcohols were similar except for shifts in peak position. The results point to a centred rectangular cell for which the symmetry-related reflections (1,1) and $(1,\bar{1})$ coincide and the (2,0) reflection is distinct. The unit cell dimensions were computed for the rectangular cell (a', b') and the distorted hexagonal cell ($a = b = \frac{1}{2} \mid \mathbf{a}' \pm \mathbf{b}' \mid, \gamma$) and are given in the table. The cell dimensions of the alcohols are closer than those of carboxylic acids ones to that of ice.

In the self-organized crystalline clusters, the alcohol molecules are tilted by 8 to 11° towards next nearest neighbours, the tilt value being dependent on the chain length. The acid molecules are tilted by 26° towards nearest neighbours. The correlation lengths associated with the first order reflections show that the range of crystalline order is anisotropic, extending only over 35 to 95 spacings parallel to the tilt direction, but over 240 spacings perpendicular to it[2]. The packing arrangements of the alcohol and acid amphiphiles are presently being determined with higher accuracy using the GID data (Fig. 2) and atom-atom potential energy calculations.

[1] M. Gavish, R. Popovitz-Biro, M. Lahav and L. Leiserowitz, Science, *in the press.*
[2] D. Jacquemain, F. Leveiller, S.P. Weinbach, M. Lahav, L. Leiserowitz, K. Kjær J. and Als-Nielsen, *in preparation.*

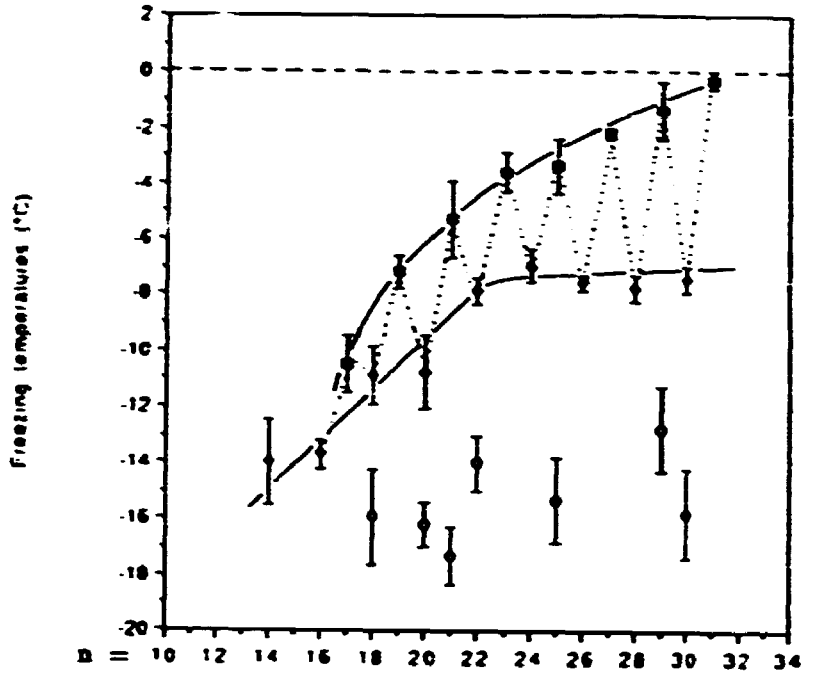

Fig. 1. Freezing points of drops of supercooled water covered by monolayers of alcohols $C_nH_{2n+1}OH$ (n even ◆, n odd □) and carboxylic acids $C_nH_{2n+1}COOH$ (○).

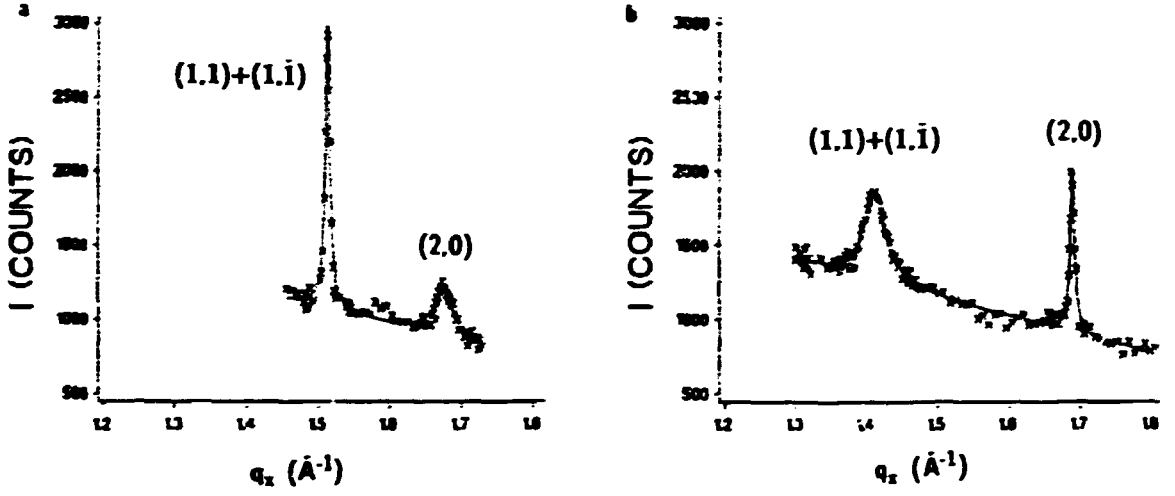

Fig. 2. GID of uncompressed monolayers over pure water at 5 °C ($q_z = 4\pi sin\theta/\lambda$, where 2θ is the angle between the incident and the diffracted beam and λ is the wavelength). (a) Data for the alcohol $C_{30}H_{61}OH$. (b) Data for the acid $C_{29}H_{59}COOH$.

Table: Centred rectangular (a', b'), and distorted hexagonal (a, b, γ) unit cells.

Compound	a'(Å)	b'(Å)	a = b(Å)	γ(°)	area (Å²)
n = 23, X = OH	5.00	7.56	4.54	113.0	18.93
n = 30, X = OH	4.99	7.49	4.50	112.7	18.67
n = 31, X = OH	4.99	7.53	4.52	113.0	18.77
n = 29, X = COOH	5.53	7.44	4.64	106.7	20.58
Hexagonal ice	4.5	7.8	4.5	120	17.5

1.42 Grazing Incidence X-Ray Diffraction of Cadmium Arachidate Monolayers at 9 °C over Water in the Uncompressed State. Evidence in Favour of an Ordered Cadmium Layer

(F. Leveiller, D. Jacquemain, M. Lahav, L. Leiserowitz, *Structural Chemistry Department, Weizmann Institute of Science, Rehovot, Israel*, C. Böhm, R. M. Kenn, *Universität Mainz, Institut für physikalishe Chemie, Germany*, M. Deutsch, *Physics Department, Bar-Ilan University, Ramat-Gan, Israel*, K. Kjær and J. Als-Nielsen, *Physics Department, Risø National Laboratory, Denmark*)

Induced crystallization of organic[1] and inorganic[2] systems under Langmuir monolayers suggests that ions are specifically bound to the monolayer. Thus we carried out Grazing-Incidence X-ray Diffraction experiments at the wiggler beam line W1 in HASYLAB at DESY, Hamburg, on arachidic acid ($CH_3(CH_2)_{18}COOH$) monolayers spread over 10^{-3} M cadmium chloride solutions at a *pH* of 8.8 (adjusted by addition of ammonia), in order to determine whether the cadmium ions are bound in an ordered manner, commensurate or incommensurate, with the arachidate monolayer. Although the monolayer surface coverage was 67 %, with zero surface pressure, an X-ray diffraction pattern (Fig. 1a) was observed at 9 °C displaying no less than 11 diffraction peaks. The width of the peaks around q_x of 1.5 Å^{-1} yield crystalline coherence lengths of $\sim$ 1000 Å. Over pure water under similar conditions, a relatively weak peak at $q_x = 1.44$ Å^{-1} was detected with a coherence length of $\sim$ 500 Å. Thus the cadmium ions promote the self-aggregation of the monolayer.

The X-ray pattern was interpreted as follows: the three intense peaks in the range $1.5\text{Å}^{-1} \leq q_x \leq 1.7$ Å^{-1}, denoted as a "triplet", are due to ordering of the arachidate molecules. Their Bragg rod profiles indicate contribution from the hydrocarbon backbone, whereas the profiles of the remaining reflections are flat, indicating contribution from a thin horizontal layer of atoms, *i.e.*, the Cd^{2+} ions. Assigning $\{h,k\}$ indices $\{0,1\}$, $\{1,\bar{1}\}$ and $\{1,0\}$ to the "triplet" (Fig. 1a), yields an oblique cell $a = 4.60$, $b = 4.89$ Å, $\gamma = 121.3$ °C, with an area of 19.2 Å^2. We may index all the other peaks as fractional orders with indices $\{h/2, k/3\}$ as shown in Fig. 1a, yielding a cadmium unit cell which is a 2×3 reconstruction of the arachidate cell. Since the molar ratio of the counter-ion Cd^{2+} to the carboxylate group CO_2 is 1:2, there must be three Cd^{2+} ions per unit cell. A model using five parameters fits the intensity data set; the parameters varied are a scale factor and two Cd^{2+} ion positions (Table 1) with an assessed Debye-Waller factor. The calculated intensities are shown in Fig. 1b. We shall need to address[3] the question of interleaving ammonia and water molecules in the ionic layer, the structure of the arachidate moiety and the relative displacement of the arachidate and Cd^{2+} lattices.

[1] E.M. Landau, M. Levanon, L. Leiserowitz, M. Lahav and J. Sagiv, (1985). Nature, **318**, 353-356, E.M. Landau, S. Grayer Wolf, M. Levanon, L. Leiserowitz, M. Lahav and J. Sagiv, (1989). J. Am. Chem. Soc. **111**, 1436-1445.

[2] E.M. Landau, R. Popovitz-Biro, M. Levanon, L. Leiserowitz and M. Lahav, (1986). Mol. Cryst. Liq. Cryst., **134**, 323-335, S. Mann, B.R. Heywood, S. Rajam and J.D. Birchall, (1988). Nature, **334**, 692-695.

[3] F. Leveiller, D. Jacquemain, M, Lahav, L. Leiserowitz, M. Deutsch, K. Kjær and J. Als-Nielsen, (1990), *submitted to Science* (1990) and Leveiller, F., *in preparation.*

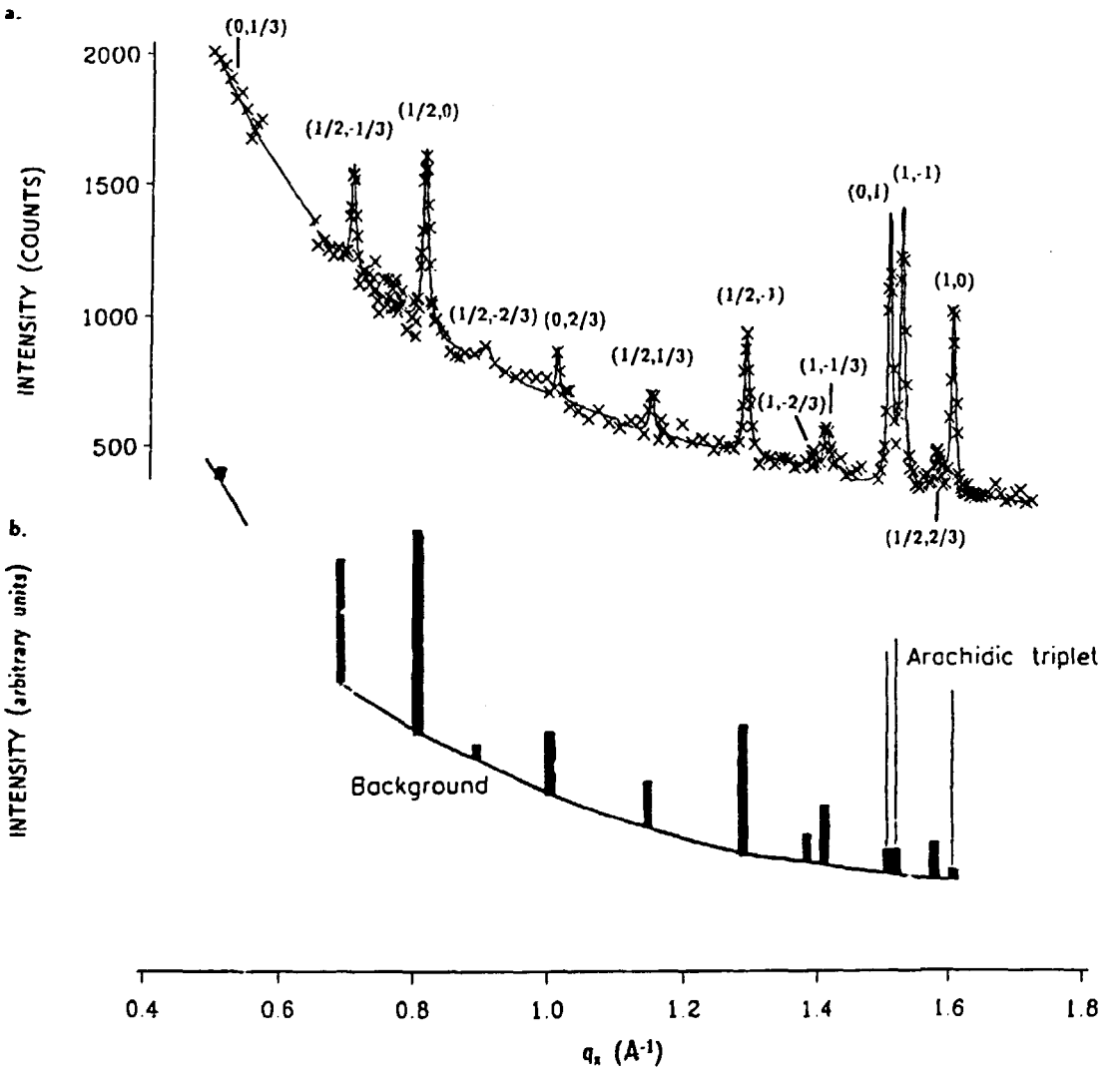

Fig. 1. Uncompressed arachidic acid monolayer spread over a $10^{-3}M$ $CdCl_2$ subphase; pH = 8.8 at 9 °C. The mean molecular area was 28 Å^2 with zero surface pressure (uncompressed state). (a) The observed GID powder pattern. The assigned (h,k) indices are indicated above each peak. (b) The calculated powder diffraction pattern for the cadmium lattice.

Cd^{++}	x	y
1	0^{Δ}	0^{Δ}
2	0.264(23)	0.405(21)
3	-0.059(28)	0.637(25)

Table 1: The fractional coordinates of the Cd^{++} ions in the unit cell a = 9.20 Å, b = 14.68 Å, γ = 121.32°. The estimated errors are given in parantheses. Δ: Fixed coordinates.

1.43 Effect of Solvent on Growth and Dissolution of Ordered Monolayers at Air-Solutions Interfaces

(S. P. Weinbach, D. Jacquemain, F. Leveiller, M. Lahav, L. Leiserowitz, *Structural Chemistry Department, The Weizmann Institute of Science, Rehovot, Israel*, K. Kjær and J. Als-Nielsen, *Physics Department, Risø National Laboratory, Denmark*)

The role played by solvent on the growth and dissolution of three-dimensional (3D) crystals is still not a well understood phenomenon. For example, the central question as to how solvent-crystal surface interactions promote or inhibit growth of a particular face is still, by and large, unanswered. Two-dimensional (2D) crystalline monolayers at the solution interface may be used as model systems for studying solvent-crystal surface interactions because the solvent is in contact with "one" face only. Hence, we first studied the effect of solute molecule glycine NH_3^+-CH_2-CO_2^- in aqueous solution on the growth of 2D crystallites of uncompressed monolayers of the fluorinated amphiphile CF_3-$(CF_2)_9$-C_2H_4-O-CO-CH_2-CH-$(NH_3^+)CO_2^-$ (PFA)[1]. We had found by Grazing Incidence X-ray Diffraction (GID) that glycine in solution significantly retards the growth of crystallites of PFA; it took over 40 minutes for the GID peak to reach maximum intensity[1]. This was interpreted as being due to hydrogen-bonding between solute glycine and NH_3^+-CH-CO_2^- head-groups of neighbouring PFA molecules. The crystallites, once grown, are very stable by virtue of a hydrogen-bonded bilayer involving the PFA headgroup and the underlaying glycine layer. We performed the complementary experiment of monitoring growth and dissolution of PFA over an aqueous solution containing β-alanine (NH_3^+-CH_2-CH_2-CO_2^-). This molecule cannot form a hydrogen-bonded layer underneath the PFA layer and so it retarded the PFA growth to some extent, and subsequently induced complete disruption of the PFA crystallites over a period of two hours (Fig. 1). We also monitored the growth of crystallites of uncompressed monolayers of arachidamide ($CH_3(CH_2)_{18}$-$CONH_2$) over pure water, formic acid (HCOOH) and formamide ($HCONH_2$) water solutions. According to 3D crystal growth experiments of primary amides from formic acid or formamide solutions, it appears as if formic acid inhibits the formation of the crystal face exposing the amide group[2]. The GID results (Fig. 2) are in keeping with this deduction; uncompressed monolayers of arachidamide over pure water solutions form ordered aggregatee with a long correlation length. The same applies to arachidamide over a formamide-water solution, but over a formic acid-water solution the GID peak is so broad that we conclude that the acid solvent inhibits 2D crystal formation.

[1] D. Jacquemain, S. Grayer Wolf, F. Leveiller, M. Deutsch, M. Lahav, L. Leiserowitz, K. Kjær and J. Als-Nielsen, 81990). J. Am. Chem. Soc., **112**, 7729-7736.
[2] S. P. Weinbach, L. J. W. Shimon, M. Lahav and L. Leiserowitz, *work in progress.*

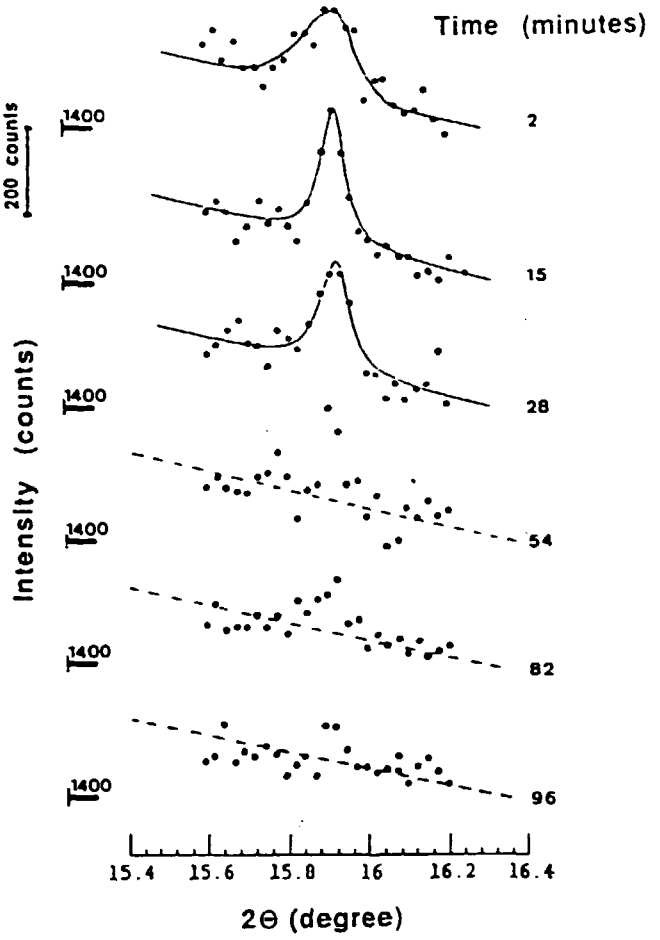

Fig. 1. Time evolution of the grazing incidence X-ray diffraction group of an uncompressed PFA monolayer over an 0.005 M β-alanine solution (2θ is the angle between the incident and the diffracted beam).

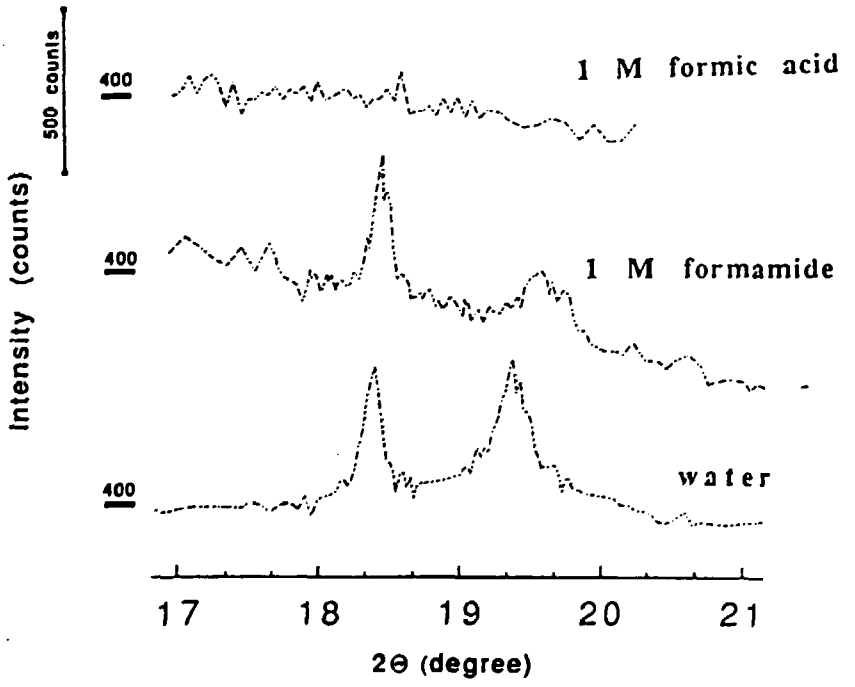

Fig. 2. Grazing Incidence X-Ray Diffraction from uncompressed arachidamide monolayers over various water subphases.

1.44 Crystalline Phases in Fatty Acid Monolayers on Water

(R. M. Kenn, C. Böhm, A. M. Bibo, I. R. Peterson, H. Möhwald, *Mainz University, Germany*, K. Kjær and J. Als-Nielsen, *Physics Department, Risø National Laboratory, Denmark*)

For monolayers of fatty acids, $CH_3(CH_2)_{n-2}COOH$, surface pressure *vs.* molecular area isotherms exhibit anomalies at certain pressures, indicative of phase transitions. Figure 1 shows the phase diagram thus derived for behenic acid, $n = 22$. This phase diagram is similar for all long chain fatty acids with one extra CH_2 group being equivalent to an offset in the temperature scale of 5–10 °C. It is tempting to associate the different phases with different molecular packing configurations which may be revealed by Grazing Incidence Diffraction (GID) using Synchrotron X-rays, and the results derived from behenic acid may indeed be transferred to other fatty acids due to the generic nature of the phase diagram, *c.f.*[1].

Figure 2 shows the geometry of GID from a single crystal grain. The intensity distribution along a Bragg rod, observable for $Q_z > 0$, measures the intersection of the molecular formfactor with the Bragg rod at reciprocal lattice vector $\tau_{h,k}$, so for tilted molecules the intensity may peak at a non-zero value of $Q_z = Q_z^p$. Denoting the polar angle from the surface normal to the molecular axis by t and the azimuthal angle from $\tau_{h,k}$ to the projection of the molecular axis on to the film plane by $\psi_{h,k}$ one finds $\tan t \cos\psi_{h,k} = Q_z^p/\tau_{h,k}$.

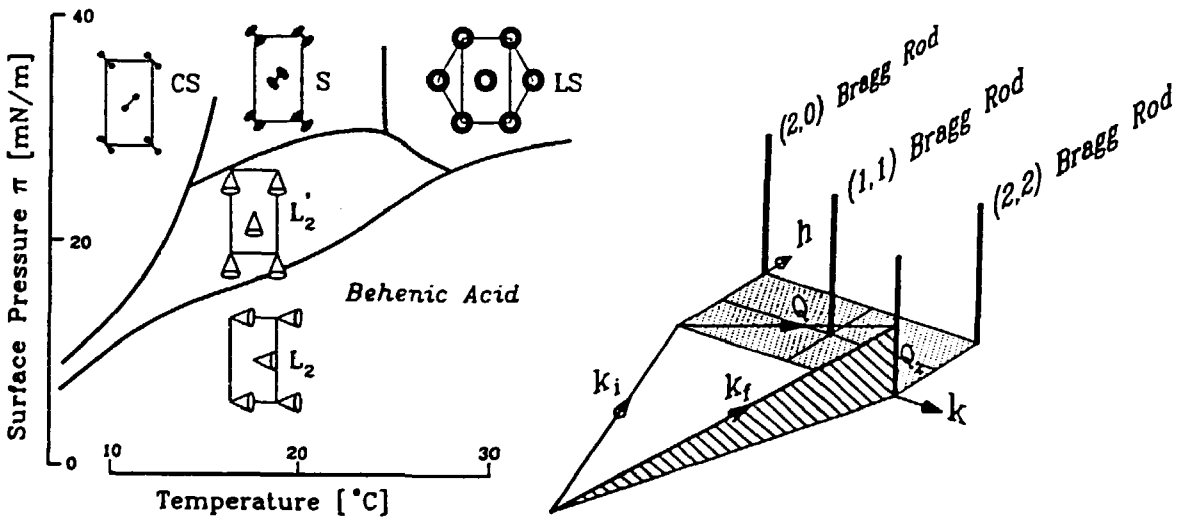

Fig. 1. Phase diagram of behenic acid obtained from isotherms. Inserts: Molecular conformations obtained from intensity distributions along (1,1) and (2,0) Bragg rods, c.f. Fig. 2. Structures: LS: Vertical, freely rotating molecules, area per molecule $A = 20.0$ Å^2. S: Vertical molecules with hindered rotation, $A = 19.3$ Å^2. CS: Vertical molecules, herring-bone structure of the C – C – C backbones, $A = 18.6$ Å^2. L_2: Molecules tilted towards nearest neighbours. L_2': Molecules tilted towards next-nearest neighbours.

Fig. 2. The scattering geometry.

By measuring *two* Bragg rod intensity distributions one can therefore unambiguously derive the magnitude of the molecular tilt as well as its azimuthal direction. Figure 3 shows

such sets of Bragg rods for the (2,0) and the (1,1) reflections in the L_2 phase (top), the L_2' phase (middle) and the S phase (bottom). The corresponding molecular configurations are shown as inserts unit cell in Fig. 1. Data have also been obtained in the CS and the LS phases. In addition to the magnitude and symmetry of the molecular tilt throughout the phase diagram, the X-ray data also provide the size of unit cell and thereby the compressibility as well as the coherence length or crystallinity of the different phases. For details, see Ref. 2.

[1] A.M. Bibo and I.R. Peterson, (1990). Advan. Materials, **2**, 309.

[2] R.M. Kenn, C. Böhm, A.M. Bibo, I.R. Peterson, H. Möhwald, K. Kjær and J. Als-Nielsen, (1990). J. Phys. Chem, *in the press.*

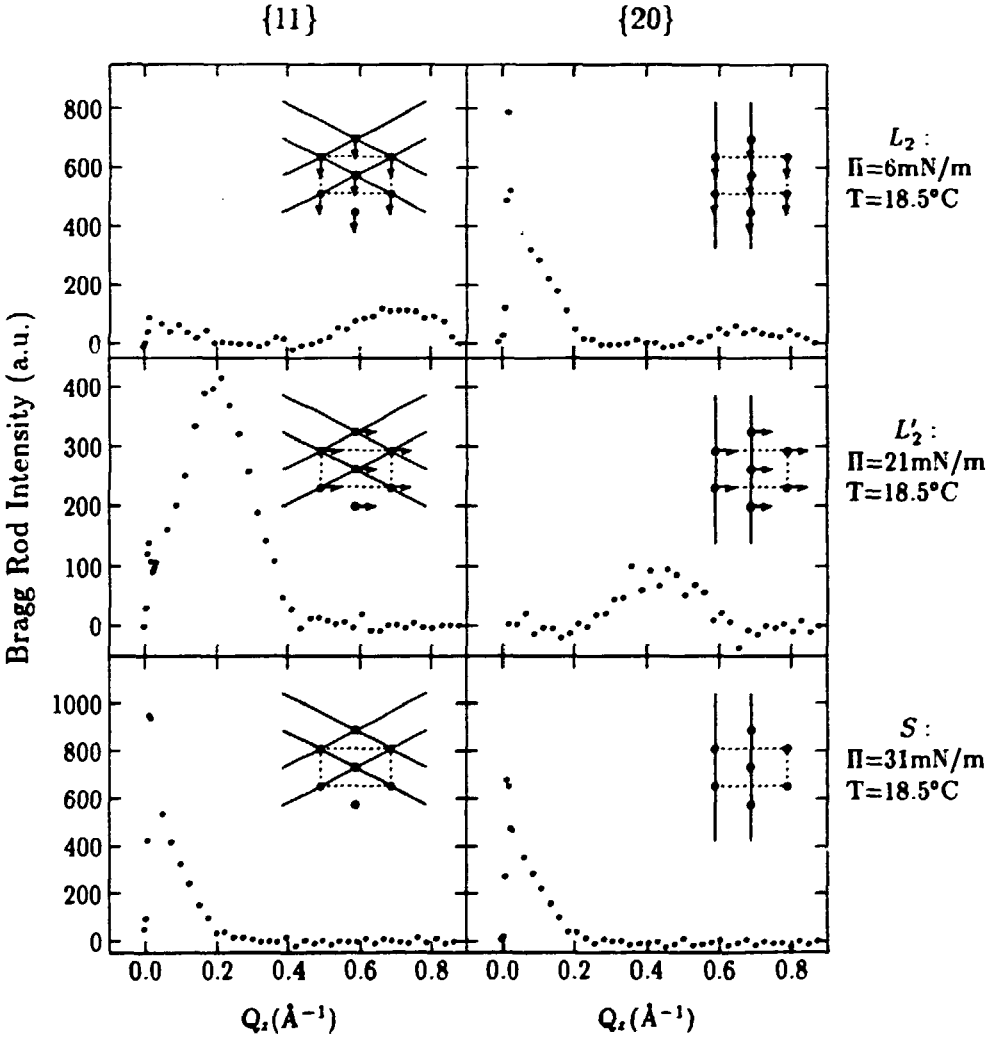

Fig. 3. Intensity distributions along (1,1) (left panels) and (2,0) (right panels) Bragg Rods in the L_2 phase (upper panel), L_2' phase (middle panel) and S phase (lower panel).

1.45 The Prediction of the 3-Dimensional Structure of Protein Backbones by Neural Network and a Novel Folding Routine

(J. Bohr, *Physics Department, Riso National Laboratory, Denmark*, H. Bohr, *University of Illinois, Urbana-Champaign, USA*, S. Brunak and R.M.J. Cotterill, *The Technical University of Denmark*, H. Fredholm and S.B. Petersen, *Novo-Nordisk Research Institute, Copenhagen, Denmark*, and B. Lautrup, *Niels Bohr Institute, Denmark*)

One current aim of molecular biology is the determination of the three-dimensional (3D) tertiary structure of proteins from their sequences of amino acid residues. We deploy a method for predicting the 3D structure of a protein backbone from its amino acids sequences. A neural network was trained on matching sets of amino acid sequences and structural information of two types, one being the corresponding secondary structure and the other the binary distance constraints, in the form of diagonal bands of binary versions of the C_α distance matrices. In the case of a training set consisting of 13 proteases, the network was capable of learning to a level of 99.9 % on the distance matrix output and 100 % on the associated secondary structure assignment. The distance matrix for a protein unknown to the network was generated by the trained network. Subsequently, a novel minimization was used to fold the protein's backbone until a maximally attainable number of the distance constraints were satisfied. The 1TRM trypsin was used as a test case for the combined method, using a neural network and a subsequent minimization, for predicting protein backbone structures. The homologous (75 %) protein 4PTP was included in the training set as well as used as a starting point for the minimization of the backbone structure. However, none of the 223 window configurations with 61 consecutive residues that could be generated from 1TRM, were represented in the training set. The result of the minimization is shown in the figure, and it agrees with the correct 3D structure of 1TRM, to within 3.0 Å root mean square.

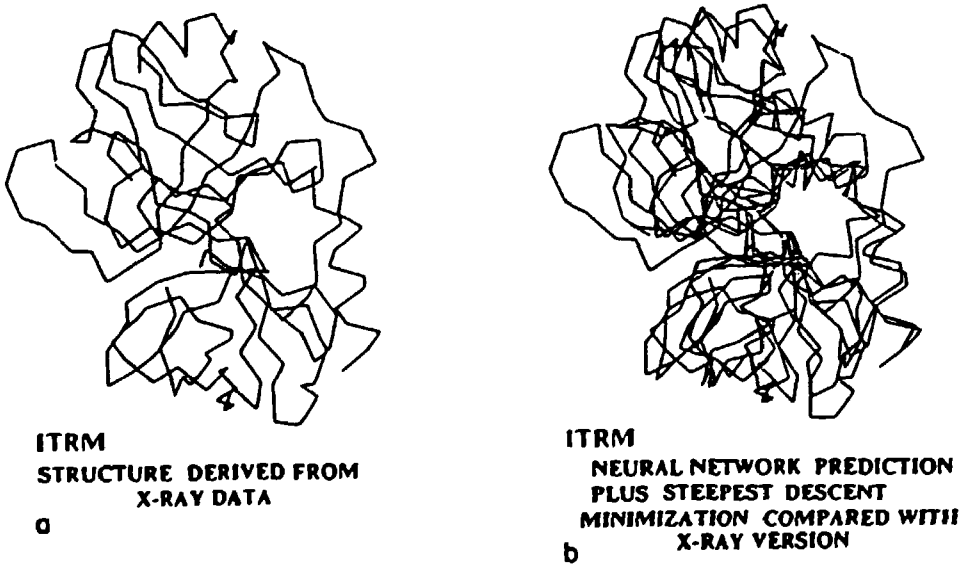

a) The crystal structure for 1TRM, as known from X-ray data. b) The predicted structure of 1TRM superimposed on the crystal structure.

1.46 Small Angle Scattering Studies on Coated Vesicles

(R. Bauer, S. Hansen, *Royal Veterinary and Agricultural University, Denmark*, M. Behan, G. Jones, *Daresbury Laboratory, U.K.*, K. Mortensen, and J. Skov Pedersen, *Physics Department, Riso National Laboratory, Denmark*)

In a living cell, the protein clathrin[1] is polymerised in the form of a polygonic sphere enwrapping a small bilayer membrane vesicle. These coated vesicles serve the purpose of transporting specific macromolecules into the cell. Coated vesicle formation is initiated when ligands bind to their specific receptors on the surface membrane of a cell resulting in clustering of the receptors, invagination of the coated membrane and ultimately the formation of the coated vesicle.

Structural information of clathrin coated vesicles has been achieved by small-angle X-ray[2] and neutron[3] scattering, and dynamic light scattering[4]. A characteristic peak at $q = 0.025$ Å^{-1} in both the X-ray and the neutron scattering profile (in D_2O) from intact coated vesicles is consistent with a polygonic structure of the clathrin coat. From the neutron and the dynamic light scattering data, the size of the coated vesicle is found to be 1000 Å. Dynamic light scattering shows moreover a distribution of sizes for the coated vesicles demonstrating polydispersity of the samples. Quick freezing and slow thawing cause aggregation of the proteins. Simultaneously, the $q = 0.025$ Å^{-1}-peak is markedly reduced, indicating breakdown of the polygonic structure. The figure demonstrates some of these properties, as observed using neutron scattering.

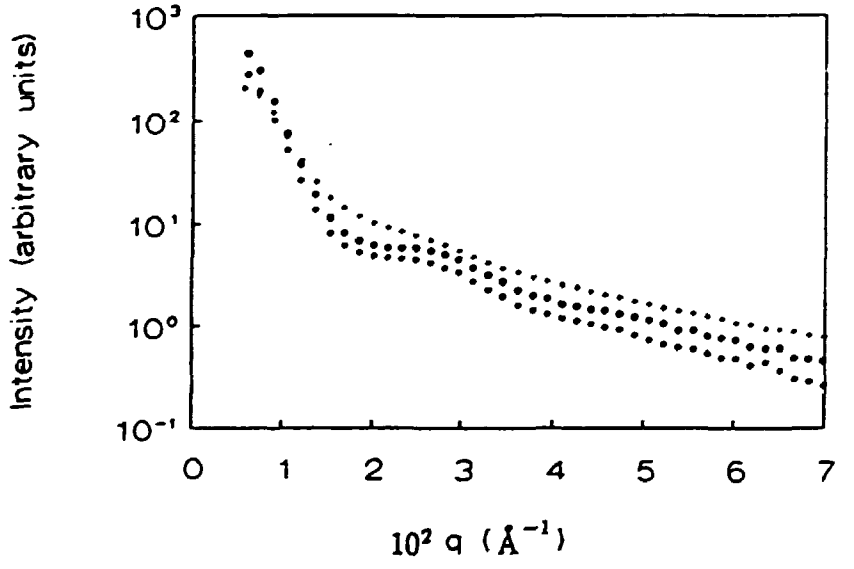

SANS-data on clathrin network: o*: clathrin coated vesicles* o*: clathrin network without membrane* ×*: clathrin coated vesicles previously frozen.*

[1] B.M.F. Pearse, (1975). J. Mol. Biol. **97**, 93-98.
[2] SAXS-Daresbury Synchrotron Facility.
[3] Risø-SANS Facility.
[4] Light Scattering Facility at the Royal Veterinary and Agricultural University.

1.47 Kinetics of Urea-Induced Dissociation of Human Plasma α_2-Macroglobulin

(B. Sjöberg, S. Pap, *University of Göteborg, Sweden*, and K. Mortensen , *Physics Department, Riso National Laboratory, Denmark)*

Human plasma α-macroglobulin (α_2M) is a glycoprotein with molecular weight about 720000. It is generally assumed that the most important physiological role of α_2M is to protect living materia from degradation by the presence of enzymes. The molecule has a complicated structure. It is a tetramer composed of identical subunits linked in pairs by disulfide bonds and two such disulfide bonded dimers are associated non-covalently to form the native tetramer. The strategy in our investigation of α_2M is to dissociate the molecule by specific reagents, followed by characterization of the products by the SANS technique. As a result of these studies we obtain information about the quaternary structure of α_2M, as well as about the nature of the contact area between the subunits. The SANS technique is ideally suited for investigations of this kind, because, besides structural information, it also offers a rapid an non-destructive determination of the average molecular mass of the solute.

In the investigation we have studied the kinetics of the urea-induced dissociation of α_2M into two half-molecular fragments[1]. Measurements have been made both by using deuterated urea ([D]urea) in 99% D_2O, and normal urea ([H]urea) in H_2O. The change in relative mass, which occurs upon dissociation, has been followed by recording the forward scattering of neutrons as a function of time. All the kinetic data, recorded in the [H]urea concentration range from 2.44 to 5.15 M and [D]urea range from 2.70 to 6.24 M, can be explained by a reaction which is strictly first-order with respect to the concentration of un-dissociated α_2M. The velocity constant is a function of the urea concentration and it varies within wide limits. For instance, the half life-time of the reaction (at 21°C) at the lowest concentration of [D]urea studied (2.70 M) is 370 hours, whereas the same value at the highest concentration of [D]urea (6.24 M) is only 8 minutes.

In this system there is also a pronounced kinetic isotope effect. That is, the dissociation is four times faster in H-medium as compared with D-medium, at the same urea concentration. From the angle dependence of the neutron scattering it can be concluded that the reaction is associated with a drastic change in structure; the scattering curve of urea-dissociated α_2M can best be explained by a Gaussian coil with a radius of gyration equal 9.44 nm. We have also studied the temperature dependence upon the velocity constant. To our surprise, we found that the dissociation goes faster at +4°C, as compared to room temperature. This result indicates that entropy factors are involved and that hydrophobic interactions probably are of importance in the non-covalent interaction between the subunits of α_2M.

[1] B. Sjöberg, S. Pap, S.E. Järnberg and K. Mortensen, *submitted.*

1.48 Solution Structure and Interaction of Thiol-Ester Proteins

(R. Österberg, *The Swedish University of Agricultural Science, Uppsala, Sweden*, A. Ikai, *Tokyo Institute of Technology, Japan*, and K. Mortensen, *Physics Department, Risø National Laboratory, Denmark*)

Within the family of native thiol-ester proteins there are monomers, dimers and tetramers with monomeric molecular masses ranging from 185 to 200 kD. One kind of monomeric thiol-ester proteins is that involved initially in the cascade reaction by complement proteins. For instance, activation of the classical or the alternative pathway occurs via a enzymatic cleavage of the proteins: *C*4 or *C*3, respectively. The cleavage yields the small fragments *C*4*a* and *C*3*a*, and the large fragments *C*4*b* and *C*3*b*. As a result, the labile thiol ester bond is split and the *b*-fragments (*C*4*b* or *C*3*b*) may become attached to the target particle, say a bacterium; thereby, the first building stone for the successive formation of membrane attack complex is formed. Using a Kratky-small-angle X-ray (SAXS) camera in Uppsala, and the Risø small-angle neutron scattering (SANS) instrument, we have characterized the complement proteins *C*3, *C*4, *C*5 and some components within the so-called complement cascade[1]. Also, protein-protein complexes, and dimers supposedly involved in the complement reaction have been characterized[2]. More recently, using monoclonal antibodies as markers we have analyzed the conformation change which is induced by the thiol ester cleavage. The results indicate that the conformational change involves rotation of a large globular domain within the *C*3 protein[3].

The facts that organs from pigs are now being used as sources for transplantation on humans, has encouraged us to perform a pa. el study on human and porcine *C*3 and *C*4. The results from these studies show close similarities between the human and the porcine proteins. Also, the porcine proteins cross-react with monoclonal antibodies raised against the corresponding human proteins. Analysis of the solution structures of the antibody complexes indicate that the epitopes on the porcine proteins are situated on a similar surface area as those of the human proteins[4]. Another kind of monomeric thiol-ester protein is the proteinase inhibitor, $\alpha_1 I_3$, present in the blood plasma of rats and mice. It can reach concentrations as high as 15 mg/ml. The SAXS and SANS data shows that $\alpha_1 I_3$ has close similarity in size and shape with those of the *C*3 and *C*4 monomers. The most recent study involves certain tetramers that show atypical reactions relative to methylamine or proteinase. Here, SAXS and SANS are the most powerful methods, since these reactions yield clear changes both in the correlation peak and the radius of gyration. Neutron scattering from solution of ovostatin (a protein obtained from hen and crocodile eggs) in the absence and presence of methylamine yields well resolved data for scattering vector $q \leq 0.25$ Å^{-1}. These data are now being analyzed.

[1] R. Österberg, B. Malmensteen, U. Nilsson, G. Eggertsen, and J. Kjems, (1988). Int. J. Biol. Macromol. **10**, 15-20.
[2] R. Österberg, U. Nilsson, and G. Eggertsen, (1985). J. Biol. Chem. **260**, 12970-12973.
[3] R. Österberg, U. Nilsson, T. Stigbrand and J. Kjems, (1989). Eur. J. Biochem, **183**, 507-511.
[4] R. Österberg, U. Nilsson, T. Stigbrand and K. Mortensen, (1990), *submitted.*

1.49 Studies on Humic Acid Structure and Metal Ion Binding under Various Environmental Conditions

(R. Österberg, I. Lindkvist, *The Swedish University of Agricultural Science, Uppsala, Sweden*, Oluf Wahlberg, *Department Inorganic Chemistry, KTH, Stockholm, Sweden*, and K. Mortensen, *Physics Department, Riso National Laboratory, Denmark*)

Humic acids are highly reactive organic poly-electrolytes that are present in all soils and natural water systems. They react with and bind not only metal ions, but also organic compounds of both low and high molecular weight. They are of great importance for the transport of nutrients and for making them available to the plant kingdom. Nevertheless, as yet, the chemical structures of humic acids are not known, and therefore, studies intended to increase our knowledge of the humic acid structure would be an urgent requirement for a better understanding of the transport of nutrients as well as the transport of toxic metal ions and toxic organic compounds in nature.

We have started a general program to study humic acids under various environmental conditions. These studies include small-angle neutron scattering (SANS) to analyze the size and the shape. Simultaneously, the metal ion binding and acid-base properties are being analyzed using a high-precision electromotive force method. One important factor, which is being studied, is the influence of the *acid rains* on the humic acid structure, as well as on its reactivity and thermodynamic metal ion binding stability. Because it has been reported that humic acids from various sources show great variations in properties, we have studied three different samples. They are all carefully prepared standard samples, two from Europe and one from USA. The SANS measurements involved the full capacity of the new Risø-SANS instrument in order to reach sufficiently large range of scattering vectors, q. The results shows surprisingly good agreement among the three different samples, as far as the radius of gyration R_g for the largest particles are concerned. However, the R_g-values determined are about a factor of ten larger than those previously reported by other investigators.

By measuring the humic-acid in solution of differnt H_2O-D_2O mixtures, one is able to change the contrasts and this yields data which reflect the internal structure of the humus particles in solution. It is the aim, that these studies will result in a model which explains why humic acids bind both hydrophilic (such as metal ions, proteins and carbohydrates) and hydrophobic (such as various pesticides, herbicides, and lipids) compounds.

1.50 Evolution of the Structure of Bicontinous Microemulsion

(S. H. Chen, *LVM/DSM Research, Geleen, the Netherlands*, J. Samseth, *Institut for Energiteknikk, Kjeller, Norway*, and K. Mortensen, *Physics Department, Riso National Laboratory, Denmark*)

In three-component microemulsions composed oil, water and surfactant, the microstructure can continuously vary from a collection of water droplets suspended in oil to a collection of oil droplets suspended in water each coated with a monolayer of surfactant. It is plausible to imagine that in the transition region of inverting form the water internal structure to water external structure, the microemulsions must adopt a bicontinuous structure especially when there are equal volume fraction of oil and water and the surfactant is balanced in its hydrophilic and lipophilic tendencies. We investigate a model microemulsion system consisting of decane/water (0.6% NaCl added)/AOT in its one-phase microemulsion region, as a function of temperature. We used equal volume fraction of decane and water each at 45% and the volume fraction of surfactant AOT kept a constant value of 10%. As the temperature varies from the lower phase boundary at $T_1 = 35$ °C to the upper boundary at $T_u = 55$ °C the microemulsion is known to evolve from the water internal structure continuously to the water external structure[1]. The phase diagram of the system in the $T - \gamma$ plane, where γ denotes the surfactant weight fraction, is shown in the first figure. We are particularly interested in searching for the *inversion – temperature* within the one-phase channel. We have performed SANS experiments using the bulk contrast between oil and water and an interface contrast between surfactant and oil in water. We have, by a careful examination of the set of data for the temperature variation at constant composition, located the inversion temperature to be at 40 °C[2]. At this temperature the surfactant can be said to be completely balanced and the structure should be truely bi-continuous. The second figure shows an example of SANS scattering data, as obtained for sample with interface contrast.

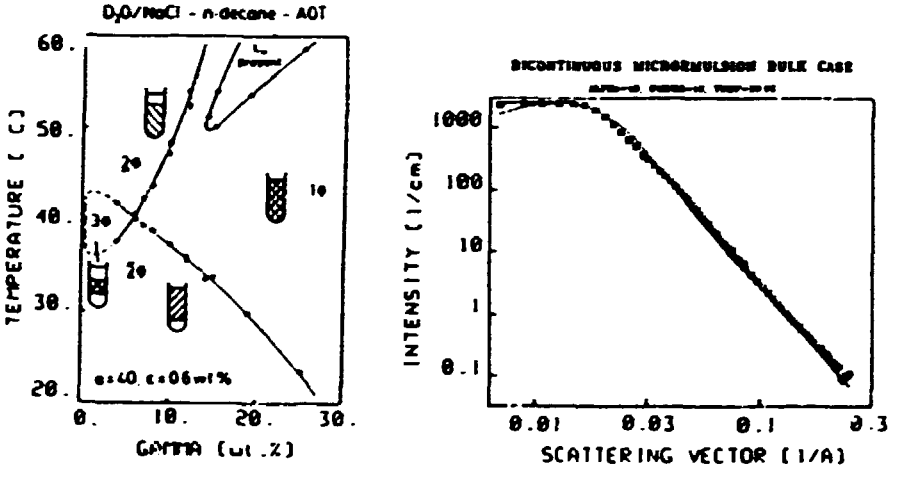

a) Phase diagram of AOT/D_2O/H-decane microemulsions at α = 100 wt.% oil/wt.% oil+ wt.% water = 0.40. b) SANS data of the system obtained at the 1ϕ-3ϕ (1-phase to 3-phase) transition. The full line represents fitting to a model [2].

[1] S.H. Chen, S.L. Chang, and R. Strey, (1990). J. Chem. Phys. **93**, 1907.
[2] S.H. Chen, S.L. Chang, R. Strey, J. Samseth, K. Mortensen, *in the press.*

1.51 Effect of Alcohols on the Properties of Micellar Systems

(G. Forland, *Kjemisk Institut, Bergen University, Norway*, J. Samseth, *Institut for Energiteknikk, Kjeller, Norway*, and K. Mortensen, *Physics Department, Riso National Laboratory, Denmark*)

Alcohol solubilization effects on aqueous solutions of sodiumdodecyl-sulfate (SDS) micellar system has been investigated by means of quasielastic light scattering, viscosity measurements, and small-angle neutron scattering experiments.

Aquaous solutions of 0.4 molar SDS was used. For the neutron scattering experiments D_2O was used instead of normal H_2O in order to obtain good contrast. The investigations includes the different alcohols: 1-butanol, 1-pentanol and 1-hexanol. The effect of different concentrations of these alcohols was studied. Moreover the effect of the ionic strength was investigated by changing the NaCl concentration (maximum 0.4 molar).

Light scattering, neutron scattering and viscosity measurements on the pristine material show all spherical micelles. Upon the addition of butanol, which is a short chain alcohol, neither the size nor the shape of the micelles changes. It is therefore probably that butanol remains in the water rather than interpenetrating the SDS micellses. Upon addition of pentanol, however, the micellar radius increased, reaching a maximum value at about 0.15 molar pentanol. Hexanol, on the other hand, seems to change both the size and the shape of the micelles. The light scattering measurements were originally interpreted as indicating highly hexanol-swollen micelles. However, light scattering data are difficult to interpret and the data may rather indicate changes in shape and micellar interactions. New neutron scattering data indicates that changes in the shape are more important for the hexanol/SDS micellar system.

1.52 Small-Angle Scattering of Poly(Vinylchloride)

(R.L. Scherrenberg, H.R. Reynaers, *Katholieke Universiteit, Leuven, Belgium*, K. Mortensen, *Physics Department, Risø National Laboratory*, W.A.H.M. Vlak, *Netherlands Energy Research Foundataion, ECN, Petten, The Netherlands*, and C. Gondard *LVM/DSM Research, Geleen, The Netherlands*)

The influence of the polymerization temperature on the internal morphology of poly(vinylchloride) (PVC) powders has been examined with both small-angle X-ray and small-angle neutron scattering. Neutron scattering experiments were carried out at both the Petten-SANS facility and at the Risø-SANS facility. The neutron scattering experiments were proven to be favorable relative to the X-ray scattering, partly because of the high absorption of X-rays by poly(vinylchloride) and partly because of the better resolution possible using long wavelength neutrons. The experiment showed that the PVC powders contain pores of about 1 μm. No indication were found for the presence of the proposed micro-porosity, with length scales much below 1 μm. The specific surface of the powders proved to be very dependent on the polymerization temperature, however. All powders studied showed a non-ideal Porod relation-ship. In stead of the *intensity* $\sim (Q)^{\alpha}$, where Q is the scattering vector and with α=4 for a sharp interface, an exponent of α=4.5 was found, indicating a rather smooth surface of the powder. The figure shows the SANS data as obtained for PVC sample polymerized at different temperatures. Plasticized samples of PVC exhibit a prominent peak in the small-angle scattering experiment. This peak has been interpreted using a two-phase model where the two phases are assumed to be respectively amorphous plasticized material and unplasticized crystalline PVC[1,2]. The position of the correlation peak therefore gives information on the penetration of solvent in PVC. Preliminary small-angle neutron scattering experiments were carried out on three PVC samples for different plasticizer concentrations. The experiments shows that the correlation peak, and thereby the internal structure of plasticized/non-plasticized material is dependent on both the solvent and the polymerization temperature.

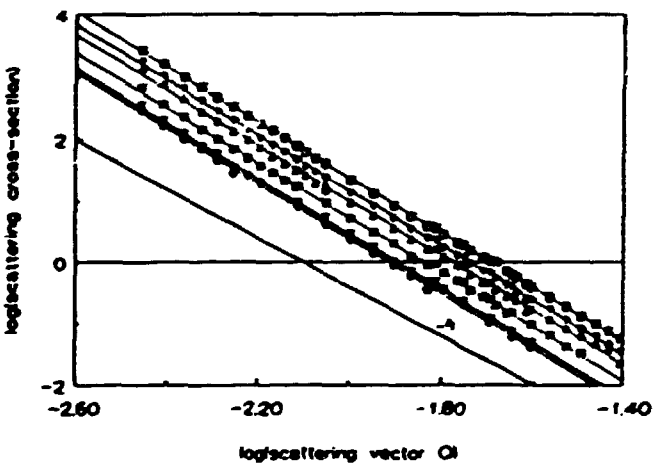

SANS data on PVC samples as polymerized at different temperatures: o: *86 °C* ◁: *81 °C* □: *74 °C* △: *64 °C* ◇: *44 °C* +: *36 °C* ▯: *26 °C.*

1.53 Ordered Phases in Block-Co-Polymer Melts

(K. Almdal, F. Bates, K. Koppi, *University of Minnesota, Minneapolis, USA*, and K. Mortensen, *Physics Department, Risø National Laboratory, Denmark*)

The balance between entropic and energetic factors, and the corresponding phase behaviour, is particularly delicate in *soft* materials, such as microemulsions, micellar solutions, and block copolymers. Lacking short range order, these mesomorphic substances can fill space through the formation of intriguing microstructures, including bicontinuous phases characterized by periodic area minimizing surfaces. Block copolymers are particularly suitable for the investigation of such phase behaviour since the molecular parameters which govern the overall entropy and energy can be independently and precisely controlled. By the application of a shear field, long range order can be obtained, resulting in well defined three-dimensionally resolved Bragg reflections. By neutron small-angle scattering and shear modulus measurements, we are mapping the phase diagram of a model diblock copolymer, consisting of poly(ethylene-propylene) PEP and poly(ethyethylene) PEE[1]. For example, we have shown that the $PEP_{0.65}$-$PEE_{0.35}$ changes between three ordered phases: a low temperature discontinuous lamellar structure, a mono-continuous and a bi-continuous ordered phase at intermediate temperatures, and a disordered bi-continuous phase at high temperature[2]. In other regions of the phase diagram, hexagonal structures develops, as shown in the figure.

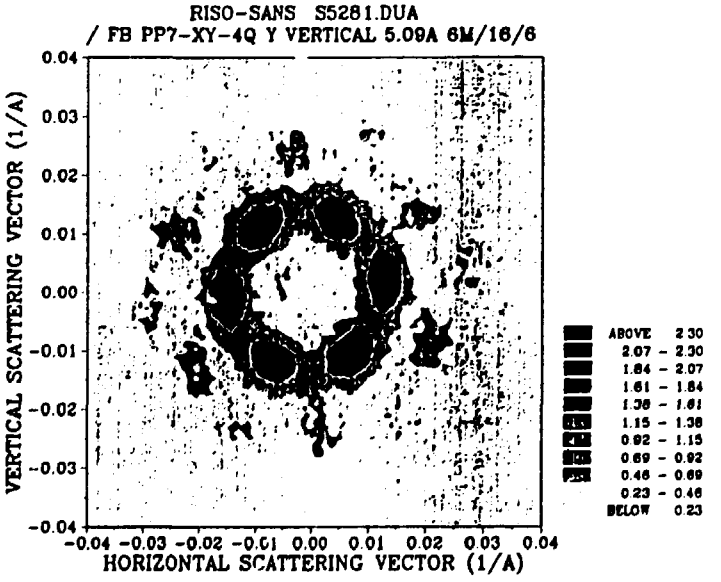

SANS-data on PEP-PEE, showing hexagonal structure.

[1] F.S. Bates, J.H. Rosedale and G.H. Fredrickson, (1990). J. Chem. Phys. **92**, 6255-6270.
[2] K. Almdal, K. Koppi, F.S. Bates and K. Mortensen, *submitted.*

1.54 Structural Studies of the Aggregation of Co-Block-Copolymers in Aqueous Solution

(K. Mortensen, J. Skov Pedersen, *Physics Department, Risø National Laboratory, Denmark*, W. Brown, *University of Uppsala, Sweden*, and S. Hvidt, *Roskilde University Center, Denmark*)

Aqueous solutions of the low-molecular weight tri-block copolymer consisting of poly(oxypropylene) POP and poly(oxyethylene) POE exhibit interesting, unusual characteristics. While the solution of POP-POE-POP copolymer at low temperature forms a low viscous liquid, the high temperature properties reveal that of of a solid-like gel[1,2].

The structural properties of the copolymer $OP_{40}OE_{25}OP_{40}$ has been studied by small-angle neutron scattering. Samples with different concentration ranging from 1% to 30% polymer has been studied as a function of temperature. The scattering data clearly reveal the correlated structure resulting in the gel-phase at high temperature. However, while viscosity measurements shows a transition to the gel state to occur within less than one degree[1], the neutron scattering data shows a gradually developing correlated structure, as given by the intensity of the correlation peak observed. In the figure is shown the development of the scattering function for the 20% POP-POE-POP sample. At low temperatures, both the intensity and the q-dependence of the neutron scattering is rather weak. This is in contrast to dynamic light scattering experiments, which indicates both well defined POP-POE-POP *monomers* and *micelles* at low temperatures[1]. At high temperature (not shown in the figure), the correlation peak vanish, and low-angle scattering dominates the structure-factor in agreement with the cloud-point observed by static light scattering.

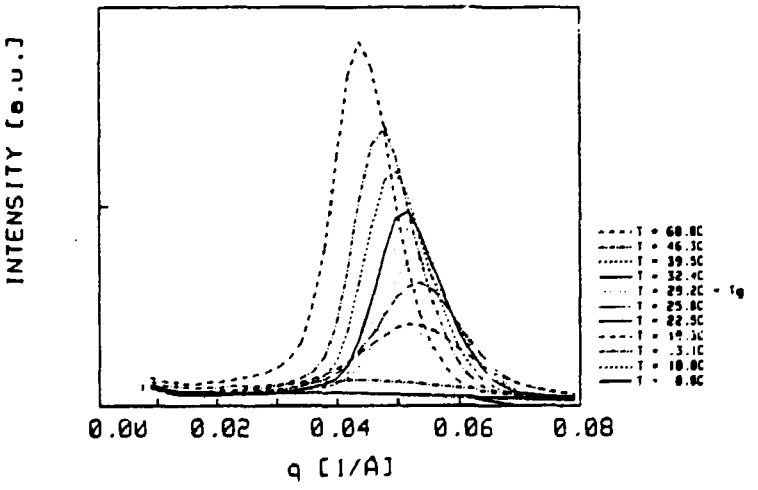

SANS data on aqueous solution of 23% $OP_{40}OE_{25}OP_{40}$ as obtained at temperatures ranging from 8 to 61 °C. Above approximately 13 °C, a well defined correlation peak develops. There seems not to be any marked change in the correlation peak at the gel-transition temperature, $T_g = 30$ °C, as observed by viscosity measurements.

[1] H.R. Brown, H. Kasakevich, and G.D. Wignall, (1986). Polymer **27**, 1345.
[2] D.G.H. Ballard, A.N. Burgess, J.M. Dekoninck, and E.A. Roberts, (1987). Polymer **28**, 3.

1.55 Small Angle Neutron Scattering Study of PDMS Gels Cross-linked by Electron Irradiation and Swollen to Equilibrium

(A.N. Falcão, J. Skov Pedersen, and K. Mortensen , *Physics Department, Riso National Laboratory, Denmark)*

A polymer melt, randomly crosslinked, will reach the gel point at a certain crosslink density. A macroscopic cluster of connected polymers will then be formed extending the whole sample, and the elastical properties of the polymer will change from liquid-like behaviour to solid-like behaviour. Although gelation processes and polymer networks have been, for many years, an active area of research, there are several questions lacking a proper answer. Seeking a better understanding of the microscopic properties of randomly crosslinked polymer gels, we address, in particular, the question of how a network accomodates changes in volume on a local scale.

Recently[1-2], it has been reported that the swelling process of randomly crosslinked gels disagrees with the classical picture of a regular network whose elementary strands expand upon swelling. This conclusion was drawn from the results of scattering experiments performed on swollen networks prepared by random crosslinking of the polymers in their *reaction bath.* A comparison between the signal produced by these swollen gels with the one produced by dissolved samples that have the same polymer concentration, showed that, for large scattering vector q (small length scales), both signals match almost perfectly (no evidence of any deformation was observed). On the other hand, in the small q region the signals are very different – a strong increase in the scattering intensity of the gel is observed, indicating important fluctuations of polymer concentration at large scales. To explain the very heterogeneous swelling of the gel, a model based on percolation theory was proposed. It introduces the notion of "frozen blob" – a blob that is trapped by crosslinks produced in first neighbour contact points on the model lattice. The frozen blobs can form clusters whose mass distribution depends on the crosslink density. Even in the presence of a good solvent, the frozen blobs are not expected to swell, the solvent being absorbed in the medium in between the clusters. This model predics two correlation lengths : ξ_b – associated with the typical size of the blob ; ξ_c - associated with the typical size of the clusters of frozen blobs. The small angle scattering curve of such a system will then show three different regions: $q \gg 1/\xi_b$ where the inner structure of the blobs is probed, $\xi_c \ll q \ll 1/\xi_b$ where the inner structure of the clusters is probed, and $q \ll 1/\xi_c$ where the gel looks homogeneous.

We have started studying the structural characterization of polidymethylsiloxane (PDMS) networks produced by electron irradiation. However, instead of performing the crosslinking in the reaction bath, we crosslinked the *polymer melt.* In order to determine the gel fraction dependance on the received dose, samples were irradiated at different doses (ranging from 30 kGy to 1 MGy). After irradiation the non-crosslinked fraction was extracted in a bath of *p*-xylene under N_2 atmosphere and a temperature of 60 °C for several days. The gel fraction was measured by the ratio between the masses after and before extraction. The equilibrium swelling dependence on the dose received was measured by the volume change produced by immersing the crosslinked networks in excess of *p*-xylene. The small angle scattered intensity was recorded for five samples (irradiated at doses 100 kGy, 125 kGy, 150 kGy, 400 kGy and 800 kGy), after being swollen to equilibrium

in fully deuterated *p*-xylene. Also polymer solutions with the same volume fractions were measured.

Although the analysis of the experimental data is at its beginning, some qualitative behaviour can already be given: i) The samples show the characteristic increase in scattered intensity at very low q. The highest intensity at very small q was found in the 125 kGy sample. The increase in intensity is gradually less pronounced for increasing dose; ii) Fig.1 shows a log-log plot of the absolute intensities for the sample crosslinked at 100 kGy and for the solution having the same polymer volume fraction. At very small q the signal falls off following a power law. Then it has an apparent small plateau before falling off again following another power law. This kink was observed for the samples crosslinked at 100, 125 and 150 kGy, although the width of the apparent plateau decreases with increasing crosslinking degree. At 400 kGy it is hardly possible to identify it and at 800 kGy it is definitly not observed; iii) The ξ_c crossover is not observed in the samples crosslinked at 100 and 125 kGy, presumably because they are shifted to values of q so small that it was not accessed in the experiment. However samples irradiated at 150 and 400 kGy show a tendency for the intensity to level off at very small q, and that effect is clear for the higher dose sample (800 kGy); iv) ξ_b is clearly present for all samples except for the 800 kGy one, where an extended cross-over region is present; v) Although i)-iv) are in qualitative agreement with the model proposed, the power law dependence of intensity does not agree with the values predicted by the theory. In the intermediate regime they are systematically lower than the predicted ones, and they depend on the crosslinking degree. From 100 kGy to 125 kGy it increases, and for higher doses it decreases. At 800 kGy the power law is completely shadowed by the crossover. In the high q regime, the slopes are not constant, but decrease with the dose.

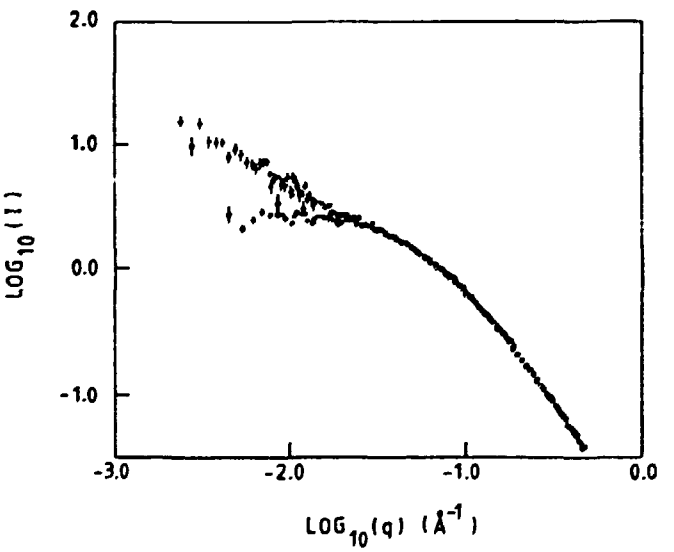

Fig. 1. Log-log plot of the absolute intensities for the sample crosslinked at 100 kGy, and for the solution having the same volume fraction.

[1] J. Bastide and L. Leibler, (1988). Macromolecules **21**, 2647.
[2] J. Bastide, L. Leibler and J. Prost, (1990). Macromolecules **23**, 1821.

1.56 Structural and Thermal Studies of Silica Aerogel

(D. Posselt, J. Kjems, J. Skov Pedersen, K. Mortensen, *Physics Department, Riso National Laboratory, Denmark*, A. Bernasconi, T. Sleator and H. R. Ott, *Laboratorium für Festkörperphysik, ETH-Hönggerberg, Switzerland*)

The concept of self-similarity is an 'alternative' symmetry concept giving a key to systematic descriptions of certain amorphous materials. A three year ph.d. project has focused on materials for which self-similarity is established through mass-fractal scaling: mass $\propto$ (distance)^{d_f}, where d_f is the fractal dimension. Dried silica gels have become prototype model systems, showing mass-fractal scaling over up to two decades in lengthscale (10-1000 Å), depending on the detailed preparation conditions.

Silica gels are made in the liquid state, *i.e.* as wet gels. After gelling the gels must be dried without destroying the gel network, which can be done by hypercritical drying or alternatively by freeze drying. The last method however, produces powders of mm-sized grains. Small-angle scattering with X-rays (SAXS) and neutrons (SANS) have been used to investigate changes in the dry gel structure, when reaction parameters such as pH and aging time of the wet gel are varied . The gel structure is characterized by four parameters: The fractal dimension d_f, the size of the building blocks R, the maximum length scale at which mass-fractal scaling applies, *i.e.* the correlation length ξ, and a surface fractal dimension characterizing the degree of roughness of the inner surface of the dried gel. These parameters are found for different types of gels by model fitting in reciprocal space, and the systematics found is explained in terms of reaction chemistry.

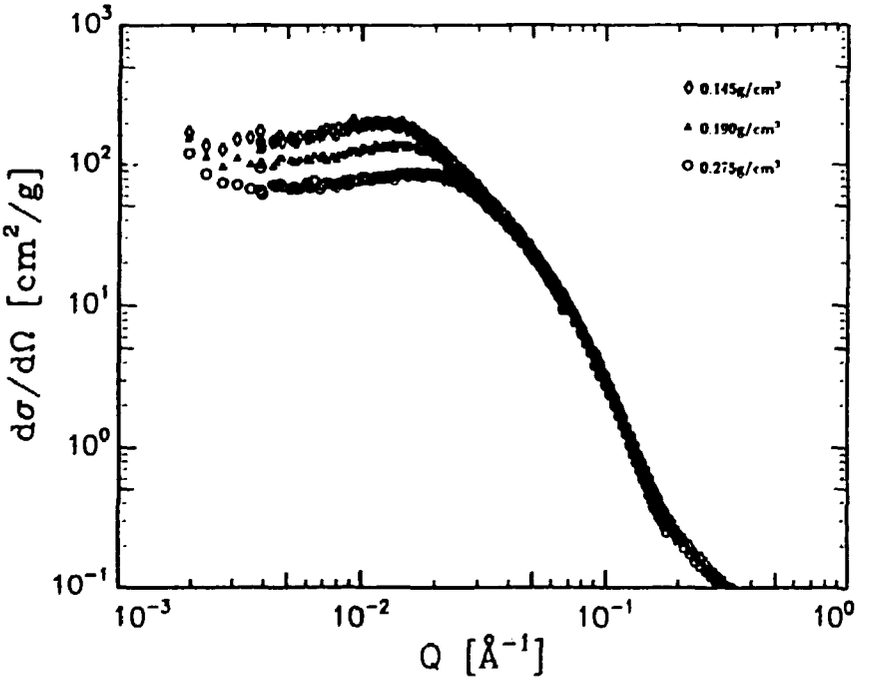

Fig. 1. SANS spectra of a homologous series of base-catalyzed silica aerogels.

A homologous series of three base-catalyzed aerogels with densities 0.145 g/cm^3 (LD), 0.190 g/cm^3 (MD) and 0.275 g/cm^3 (HD) have been characterized by SANS (Fig. 1), sound velocity measurements and Brillouin light scattering. The data are found to be consistent with a model where the gel is made by aggregation of amorphous silica units with a radial size of 20 Å. The fractal dimension $d_f \sim 2$, and the correlation length ξ is found to increase systematically with decreasing density, the values lying between 200 and 350 Å. The longitudinal sound velocity is varying between 182 m/s (LD) and 423 m/s (HD).

A basic question is, whether a fractal structure is reflected in the vibrational behaviour of the system in question - theories predicting localized 'fracton' modes to be the dominant excitations in the frequency regime corresponding to fractal structure. A rough estimate of the relevant frequencies for the aerogel series, using the measured sound velocity and correlation length, gives a cross-over from long wavelength phonon behaviour to the fracton regime at $\omega_\xi \sim 0.1$ K, which is consistent with estimates based on Brillouin light scattering.

The low temperature specific heat C_p and thermal conductivity λ of the above described gel series have been measured at Laboratorium für Festkörperphysik, ETH, Zürich. Due to long relaxation times, a technique specifically designed for aerogels has been developed. The technique is based on a classical thermal relaxation method, and gives both C_p and λ in the same run. The data cover the temperature interval 0.05-20 K. Specific heat data for aerogel of density 0.145 g/cm^3 (LD) and 0.275 g/cm^3 (HD) are shown on Fig. 2, and thermal conductivity data for the same samples in Fig. 3. For comparison also data for amorphous silica is shown[1]. The data confirm the existence of three different vibrational regimes, where crossovers in frequency correspond to the structural crossovers. The crossovers in frequency are observed at temperatures which roughly corresponds to $\hbar\omega/k_B \sim T$. Below T_ξ phonons are dominating and above T_R internal modes of the basic particles become excited. In-between these two crossover temperatures the fracton regime is found. We fit a model density of states, $N(\omega) \propto \omega^2$ for $\omega < \omega_\xi$, and $N(\omega) \propto \omega^{\tilde{d}-1}$ for $\omega > \omega_\xi$, to the specific heat, and find a 'bump' in the density of states around the crossover frequency ω_ξ between phonon and fracton behaviour. From the fit we find $\omega_\xi \sim 0.10$ K and the spectral dimension $\tilde{d} \sim 1.1$ for the LD sample and $\omega_\xi \sim 0.37$ K and $\tilde{d} \sim 1.2$ for the HD sample. Our data for the MD sample do not reach below 1 K, which is why they are not included in the full analysis. In the particle regime however, the MD data are analysed consistently within the same model as the other samples.

Individual contributions to the thermal conductivity from phonons, fractons and particle modes respectively are determined. We find a linear temperature dependence in the fracton regime as predicted theoretically (fracton hopping model). Further we observe that λ is proportional to C_p in the regime where the thermal properties are dominated by particle modes. This is interpreted as a consequence of the mean free path of the particle modes being limited to the size of the building blocks. The proportionality constant characterizes the network connectivity which increases with the sample density in analogy with a percolation network. Our data cannot be explained in terms of two-level states, and further we conclude from comparing with amorphous quartz data, that application

of the fractal concept to dense glasses, where mass-fractal scaling does not apply, certainly can be questioned.

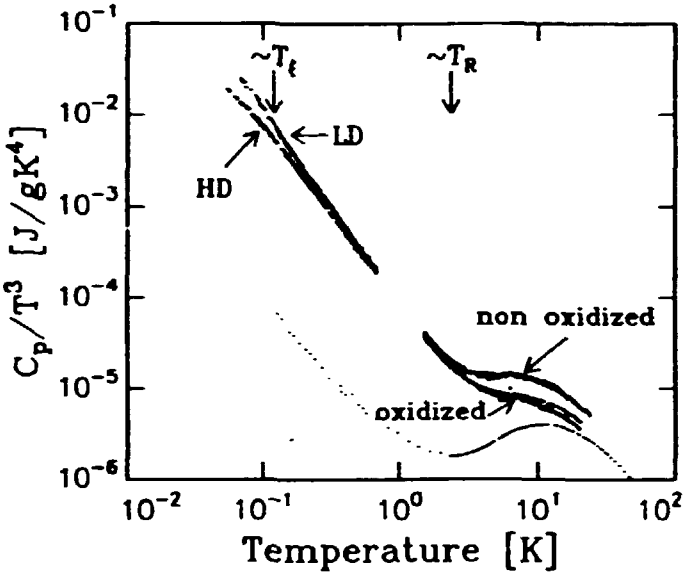

Fig. 2. Specific heat data for the homologous aerogel series. The data are shown as log C_p/T^3 vs. log T to emphasize the different regimes and deviations from Debye behaviour. T_ξ and T_R indicate crossover temperatures. Oxidation of the samples removes organic rest groups attached to the inner surface of the gel, thereby decreasing the specific heat in the range corresponding to onset of particle modes. Dots: Amorphous silica data[1].

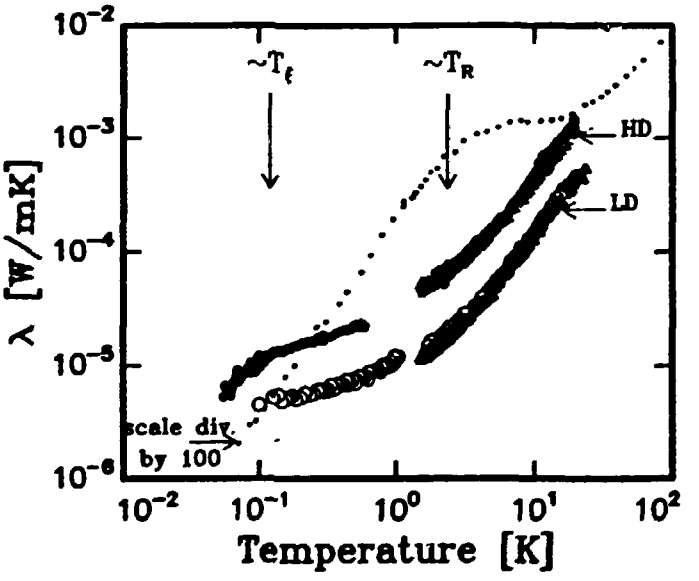

Fig. 3. Thermal conductivity data for the homologous aerogel series in double logarithmic representation. T_ξ and T_R indicate crossover temperatures. Oxidation do not influence the thermal conductivity (filled points correspond to oxidized samples). Dots: Amorphous silica data on a scale divided by hundred[1].

[1] R.C. Zeller and R.O. Pohl, (1971). Phys. Rev. B 4, 2029.

1.57 A Comparison of Results from SANS, PAT and TEM for Bulk Cu Containing Krypton During Isochronal Annealing

(J. Skov Pedersen, *Physics Department, Riso National Laboratory, Denmark*, M. Eldrup and A. Horsewell, *Materials Department, Riso National Laboratory, Denmark*)

It is generally recognized that in the studies of gases in solids no single experimental technique provides a full picture of the microscopical parameters (*e.g.* defect concentrations, size distribution, gas density). We have therefore combined Small Angle Neutron Scattering (SANS), Transmission Electron Microscopy (TEM) and the Positron Annihilation Techniques (PAT) to investigate bulk samples of Cu containing 3 at. % of Kr. The samples were obtained from Harwell, U.K.[1], where they were produced by a combined sputtering and implantation method. In the present study we have given special attention to preparing *identical* samples used in the application of the three different techniques. The samples were studied as-prepared and annealed to 275 °C, 425 °C and 575 °C.

The PAT investigations give information on the positron lifetimes which have a simple relation to the density of Kr in the gas bubbles[2]. Assuming equilibrium Kr bubbles the density can be used to calculate the bubble radii r. These are given in the table (in Å) together with the volume fraction S (in %) as derived from the Kr density in the bubbles and the value for the atomic percentage of Kr determined by high temperature outgasing. Also shown in the table are the results from SANS and TEM. The SANS results were derived from an indirect Fourier transformation[3] of the scattering data. The transformation gives the correlation function of the bubbles which was interpretated in terms of a two shell model. The inner shell describes the bubbles and the outer shell describes a volume outside the bubble which is depleted of Kr. The volume fraction is found by determining the bubble concentrations using the Kr density determined by PAT to calculate the scattering contrast between the bubbles and the Cu matrix. The TEM results are derived from the measured size distributions and estimates of the bubble densities. The results in the table are not in good agreement. When comparing radii, however, one should keep in mind the difference between the techniques in the weighting of small bubbles relative to large ones when calculating the average radii that are dispalyed in the table. For PAT the detection probability is roughly proportional to r^{α}, where α is between one and two. For the SANS measurements the scattering power of a bubble is proportional to r^6, and consequently the large bubbles are heavily weighted. For TEM, resolution problems for small bubbles also weight large bubbles.

	PAT		SANS		TEM	
T_{ann}	r (Å)	S (%)	r (Å)	S (%)	r (Å)	S (%)
as-prep.	15	8.2	11	2.6		
275 °C	11	8.3	11	3.1	6	1.7
425 °C	26	10.5	28	5.1	12	4.9
575 °C	53	13.7	38	7.4	25	4.1

The size distributions have also been determined from the SANS data. The bubbles were assumed to be spherical and the bubble-bubble correlation effects were modelled by using the structure factor for hard spheres[4]. It was assumed that the hard sphere radius is

proportional to the actual radius and that bubbles with a certain size are surrounded only by spheres of the same size (a local mono-disperse model). The determined *volume* distributions are shown in Fig. 1. The distribution is centered around 10 Å for the two lowest annealing temperatures, whereas the center of the distribution moves to higher values for higher annealing temperatures. A small contribution of bubbles with small radii seems to persist even at the two highest temperatures. This is in disagreement with the size distributions determined by TEM. However, for all annealing temperatures there is a fair agreement between the size distributions determined by SANS and TEM for the bubbles with large radii.

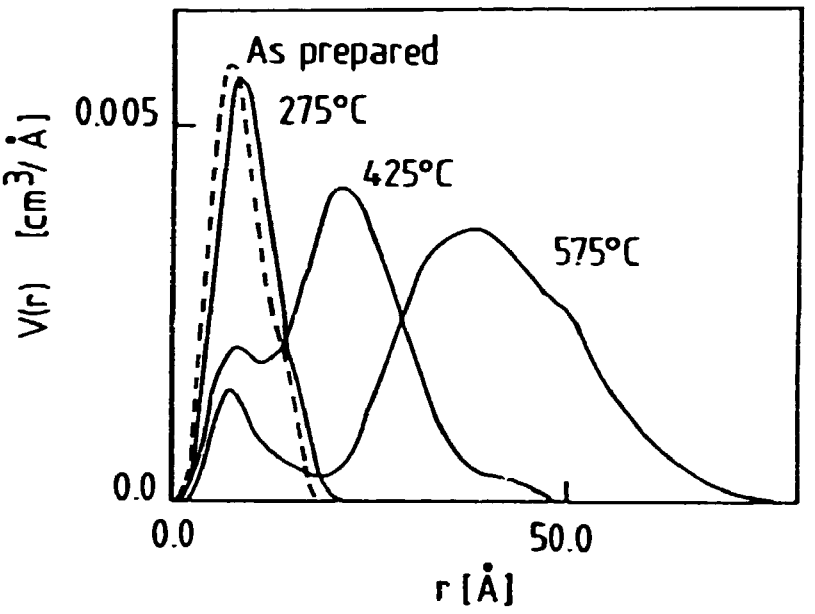

Fig. 1. The volume distributions determined from the SANS data.

[1] D.S. Whitmell, R.S. Nelson, K.J.S. Smith and G.J. Bauer, (1983). Eur. Appl. Res. Reports - Nucl. Sci. Techn. **4**, 513.

[2] K.O. Jensen, M. Eldrup, N.J. Pedersen and J.H. Evans, (1988). J. Phys. F: Met. Phys. **18**, 1703.

[3] O. Glatter, (1977). J. Appl. Cryst.**10**, 415.

[4] J.D. Kinning and E.L. Thomas, (1984). Macromolecules **17**, 1712.

1.58 Cavity Growth Rates in Fatigued Copper

(J. G. Barker, J. R. Weertman, *Northwestern University, Evanston, Illinois, USA* and J. Skov Pedersen, *Physics Department, Riso National Laboratory, Denmark*)

Materials stressed at high temperatures (0.4-0.7 times the melting temperature) fail by the nucleation, growth, and coalescence of grain boundary cavities. Diffusional growth of cavities in materials under static stress has been adequately described[1], but predicts no net growth under fully reversed fatigue conditions. By including a second order stress dependence of the grain boundary diffusivity, a small net growth rate is expected[2], but in practice, the cavity growth rate under fatigue matches or exceeds that under creep conditions. Other mechanisms involving plastic strain or gas stabilization have also been proposed[3-5].

In a previous study the dependence of the cavity growth rate on the fatigue frequency was determined[6]. The present study determines the stress amplitude dependence of the cavity growth rate. A weighted average cavity size, $R_p = < R^3 > / < R^2 >$, is measured by combining precision density measurements (PDM) to determine the cavity volume fraction, V_v, with small angle neutron scattering (SANS) measurements in the Porod region (q^{-4} behaviour of the intensity, where q is the modulus of the scattering vector) to determine the total cavity surface area, S_v. A characteristic cavity volume is defined as: $V_p = \frac{4}{3}\pi R_p^3$; $R_p = 3V_v/S_v$; a characteristic cavity number density as: $N_p = V_v/V_p$. V_p and N_p will give estimates of the cavity growth and nucleation rates, respectively.

Nominally 99.999% pure copper samples were fatiqued at temperature 678 K and frequency $\nu = 17\ s^{-1}$. The stress amplitude $\Delta\sigma$ was varied from 7 to 48 MPa. The number of fatigue cycles was varied from $9 \cdot 10^6$ at 7 MPa stress amplitude to $7 \cdot 10^4$ at 48 MPA. The measured cavity volume fractions V_v varied from $3 \cdot 10^{-4}$ to $3 \cdot 10^{-3}$. The measured specific cavity surface areas varied from 2 to 15 mm^{-1}. The characteristic cavity volumes V_p varied from 0.3 to 4.0 μm^3.

The SANS data near the beam deviates from the Porod law as shown as solid symbols in Fig. 1, with the Porod law expressed as a horizontal line in the plot. The deviation has been attributed primarily to collimation smearing. To determine how smearing effects data, both the true scattering intensity dependence upon the scattering vector q and the probability distribution of q measured at a fixed detector element position must be known or estimated. The distribution of q depends upon the dimensions of the apertures, flight paths, detector resolution function, and wavelength spread of the velocity selector.

Assuming the data to actually follow the Porod law, the smearing effect was modeled. Using the method of Skov Pedersen *et al.*[7], the probability distribution of the scattering vector has been analytically modeled to fit Gaussian functions based upon the characteristics of the SANS instrument. The dashed curve in Fig. 1 represents the above smearing calculation. In addition, in the present work a numerical method has been developed that calculates the shape of the probability distribution of the scattering vector for the circular aperture geometry, including beamstop shadowing. The analytical expressions in[7] for the fitted Gaussian-like functions will be modified to include beamstop shadowing in the future. The solid curve in Fig. 1 represents the numerical calculations. The agreement

between the smearing calculations and the experimental data indicates that combined smearing and beamstop shadowing effects cause the observed deviation from the Porod law.

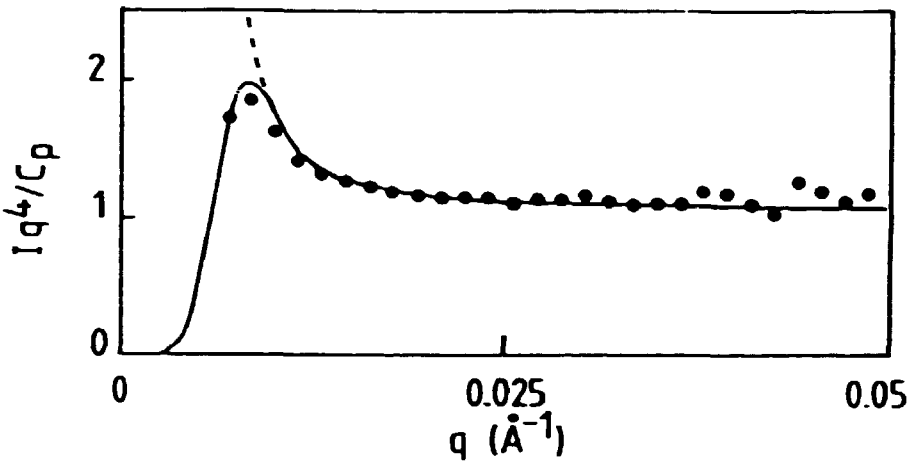

Fig. 1. A Porod plot of the observed scattering. Dashed curve: Porod scattering smeared by the Gaussian-like resolution function[7]. Solid curve: Smeared Porod scattring calculated by the numerical method.

The scattering measurements also showed a transition from circular to square scattering contours with increasing degree of cavitation. Cavities formed during the high temperature fatigue of copper have been found to form on grain boundaries aligned preferentially 30° to 60° to the stress axis[8]. Calculations indicate that the combination of the preferred cavity orientation with cavity elongation with increasing degree of cavitation will cause the observed transition from circular to square scattering contours. The present measurements combined with previous measurements made on copper[6], have determined an empirical correlation of the cavity growth rate dV_p/dt with stress amplitude $\Delta\sigma$ and frequency ν : $dV_p/dt = 4 \cdot 10^{-8}\nu^{0.47}(\Delta\sigma)^{1.9}\mu m^3/s$.

From the frequency and stress amplitude dependence of the plastic strain amplitude $\Delta\epsilon_p$, the above correlation can also be represented as: $dV_p/dt = 8 \cdot 10^{-3}(\Delta\epsilon_p)^{0.5}$. In summary, by combining PDM and SANS measurements, a characteristic cavity size and number density can be estimated. Measurements on fatigued copper samples indicate: i) Smearing of the data near the beam causes the observed deviation from the Porod law. ii) The square-like intensity contours indicate oblate ellipsoid shaped cavities are aligned 45° to the stress axis. iii) The cavity growth rate depends upon the stress amplitude squared. iv) The growth rate depends upon the plastic strain rate to the power 1/2.

1) M.V. Speight and W.J. Beere, (1975). Met. Sci. **9**, 190.
2) J. Weertman, (1974). Met. Trans. **5**, 1743.
3) R.P. Skelton, (1966). Phil. Mag. **14**, 563.
4) A.J. Gittins, (1968). Met. Sci. **2**, 51.
5) H. Trinkaus, (1981). Script Met. **15**, 825.
6) J.G. Barker and J.R. Weertman, (1990). Scripta Met. **24**, 227.
7) J. Skov Pedersen, D. Posselt and K. Mortensen, (1990). J. Appl. Cryst. **23**, 321.
8) T. Saegusa and J.R. Weertman, (1978). Scripta Met. **12**, 187.

1.59 Results of Flux and Resolution Function Calculation for SAXS Setups Using the Gaussian Formulation of Phase-Space Analysis

(J. Skov Pedersen, *Physics Department, Riso National Laboratory, Denmark* and C. Riekel, *European Synchrotron Radiation Facility, Grenoble, France*)

We have recently developed a method for calculating the flux at the sample position and the width of the resolution function in reciprocal space for Small Angle X-ray Scattering (SAXS) setups[1]. The method is a mathematical formulation of the general phase-space description given by Matsushita and Kaminaga[2]. In our method the intensity of the source, the acceptance windows of the slits and of the monochromator are decribed by Gaussian functions. We have further given formula for transforming these distributions along the beam line. When using Gaussian functions it is particularly simple to calculate total fluxes and beam sizes at any position along the beam line. We have further calculated the resolution function which describes the instrumental smearing of the ideal cross-section.

As an example we have performed calculations for the setup shown in Fig. 1. It consists of an elliptical mirror and a focusing monochromator crystal. The mirror focuses in the vertical plane and the crystal in the horizontal plane. In order to achieve ideal focusing the surface of the monochromator crystal makes an angle relative to the scattering crystal planes. Slits are situated in front of the mirror, after the monochromator and just before the sample. The first slit is the defining slit, whereas the two other slits only removes parasitic scattering from the optical elements and the slits closer to the source. Thus only the first defining slit need to be included in the calculations. A FORTRAN programme for calculating fluxes, beam sizes and resolution has been written making it very easy to describe several different setups of the type shown in Fig. 1 by changing only a set of input parameters.

The first numerical example concerns the setup described by Hendrix *et al.*[3] using the storage ring DORIS at DESY in Hamburg as source. For the ring parameters 4.7 GeV and 20 mA, we have extimated the brilliance of the source to be about $6 \cdot 10^{20}$ photons/s/(rad)^2/(mm)^2 per unit wavelength band at a wavelength of 1.5 Å. For these parameters we get a flux of $1 \cdot 10^{11}$ photons/s compared to the value $(5 \pm 2) \cdot 10^{11}$ photons/s as mesured by Hendrix *et al.* by an ionization chamber. The beam size at the detector is calculated to be 0.8 × 1.1 mm^2 in the vertical and horizontal direction, respectively. The wavelength spread is very small and contributes marginally to the resolution, which is described by the variances $3.5 \cdot 10^{-4}$ Å^{-1} in the vertical direction and $5.4 \cdot 10^{-4}$ Å^{-1} in the horizontal direction.

The second numerical example concerns a comparison with flux calculations by conventional phase-space analysis[4] for a laboratory setup using a rotating anode as source. The source size is 0.1 × 0.1 mm^2 and the brilliance at 40 keV and 40 mA is estimated to be $2.5 \cdot 10^{17}$ photons/s/(rad)^2/(mm)^2 per unit wavelength band at a wavelength of 1.54 Å. The table shows the values for the flux found by conventional phase-space analysis for several different combinations of mirrors and monochromators compared to our method. The label 'multi' refers to a setup in which a multilayer has been used instead of a mirror. In combination with the perfect crystal monochromator the multilayer effec-

tively works just as a mirror. From the values in the table it is seen that the Gaussian formulation of the phase-space analysis agrees very well with the conventional analysis.

Table 1. Fluxes in units 10^7 photons/s for the laboratory setup.

Mirror/mono	Glass/SiO_2(10.1)	Pt/SiO_2(10.1)	Ni/Ge(111))	Multi/Ge(111)
conv.	0.57	0.75	0.94	4.9
Gauss.	0.55	0.74	1.49	5.5

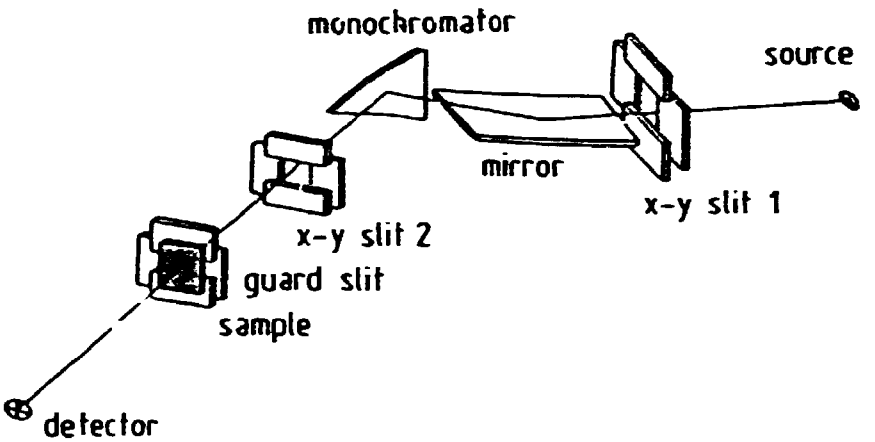

Fig. 1. The small angle X-ray scattering setup.

[1] J. Skov Pedersen and C. Riekel, (1991), *to appear in* J. Appl. Cryst. (see also the Annual Progress Report (1989)).
[2] T. Matshushita and U. Kaminaga, (1980). J. Appl. Cryst. **13**, 465 and 472.
[3] J. Hendrix, M.H.J. Koch and J. Bordas, (1979). J. Appl. Cryst. **12**, 467.
[4] C. Riekel, and P. Suortti, (1991), *to appear in* J. Appl. Cryst.

1.60 Beam Deflection in Laue and Bragg Monochromator Geometries

(J.Als-Nielsen and M. Wulff, *Physics Department, Risø National Laboratory, Denmark*)

An X-ray beam incident on a liquid surface at glancing angles may be specularly reflected (XR), diffracted (GID) or yield fluorescent radiation (GIF), see Fig. 1. The three mechanisms, encompassing liquid surface X-ray spectrometry, give complementary information about the liquid surface structure. In common is the incident monochromatic beam: It has the shape of a downward sloping thin sheet with the sheet normal and the propagation direction ideally spanning a vertical plane. In order to produce such a beam sheet one can utilize reflections from a synthetic multilayer crystal and an ordinary mirror as discussed in the next contribution. Here we compare the conventional method of Bragg scattering from a crystal in reflection (Bragg) geometry with Bragg scattering from a crystal in transmission (Laue) geometry.

The scattering geometry for both cases is shown in Fig. 2: The incident beam propagating along the unit vector $\mathbf{k}_1$ with a vertical sheet normal $\mathbf{n}_1$ is Bragg scattered by atomic net planes having a common normal τ tilted downwards from the horizontal plane by an angle t. The propagation direction of the monochromatic beam $\mathbf{k}_2$ is therefore tilted downwards by an angle α , but unfortunately also the diffracted beam *sheet* is being skewed. The skew angle s between the sheet normal $\mathbf{n}_2$ and the normal to a horizontal line perpendicular to $\mathbf{k}_2$ depends on whether the crystal surface coincides with the diffracting atomic planes (Bragg geometry) or is perpendicular to them (Laue geometry). One can derive the following relations between the skew angle s, the deflection angle α, and the angle ϕ given in the figure (the Bragg angle for zero tilt):

$$\textit{Bragg Geometry} : \sin s = \tan\alpha / \tan\phi$$

$$\textit{Laue Geometry} : \sin s = -\tan\alpha \cdot \tan\phi$$

Ideally the skew angle s should be zero. At relatively small Bragg angles ($\phi < 25°$) the Laue geomtry is more advantageous. The Laue geometry for a thin crystal, *i.e.* only small absorption, has another advantage: apart from the narrow wavelength band extracted by the monochromator crystal from the white spectrum of the synchrotron radiation beam, this beam traverses essentially unaffected further downstream where it can be utilized for other experimental stations. A suitable crystal for this kind of application might be a Beryllium single crystal wafer of about 0.5 mm thickness and with a mosaic width of about one minute of arc. This possibility is currently being investigated in collaboration with ESRF, Grenoble.

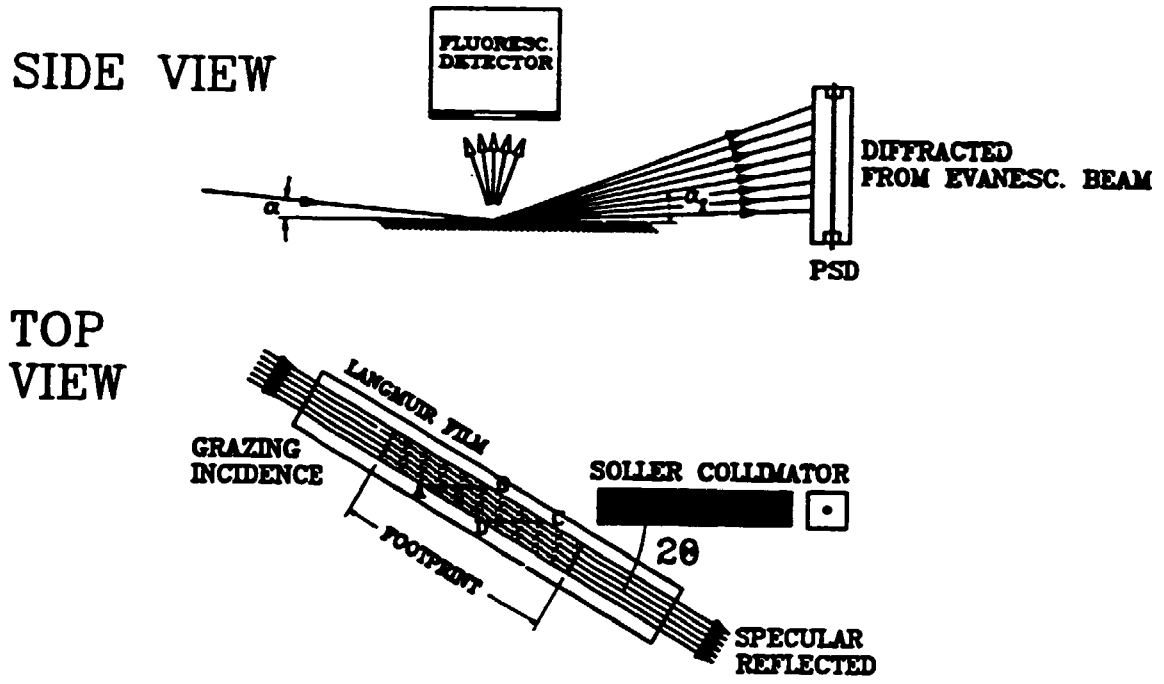

Three applications of grazing incidence X-rays on a smooth surface: Specular reflection, diffraction and fluorescence.

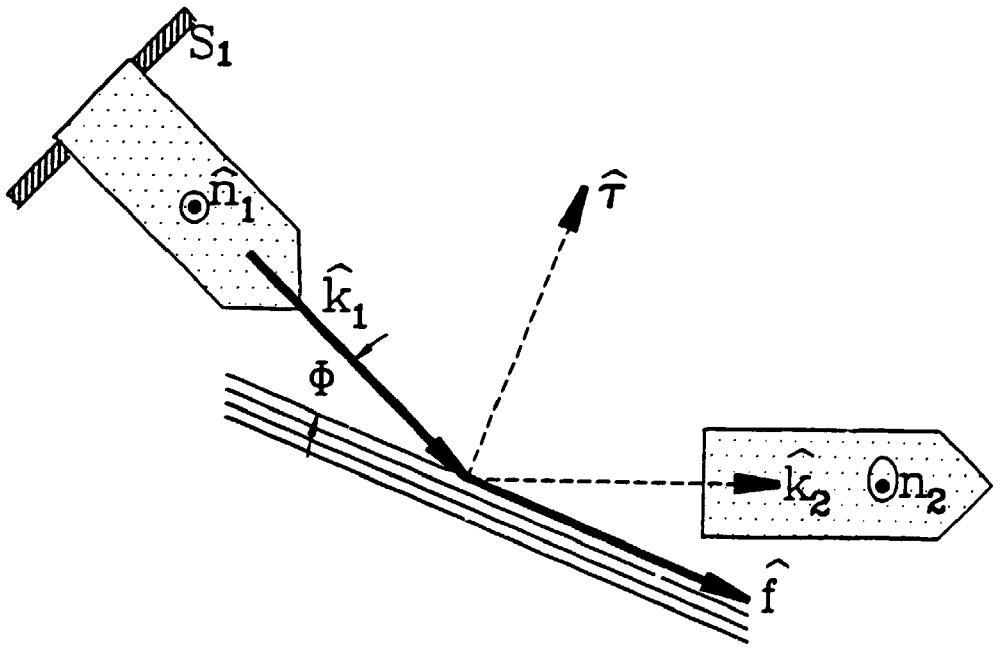

Bragg scattering geometry when an incident horizontal beam sheet (index 1) is Bragg scattered from a tilted monochromator with reciprocal lattice vector τ to a diffracted beam sheet given by its propagation direction $\mathbf{k}_2$ and sheet normal $\mathbf{n}_2$.

1.61 A Synthtetic Multilayer Crystal-Mirror Beam Defiector

(J.Als-Nielsen and F. Grey, *Physics Department, Riso National Laboratory, Denmark*)

A Synthtetic Multilayer Crystal (SMC) consisting of alternating layers of W (25 vol%) and Si (75 vol%) with a total d-spacing of 25 Å was examined at the Riso X-ray laboratory source with respect to peak reflectivity, R_o, and relative band width, w. The experiemental values R_o = 78%, W= 2.1% are in excellent agreement with the theoretical predicition outlined below. The SMC of W_xSi_{1-x} is shown in the top part of the figure. The electron density in the W layer is 4.65 electrons/Å^3 and in the Si layer 0.7 electrons/Å^3 giving a contrast density of ρ = 3.95 electrons/Å^3. The *amplitude* reflectivity of a single layer, r_1, is proportional to this density times the W-layer thickness xd divided by $\sin\theta$. It is also proportional to the scattering length of a single electron, r_o, and to the X-ray wavelength $\lambda = 2d\sin\theta$. The finite thickness of the W-layer implies a dimensionless formfactor, f which for $x = 0.25$ amounts to 0.9 for the first order Bragg reflection. Altogether the *amplitude* reflectivity per layer amounts to

$$r_1 = \rho r_o(2d^2)xf = 0.031$$

Another quantity of interest is the amplitude absorption, h_1, per layer. The path length is $d/\sin\theta$ so the intensity is attenuated by $\mu d/\sin\theta$ and the amplitude by half of that:

$$h_1 = \mu d/(2\sin\theta) = 0.0039$$

It is clear that the relative band width w must be proportional to r_1 and that the loss in peak reflectivity is expressed by h_1/r_1. The explicit formulae are:

$$w = 3/(\sqrt{2}\pi)r_1 = 0.021$$

$$R_o = (1 - h_1/r_1)^2 = 0.78$$

both in excellent agreement with the experimental findings.

The bottom part of the figure shows beam deflection by an SMC followed by a conventional mirror. The SMC provides a fixed wavevector transfer, $Q_{ml} = 2\pi/d$ whereas the mirror can be tilted to provide any wavevector transfer up to the critical value, Q_c, for total reflection. Explicitly,

$$Q_c = 4(\pi\rho_{mi}r_o)^{1/2}$$

The footprint (*c.f.* previous contribution) due to a finite beam height sets in practise a lower limit of 0.3 Qc for the wavevector transfer Q_{mi} from the mirror. The angular deflection α_{res} resulting from succesive reflections from the SMC and the mirror is given by

$$2k\alpha_{res} = Q_{ml} + Q_{mi}$$

By utilizing a striped SMC with a variety of discrete d spacings that can be inserted into the beam a wide *continuous* range of deflection angles can be obtained. This arrangement provides a high throughput and it maintains a horizontal intersection between the reflected beam sheet and a vertical plane if the incident beam sheet is horizontal.

The crystal was produced by Ovonic Synthetic Materials Company, Inc. Troy, Michigan, U.S.A.

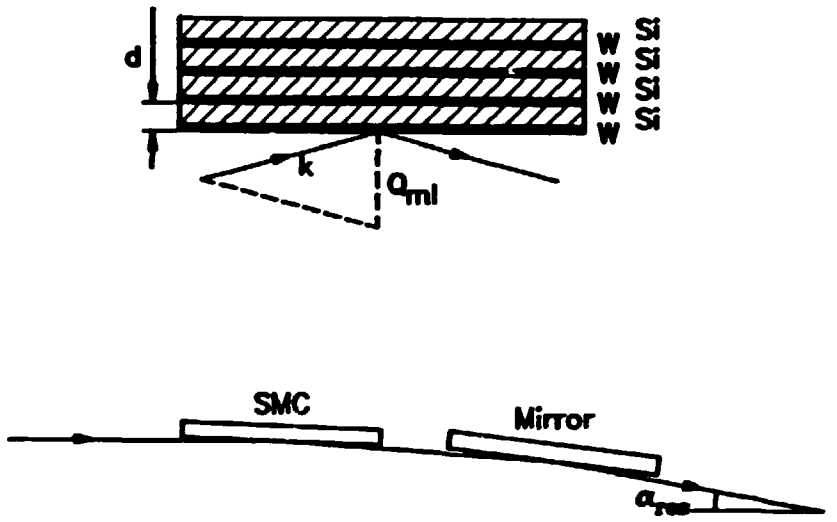

Top part: A Synthetic Multilayer Crystal (SMC) of W (heavily shaded) and Si (light shaded) with a total d-spacing of 25 Å. Bragg scattering corresponds to a wave vector transfer Q_{ml} also indicated. The 200 layers of W and Si was eavporated on a Si wafer substrate. Bottom part: Succesive reflections from an SMC and a conventional mirror provides a resulting deflection angle α_{res}; the corresponding wavevector transfer $2k\alpha_{res}$ is the sum of Q_{ml} and Q_{mi}.

1.62 The Liquid Surface Neutron Reflectometer at Risø

(D. Vaknin, K. Kjær and J. Als-Nielsen, *Physics Department, Risø National Laboratory, Denmark*)

A first prototype constant wavelength neutron reflectometer has been constructed and succesfully tested at the guide hall of the DR3 reactor at Risø. The reflectometer is designed according to the principles used by Als-Nielsen and Pershan[1] in their construction of a first prototype X-ray reflectometer for the study of gas-liquid interfaces. The reflectometer uses a constant wavelength neutron beam (in the range $\lambda = 3.7 - 4.8$ Å) which is selected by Bragg reflection from the (002) planes of a Highly Oriented Pyrolytic Graphite crystal (spacing $d = 3.355$ Å, mosaic spread : 0.4 degrees FWHM). The monochromator is mounted on a motorized axis to tilt the normal of the reflecting planes away from the horizontal, consequently bending the incident beam to any desired glancing angle (in the range of 0-7°) with respect to the liquid surface. The vertical divergence and the vertical angle of the incident beam onto the sample are determined by a pair Gd_2O_3 coated Cd slits which are adjustable both in height and in width and are located at the entrance and exit of an 80' collimator which provides horizontal collimation. The incoming neutron intensity is continuously monitored with a ^3He (0.05 atm) detector just in front of the sample. Typical intensities of the primary beam at full opening slit width ($W = 4$ mm) are about 40,000 counts/s.

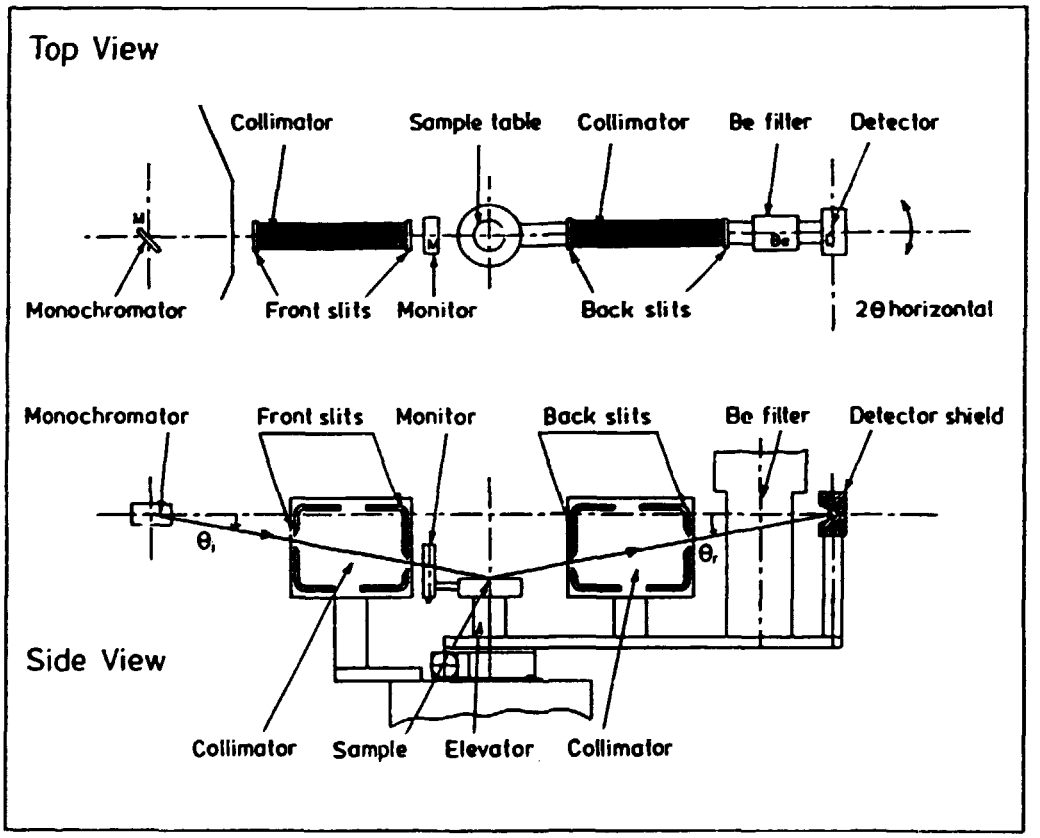

Fig. 1. Schematic top and side views of the Liquid Surface Neutron Reflectometer at Risø.

The reflected beam is passed through a slit-collimator-slit system in an arrangement symmetrical to the incidence side with a ^{3}He detector (5 atm) in a position symmetrical to the monochromator. A liquid-nitrogen cooled Be filter mounted between the last slit and the detector discriminates against the $\lambda/2$ component in the beam to better than 2%. For wavelengths around 3.7 Å we found that the $\lambda/2$ component in the primary beam was less than 6% and need not be filtered in practice. For the determination of the background count rate at each momentum transfer value, q_z, the detection arm is rotated out of the specular position horizontally to either side by 3°. The reflectometer is controlled by a PC using the software package TASCOM developed at Risø.

Currently the reflectometer is used for the study of the structural properties of monomolecular monolayers on aqueous subphases, H_2O or D_2O. Monolayers are prepared in a film balance that has been used for X-ray reflection experiments and was remodeled to incorporate Al windows to transmit neutron radiation. H_2O for the subphase is purified by a filtration plant (Milli-Q; Millipore Corp., Bedford, MA). The D_2O can be distilled (also from $KMnO_4$) in a one stage quartz/PTFE distillation plant (Normag AG, Hofheim/Ts., FRG).

Table 1: Features of the Liquid Surface Neutron Reflectometer at Risø

Monochromator	Graphite (002) $\tau = 1.873$ Å^{-1}, with an extra degree of rotation to tilt the beam onto the sample
Wavelength	3.7 – 4.8 Å
Detector	5 atm ^{3}He (limited vertical translation)
Monitor	0.05 atm ^{3}He (translating vertically with sample)
Slits	4 adjustable (height H_i and W_i opening,) Gd_2O_3 coated Cd screens. S_i
Distances	Monochromator to S_1: 272 mm Monochromator to S_2: 675 mm Monochromator to Sample to Detector: 940 mm Detector to S_3: 675 mm Detector to S_4: 273 mm Distances can vary slightly each installment
q_z range	0.0 – 0.4 Å^{-1}
Resolution	0.002 – 0.03 Å^{-1} (depending on slits)
Reflectivities	down to 10^{-6}
Backgorund	3 cts/min (minimum)
Filter	Liquid-Nitrogen Cooled Be
Collimators	30', 80' and 4° available
Analyzer (optional)	(002) HOPG, (with extra rotation)
Sample Area	30 x 50 mm^2 (minimum)

[1] J. Als-Nielsen and P. S. Pershan, (1983). Nucl. Inst. Meth. **208**, 545.

1.63 Intensity versus Resolution. A Comparison between the "Symmetrical" and "Asymmetrical" SANS Spectrometers

(A.N. Falcão, J. Skov Pedersen and K. Mortensen. *Physics Department, Risø National Laboratory, Denmark*)

The optimum design of a SANS spectrometer has been considered to be that in which the length of the flight path from source to sample (L_1) equals that of the flight path from sample to detector (L_2)[1-2] — the "symmetrical ($L_1 = L_2$) design". Recently it has been shown[3-4] that the highest count rate (C_d) at the detector is obtained when the instrument's dimensions, both longitudinal and transverse, are made as large as possible (the limits being imposed both by the requirements of the physics of the sample to investigate, and by the maximum physical dimensions of the geometrical parameters). In practice this resumes to either use the full available space for the spectrometer, or alternatively, the full neutron source available, and leads to spectrometer lay-outs that are, in general, asymmetrical ($L_1 \neq L_2$).

Since this last result has been matter for some controversy, we made an experimental test to see if an already existing spectrometer (the Risø SANS) could improve its performance by making use of the asymmetrical lay-out. The sample used in the test was formed by lamellar bilayer membranes of dimyristoylphosphatidylcholine (DMPC) mixed with 14% cholestrol. The (10) Bragg reflection characteristic of the bilayer periodicity ($q \sim 0.1$ Å^{-1})[5] was used in the comparison. The reflection was recorded for five sets of wavelength, range of scattering vector q and resolution in q. For each set, two measurements were made: one using the $L_1 = L_2$ design, and another using the $L_1 \neq L_2$ design. For the $L_1 \neq L_2$ design, the values of the geometrical parameters were chosen according to[4], assuming a spatial resolution of the detector equal to 8 mm. The expected FWHM of the peaks were then estimated following[6]. The results obtained can be seen in the table presented below. The values for the measured intensities and FWHM of the Bragg peaks were determined by fitting the experimental data with a Gaussian-like expresssion for the resolution function superposed on a linear background. The width of the peaks was treated as a varying parameter. The intensities and intrinsic widths of the peaks were checked using an already developed least-squares fitting program where the resolution function[6] describing the smearing of the ideal cross-section is implemented.

Lay--Out	Setting						ΔQ Calc Ref[6] (Å^{-1})	Measured Values ΔQ (Å^{-1})	Measured Values C_d (arb)	$C_d(Asy)/C_d(Sym)$ Ref[4]	$C_d(Asy)/C_d(Sym)$ Measured
	N	λ (Å)	L_1 (m)	L_2 (m)	ϕ_{NS} (mm)	ϕ_S (mm)					
Sym	1	3	2.0	2.0	13.0	6.5	0.0230	0.0258	19.30		
Asy	2	3	3.0	2.0	19.5	7.8	0.0230	0.0260	29.81	1.44	1.54
Sym	3	3	3.0	3.0	13.0	6.5	0.0198	0.0208	5.07		
Asy	4	3	5.0	3.0	21.6	8.0	0.0198	0.0211	7.77	1.52	1.54
Sym	5	3	4.0	4.0	13.0	6.5	0.0185	0.0186	1.46		
Asy	6	3	6.0	4.0	19.5	7.8	0.0185	0.0186	2.40	1.44	1.64
Sym	7	6	1.0	1.0	13.0	6.5	0.0238	0.0300	36.49		
Asy	8	6	2.0	1.0	25.0	8.6	0.0236	0.0304	70.04	1.78	1.92
Sym	9	6	2.0	2.0	13.0	6.5	0.0185	0.0231	4.64		
Asy	10	6	3.0	2.0	19.5	7.8	0.0185	0.0232	7.29	1.44	1.57

L_1 and L_2 are the flight path lenghts; ϕ_{NS} and ϕ_S are the source and sample pin-hole diameters; ΔQ is the FWHM of the peaks.

We note that:

1) For each set of wavelength, range of q and resolution in q, the FWHM of the peaks measured in the $L_1 = L_2$ and the $L_1 \neq L_2$ spectrometers are in excellent agreement;

2) The asymmetrical lay-out is better performing than the symmetrical one. Given the wavelength, it allows to measure a certain range of q with a given resolution with higher count rate than the symmetrical lay-out. This is clearly seen in Fig. 1. where the spectra recorded with settings 1 and 2 are plotted;

3) The measured intensity gains are slightly higher than the predicted ones. This can be produced by several factors that are difficult to account for. We mention five : i) Non uniform illumination of the source pin-hole; ii) Non uniform angular distribution of the neutrons transmited by the collimation; iii) Small errors in the pin-hole dimensions; iv) Incertainty in the neutron source pin-hole position due to umbra and penumbra effects produced by the collimation on the neutron guides; v) Increase in the wavelength spread due the presence of neutron guides in the space that separates the mechanical velocity selector from the neutron source pin-hole.

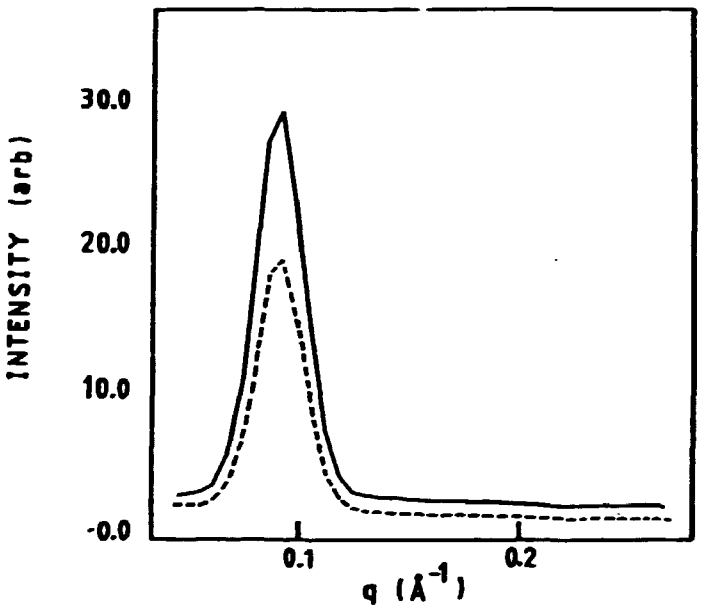

Fig. 1. Intensity versus Q,measured with 9 Å neutrons (radial averaged raw data). Full line: asymmetrical lay-out ($L_1 = 3$ m, $L_2 = 2$ m, $\phi_{NS} = 19.5$ mm, $\phi_S = 7.8$ mm, $\Delta l = 8.0$ mm). Dashed line: symmetrical lay-out ($L_1 = 2$ m, $L_2 = 2$ $\phi_{NS} = 13.0$ mm, $\phi_S = 6.5$ mm, $\Delta l = 8.0$ mm). The better performance of the asymmetrical spectrometer lay-out is clear.

[1] W. Schmatz, T. Springer, J. Schelten and K. Ibel, (1974). J. Appl. Cryst. 7, 96.

[2] D.R.F. Mildner and J.M. Carpenter, (1984). J. Appl. Cryst. 17, 249.

[3] F.M.A. Margaça, A.N. Falcão, J.F. Salgado and F.G. Carvalho, (1989). Nucl.Instr. & Meth. A274, 606.

[4] F.M.A. Margaça, A.N. Falcão, J.F. Salgado and F.G. Carvalho, (1990)."Solving the Problem of a Small Angle Neutron Scattering Spectrometer Optimization", *submitted.*

[5] K. Mortensen, W. Pfeiffer, E. Sackmann and W. Knol, (1988). Bioch. Biophys. Acta, 945, 221.

[6] J.S. Pedersen, D. Posselt and K. Mortensen, (1990). J. Appl. Cryst. 23, 321.

1.64 In Situ X-ray Diffraction Experiments on Copper Containing Catalyst Samples

(G. Fabius, B.S. Hammershøi, G. Steffensen, B. Clausen, *Haldor Topsoe A/S, Lyngby, Denmark*, and R. Feidenhans'l, *Physics Department, Risø National Laboratory, Denmark*)

In situ X-ray powder diffraction can be used to obtain information about structural changes in a catalyst during a reaction. We have performed measurements at the rotating anode in the Physics Department with a newly developed diffractometer on the high pressure cell developed at Haldor Topsøe A/S. Model compounds consisting of a mixture of CuO and $CuAl_2O_4$ were reduced in a gas composed by 5% H_2, 0.4% CO, 5% CO_2 and 3% Ar in N_2. X-ray diffraction spectra, recorded with a position sensitive detector, were measured as a function of temperature in the range from room temperature to 400 °C. An example is shown in the figure. It was observed that the reduction of a mixture of the two copper containing phases gives rise to a bimodal size distribution of metallic crystallites.

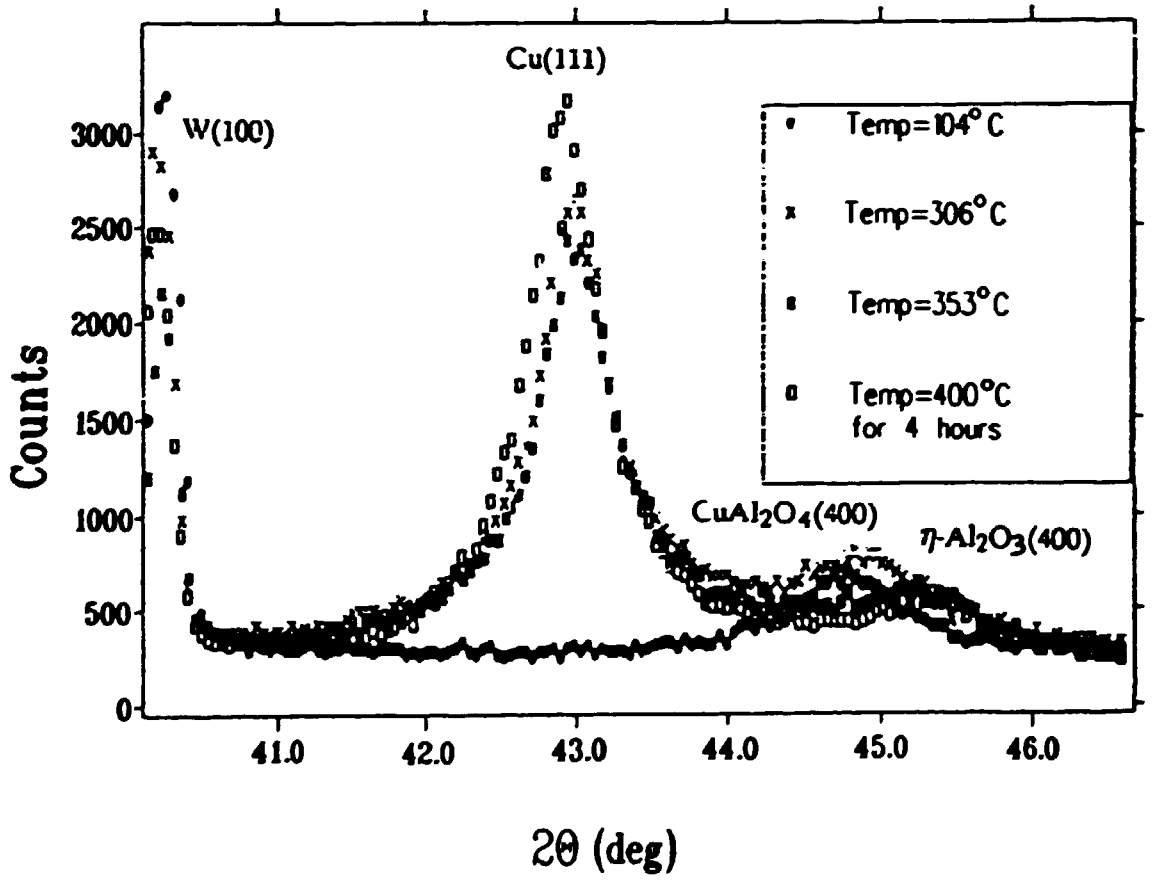

Diffraction diagrams of a model compound recorded at T=104 °C, 306 °C, 353 °C, 400 °C (after 4 hours) with a flow of reducing gas mixture.

1.65 The Growth of Pb on MgO(100)

(R. Feidenhans'l and T. Kjæ.. *Physics Department. Riso National Laboratory. Denmark*)

After a year with an overwhelming amount of technical problems. the metal-MBE has finally started operation. The technical problems were partly caused by a sample manipulator not fulfilling the specifications. The first project is the study of the growth of Pb on different surfaces. starting with MgO(100). More than 100 Å Pb was evaporated onto a MgO(100) surface at room temperatur. The Pb was evaporated from a Knudsen evaporation cell held at 600 °C. The growth rate was 1Å/s. The Pb forms three-dimensional islands on the surface. as evidenced by Reflecting High Energy Electron Diffraction (RHEED). There is no epitaxial relation between the Pb and the MgO. the Pb overlayer is polycrystalline (see figure). Investigations at different MgO temperatures and different substrates are in progress.

RHEED pattern of a polycrystalline Pb film on MgO(100).

1.66 The Liquid He Plant

(K. Christensen and M. Nielsen, *Physics Department, Risø National Laboratory, Denmark)*

For the year 1990 the following quantities of liquid He were delivered: 47,200 liter. Of this 38,700 liter He are used outside Risø.

HELIUM PRODUCTION

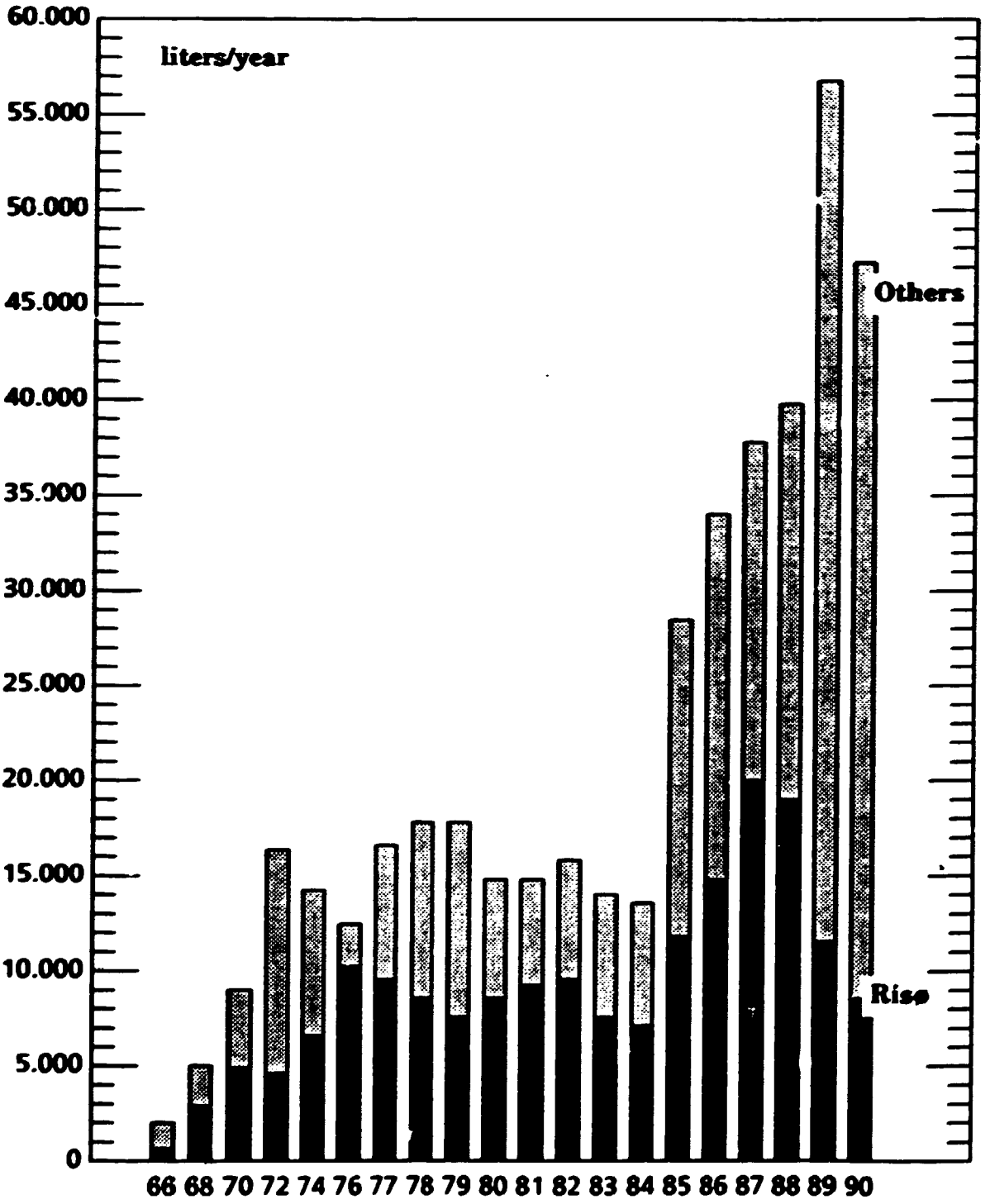

2 PARTICIPANTS IN THE WORK IN THE DEPARTMENT

Scientific Staff

Als-Nielsen, Jens (Head)
Andersen, Niels Hessel
Bohr, Jakob
Buras, Bronislaw (Part time consultant)
Clausen, Kurt Nørgaard
Feidenhans'l, Robert
Grey, François
Kjær, Kristian
Lebech, Bente
Lindgård, Per-Anker
Mortensen, Kell
Nielsen, Mourits
de Reus, Roger
Skov Pedersen, Jan

Ph.D. Students and Students

Falcão, Antonio (From June 1)
Gråbæk, Lars
Kalsbeek, Nicoline (From the University of Copenhagen)
Kromann, Rasmus
Posselt, Dorthe (Until July 31)
Poulsen, Henning Friis
Harris, Pernille (Master's Thesis Student from the University of Copenhagen)

Technical Staff

Bang, Steen
Breiting, Bjarne
Christensen, Kaj
Dietrich, Caspar (Temporary assistant)
Hansen, Danny Glüich (From February 2 until November 4)
Hansen, Poul-Erik (From August 6)
Jensen, Louis Gordon (Until March 31)
Kjær, Torben
Kofoed, Werner (Until July 31)
Larsen, Arild B. (Temporary assistant)
Linderholm, Jens
Lund, Morits
Nielsen, Mads (Temporary assistant)
Nielsen, Steen
Rasmussen, Ove (From September 1)

Technical Staff (continued)

Stahl, Kim (From September 12)
Theodor, Kjeld
Thuesen, Allan

Secretaries

Astradsson, Lone (Until February 28)
Frederiksen, Lajla
Kjøller, Kæth (Until February 28)
Kloster, Margit
Lindbo, Anette (Apprentice and part time assistant, from July 15 until September 30)
Hansen, Berit (Apprentice, from November 1)

Guest Scientists and Long Time Visitors

Annila, A.J.	Helsinki University of Technology, Finland
Howard, B.	Cavendish Laboratory, Cambridge, U.K.
Oja, A.S.	Helsinki University of Technology, Finland
Touriniemi, J.T.	Helsinki University of Technology, Finland
Vaknin, D.	University of Pennsylvania, U.S.A.
Weinfurter, H.	Hahn-Meitner Institute, Berlin, Germany

Short Time Visitors (more than one week)

Achiwa, N.	Kyushu University, Fukuoka, Japan
Aeppli, G.	AT& T Bell Laboratories, Murray Hill, New Jersey, U.S.A.
Aliborn, J.	Institute Laue-Langevin, Grenoble, France
Almdal K.	University of Minnesota, Minneapolis, Minnesota, U.S.A.
Arts, A.	University of Utrecht, Utrecht, Holland
Bates, F.	University of Minnesota, Minneapolis, Minnesota, U.S.A.
Behan, M.	Daresbury Laboratory, Warrington, U.K.
Bishop, D.	AT& T Bell Laboratories, Murray Hill, New Jersey, U.S.A.
Broholm, C.	AT& T Bell Laboratories, Murray Hill, New Jersey, U.S.A.
Brooks, R. L.	Guelph University, Ontario, Canada
Brown, S.	Cambridge University, Cambridge, U.K.
Brown, W.	Uppsala University, Uppsala, Sweden
Bruls G.	Johannes Gutenberg Universität, Mainz, Germany
Bernhoeft, N.	Durham University, Durham, U.K.
Castán, T.	University of Barcelona, Barcelona, Spain
Chen, S.H.	M.I.T., Massachusets, U.S.A.
Christensen, A.N.	University of Århus, Århus, Denmark
Degenhardt, D.	HASY Laboratory, DESY, Hamburg, Germany
Doenni, A.	LNS, ETH, Zürich, Switzerland
Enderlee, M.	Hahn-Meitner Institute, Berlin, Germany
Fjellvåg, H.	University of Oslo, Blindern, Norway

Førland, G.	University of Bergen, Bergen, Norway
Furuseth, S.	University of Oslo, Blindern, Norway
Gay, J. M.	Faculté des Sciences de Luminy, Marseille, France
Graf, H.	Hahn-Meitner Institute, Berlin, Germany
Grybos, J.	Hahn-Meitner Institute, Berlin, Germany
Gürtler, P.	HASY Laboratory, DESY, Hamburg, Germany
Habekost, S.	University of Århus, Århus, Denmark
Heidelmann, M.	University of Kiel, Kiel, Germany
Johnson, R.L.	University of Hamburg, Hamburg. Germany
Gareth, J.	Daresbury Laboratory, Warington, U.K.
Kawano, S.	Kurri Research Reactor Institute, Kyoto University, Japan
Kakurai, K.	Johannes Gutenberg Universität, Mainz, Germany
Keller, L.	LNS, ETH, Zürich, Switzerland
Kleiman, R.	AT& T Bell Laboratories, Murray Hill, New Jersey, U.S.A.
Leiserowitz, L.	Weizmann Institute, Rehovot, Israel
Lösche, M.	Johannes Gutenberg Universität, Mainz, Germany
Mason, T.	AT& T Bell Laboratories, Murray Hill, New Jersey, U.S.A.
Meyer H. M.	Hahn-Meitner Institute, Berlin, Germany
Müller P.	The Technical High School of Aachen, Aachen, Germany
Nordby, P.	University of Odense, Odense, Denmark
Nordin, B.	Chalmers Institute of Technology, Göteborg, Sweden
Nummila, K.	University of Helsinki, Helsinki, Finland
Piepenstock, M.	Johannes Gutenberg Universität, Mainz, Germany
Plyte, H.	AT& T Bell Laboratories, Murray Hill, New Jersey, U.S.A.
Samseth, J.	IFE Kjeller, Norway
Sass, J.	Freie University, Berlin, Germany
Scherrenberg, R.	University of Leuven, Leuven, Belgium
Schjerven, J.F.	University of Oslo, Blindern, Norway
Shins, A.	University of Utrecht, Utrecht, The Netherlands
Sjöberg, B.	University of Göteborg, Göteborg, Sweden
Skjetne, E.	IFE Kjeller, Norway
Stüsser, N.	Hahn-Meitner Institute, Berlin, Germany
Takahashi, M.	CNRS, Strassbourg, France
Vives, E.	University of Barcelona, Barcelona, Spain
Vlak, W.	ECN Petten, The Netherlands
Weber, D.	Johannes Gutenberg Universität, Mainz, Germany
de Wijn, H.	FOM, Amsterdam, The Netherlands
Winkelmann M.	Hahn-Meitner Institute, Berlin, Germany
Yang T	AT& T Bell Laboratories, Murray Hill, New Jersey, USA
Österberg R.	Swedish Agricultural University, Uppsala, Sweden

3 PUBLICATIONS AND EDUCATIONAL ACTIVITIES IN THE DEPARTMENT

3.1 Publications

ALS-NIELSEN, J. and GREY, F. (1990). X-ray Reflectivity of a 200 Layer $W_{.25}Si_{.75}$ Multilayer Crystal. Risø-M-2846, 21 p.

ALS-NIELSEN, J. and KJÆR, K. (1990). X-ray Reflectivity and Diffraction Studies of Liquid Surfaces and Surfactant Monolayers. Phase Transitions in Soft Condensed Matter. NATO Advanced Study Institute on Phase Transitions in Soft Condensed Matter, Geilo, 4-14 April 1989. Riste, T. and Sherrington, D. (eds.), (Plenum Press, New York, 1989). (NATO Advanced Science Institutes Series B: Physics, 211) p. 113-138.

ALS-NIELSEN, J. and PEDERSEN, J. SKOV (1990). Synkrotronstråling (Synchrotron Radiation). In: C. Christensen, C. Clausen og B. Felsager: Fysikkens Spor (Tracks in Physics) (High School Text Book in Physics, Gyldendal), 182-183.

ANDERSEN, N.H., LEBECH, B. and POULSEN, H.F. (1990). Structural Phase Diagram and Equilibrium Oxygen Partial Pressure of $YBa_2Cu_3O_{6+x}$. Acta Cryst. A Suppl. **46**, C-321.

ANDERSEN, N.H. and KJEMS, J.K. (1990). De nye superledere (The New Superconductors). In: C. Christensen, C. Clausen og B. Felsager: Fysikkens spor (Tracks in Physics), (High School Text Book in Physics, Gyldendal), 102-103.

ANDERSEN, N.H., LEBECH, B. and POULSEN, H.F. (1990). Structural Phase Diagram and Equilibrium Oxygen Partial Pressure of $YBa_2Cu_3O_{6+x}$, J. Less-Common Metals **164** & **165**, 124-131.

ANDERSEN, N.H., LEBECH, B. and POULSEN, H.F. (1990). The Structural Phase Diagram and Oxygen Equilibrium Partial Pressure of $YBa_2CU_3O_{6+x}$ Studied by Neutron Powder Diffraction and Gas Volumetry, Physica C **172**, 31-42.

ANDREASSEN, H., BOHR, H., BOHR, J., BRUNAK, S., BUGGE, T., COTTERILL, R.M.J., JACOBSEN, C., KUSK, P., LAUTRUP, B., PETERSEN, S.B., SÆRMARK, T. and ULRICH, [illegible]. (1990). Analysis of the Secondary Structure of the Human Immunodeficiency Virus (HIV) Proteins p17, gp120, and gp41 by Computer Modeling Based on Neural Network Methods. Jour. Acquried Immune Deficiency Syndromes **3**, 615-622.

ANNILA, A. J., CLAUSEN, K. N., HAKONEN, P. J., LINDGÅRD, P.-A., LOUNASMAA, O. V., NUMMILA, K. K., OJA, A. S., SIEMENSMEYER, K., STEINER, M., TUORINIEMI, J. T., WEINFURTER, H. and VIERTIÖ, H. E. (1990). Neutron Diffraction Experiments on Ordered Silver Nuclei at Picokelvin Temperatures - A Feasibility Study. Risø-M-2874, 35 p.

ANNILA, A. J., CLAUSEN, K. N., LINDGÅRD, P.-A., LOUNASMAA, O. V., OJA, A. S., SIEMENSMEYER, K., STEINER, M., TUORINIEMI, J. T. and WEINFURTER, H. (1990). Nuclear Order in Copper: New Type of Antiferromagnetism in an Ideal fcc System. Phys. Rev. Lett. **64**, 1421-1424.

ANNILA, A. J., CLAUSEN, K. N., LINDGÅRD, P.-A., LOUNASMAA, O. V., OJA, A. S., SIEMENSMEYER, K., STEINER, M., TUORINIEMI, J. T. and WEINFURTER, H. (1990). Nuclear Order in Copper: New Type of Antiferromagnetism in an Ideal fcc System. Physica B **165&166**, 779-780.

ANNILA, A. J., CLAUSEN, K. N., LINDGÅRD, P.-A., LOUNASMAA, O. V., OJA, A. S., SIEMENSMEYER, K., TUORINIEMI, J. T. and WEINFURTER, H. (1990). Nuclear Antiferromagnetic Phases of Copper in a Field. Physica B **165&166**, 781-782.

ANNILA, A. J., CLAUSEN, K. N., OJA, A. S., SIEMENSMEYER, K., STEINER, M., TUORINIEMI, J. T. and WEINFURTER, H. (1990). Kinetics, Hysteresis and Nonadiabaticity of the Phase Transitions in the Nuclear Spin System of Copper. Physica B **165&166**, 783-784.

BERNASCONI, A., SLEATOR, T., POSSELT, D. and OTT, H.R. (1990). Dynamic Technique for Measurement of the Thermal Conductivity and the Specific Heat: Application to Silica Aerogels. Rev. Sci. Instrum. **61**, 2420-2426.

BOHR, H., BOHR, J., BRUNAK, S., COTTERILL, R.M.J., FREDHOLM, H., LAUTRUP, B. and PETERSEN, S.B. (1990). A Novel Approach to Prediction of the 3-dimensional Structures of Protein Backbones by Neural Networks. FEBS letters **261**, 43-46.

BOHR, J. (1990). Magnetic X-ray Scattering: A New Tool for Magnetic Structure Investigations. Jour. Magn. Magn. Mat. **83**, 530-534.

BOHR, J., BRODDIN, D. and LOISEAU, A. (1990). Homogeneous Nucleated Annihilation of the 2q Phase in $Cu_{.78}Pd_{.22}$., Phys. Rev. B **42**, 1052-1055.

BOHR, J., GIBBS, D. and HUANG, K. (1990). X-ray Diffraction Studies of the Magnetic State of Thulium. Phys. Rev. B **42**, 4322-4328.

CASTÁN, T. and LINDGÅRD, P.-A. (1990). n=1/4 Domain-Growth Universality Class: Crossover to the n=1/2 Class. Phys. Rev. B **41**, 2534-2536.

CHOU, H., SHAPIRO, S.M., LYONS, K.B., KJEMS, J. and RYTZ, D. (1990). Soft-Mode Behaviour and the Dipolar Glass Transition in $KTa_{1-x}Nb_xO_3$, Phys. Rev. B **41**, 7231-7234.

D'AMICO, K.L., BOHR, J., MONCTON, D.E. and GIBBS, D. (1990). Melting and Orientational Epitaxy in Argon and Xenon Monolayers on Graphite. Phys. Rev. B **41**, 4368-4376.

ELLEGAARD, O., SCHOU, J. and SØRENSEN, H. (1990). Sputtering of Volatile Solids from Nonoverlapping Solids, Europh. Lett. **12**, 459-464.

ELSENHANS, O., FURRER, A., CLAUSEN, K. N. and WALKER, E. (1990). Unusual Magnetic Behaviour of the Disordered Antiferromagnetic Compound $NdAl_{0.8}Ga_{1.2}$ Studied by Neutron Scattering. J. Phys.: Condens. Matter **2**, 4737-4746.

FEIDENHANS'L, R., GREY, F., JOHNSON, R.L., MOCHRIRE, S.G.J., BOHR, J. and NIELSEN, M. (1990). Chemisorption of Oxygen on Cu(110). Acta Cryst. A Suppl. **46**, C-374.

FEIDENHANS'L, R., GREY, F., JOHNSON, R.L., MOCHRIE, S.G.J., BOHR, J. and NIELSEN, M. (1990). Oxygen Chemisorption on Cu(110): A Structural Determination by X-ray Diffraction. Phys. Rev. B **41**, 5420-5423.

FEIDENHANS'L, R., GREY, F., NIELSEN, M., BESENBACHER, F., JENSEN, F., LÆGSGAARD, E., STENSGAARD, I., JAKOBSEN, K.W., NØRSKOV, J.K. and JOHNSON, R.L. (1990). Oxygen Chemisorption on Cu(110): A Model for the c(6x2) Structure. Phys. Rev. Lett. **65**, 2027-2030.

GREY, F. (1990). Broccolis, Cauliflowers and Minarets in *Characterising Complex Systems*, ed. H. Bohr, World Scientific Publ., Singapore, 209-214.

GREY, F., FEIDENHANS'L, R., SKOV PEDERSEN, J., NIELSEN, M. and JOHNSON, R. L. (1990). Pb/Ge(111)1 ×1: An Anisotropic Two-dimensional Liquid. Phys Rev B **41**, 9519-9522.

GREY, F., FEIDENHANS'L, R. ZEGENHAGEN, J., JOHNSON, R.L. and NIELSEN, M. (1990). Si(111)'5.6 × 5.6'-Cu: A Silicide Precursor. (PS-09.01.07). Acta Cryst. A Suppl. **46**, C-373.

GRÅBÆK, L., (1990) X-ray Diffraction Studies of Kr, Xe and Pb Inclusions in Aluminium. Ph. D. Thesis, Copenhagen University. Risø–M–2868, 99 p.

GRÅBÆK, L., BOHR, J., JOHNSON, E., JOHANSEN, A., SARHOLT-KRISTENSEN, L. and ANDERSEN, H.H. (1990). Superheating and Supercooling of Lead Precipitates in Aluminium. Phys. Rev. Lett. **64**, 934-937.

GÖBEL, H.D., KJÆR, K., ALS-NIELSEN, J. and MÖHWALD, H. (1990). Reorientation of Aliphatic Tails During the Photopolymerization of a Diacetylenic Lipid. Thin Solid Films (1989) **179**, 41-52.

JACQUEMAIN, D., GRAYER WOLF, S., LEVEILLER, F., LAHAV, M., LEISEROWITZ, L., DEUTSCH, M., KJÆR, K. and ALS-NIELSEN, J. (1990). Dynamics of Two-Dimensional Self-Aggregation, Pressure and pH Induced Structural Changes in a Fluorinated Amphiphile at Liquid-Air Interfaces. An X-ray Synchrotron Study. J. Am. Chem. Soc. **112**, 7724-7736.

JOHNSON, E., GRÅBÆK, L., BOHR, J., JOHANSEN, A., SARHOLT-KRISTENSEN, L. and ANDERSEN, H.H. (1990). Lead Inclusions in Aluminium. In Beam-Solid interaction: Physical Phenomena, MRS-Symposium Proceedings Vol. **157**, pp. 247-252, eds. Knapp, J.A., Børgesen, P. and Zuhr R.A. (Pittsburgh, PA 1990).

KEEN, D. A., McGREEVY, R. L., HAYES, W. and CLAUSEN, K. N. (1990). Structural Disorder in AgBr: Reverse Monte Carlo Analysis of Powder Neutron-Diffraction Data. Phil. Mag. Lett. **61**, 349-357.

KJÆR, K.(1990). Structural Studies of Langmuir Monolayers on Water. Acta Cryst. A **46**, C-373.

LANDER, G.H., BROOKS, M.S.S., LEBECH, B., BROWN, P.J., VOGT, O. and MATTENBERGER, K. (1990). Measurements of Giant Magnetic Anisotropy in a Uranium Compound, Appl. Phys. Lett. **57**, 989-991.

LEBECH, B. (1990). Neutron Scattering Facilities at Risø, Neutron News **1** (no. 2), 7-13.

LEBECH, B., WULLF, M., LANDER, G.H., REBIZANT, J., SPIRLET, J.C. and DELAPALME, A. (1990). Neutron Diffraqction Studies of the Crystalline and Magnetic Properties of UFe_2. J. Phys.: Condens. Matter (1989) **1**, 10229-10248.

LEVEILLER, F., JACQUEMAIN, D., LAHAV, M., LEISEROWITZ, L., DEUTSCH, M., KJÆR, K. and ALS-NIELSEN, J. (1990). Ion Induced Two-Dimensional Self-Aggregation of Monolayers; Direct Evidence for Ordered Counter-Ionic Layers. An X-ray Synchrotron Study. Acta Cryst. A **46**, C-373.

LINDGÅRD, P.-A. (1990). Kinetics of Slow Domain Growth in Complex Systems in *Characterising Complex Systems.* ed. H. Bohr, World Scientific Publ., Singapore, 28-33.

LINDGÅRD, P.-A. and CASTÁN, T. (1989). Kinetics of Slow Domain Growth in Complex Systems. Revista Brasileira Fisica **19**, 338-348.

LINDGÅRD, P.-A. and CASTÁN, T. (1990). Kinetics of Slow Domain Growth: the n=1/4 Universality Class. Phys. Rev. B **41**, 4659-4662.

LINDGÅRD, P.-A. and MOURITSEN, O.G. (1990). Fluctuation Effects in First order Phase Transitions: Theory and Model for Martensitic Transformation. Phys. Rev. B **41**, 688-703.

MORTENSEN, K., PFEIFFER, W., SACKMANN, E. and KNOLL, W., (1990). Structural Properties of a Licithin-Cholesterol System: Ripple Structure and Phase Diagram. Phase Transitions in Soft Condensed Matter. NATO Advanced Study Institute on Phase Transitions in Soft Condensed Matter, Geilo, 4-14 April 1989. Riste, T. and Sherrington, D. (eds.), (Plenum Press, New York, 1989) (NATO Advanced Science Institutes Series B: Physics, 211) p. 293-296.

MÖHWALD, H., KENN, R. M., DEGENHARDT, D., KJÆR, K. and ALS-NIELSEN, J. (1990) Partial Order in Phospholipid Monolayers. Physica A **186**, 127.

NØRLUND-CHRISTENSEN, A., KROGH-ANDERSEN, E.,KROGH-ANDERSEN, I.G., ALBERTI, G., NIELSEN, M. and LEHMANN, M.S. (1990). X-Ray Powder Diffraction Study of Layer Compounds. The Crystal Structure of α-$Ti(HPO_4)_2{*}H_2O$ and a Proposed Structure for γ-$Ti(H_2PO_4)(PO_4){*}2H_2O$, Acta Chem. Scand. **44**, 865-872.

NØRLUND-CHRISTENSEN, A. and LEBECH, B. (1990). Superconducting Cuprates and Related Oxides. II. Profile Refinement of Neutron Powder Diffraction Data, Acta Chem. Scand. **44**, 902-906.

PAP, S., SJÖBERG, B. and MORTENSEN, K., (1990). The H^+-Induced Dissociation of Human Plasma α_2-Macroglobulin. An Investigation Using Small-Angle Neutron Scattering and Test of Trypsin Binding Activity. Eur. J. Biochem. **191**, 41-45.

PATTERSON, C., McMORROW, D.F., GODFRIN, H., CLAUSEN, K.N. and LEBECH, B. (1990). Evidence for a Magnon Energy Gap in the Spin-Slip Phase of Holmium, J. Phys.: Condens. Matter **2**, 3421-3425.

PEDERSEN, J. SKOV, POSSELT, D. and MORTENSEN, K. (1990). Analytical Treatment of the Resolution Function for Small-Angle Scattering, J. Appl. Cryst. **23**, 321-333.

PETERSEN, S.B., BOHR, H., BOHR, J., BRUNAK, S., COTTERILL, R.M.J., FREDHOLM, H. and LAUTRUP, B. (1990) Neural Networks and Biological Sequences. Trends in Biotechnology, November 1990.

SHIRANE, G., ALS-NIELSEN, J., NIELSEN, M., TRANQUADA, J.M., CHOU, H., SHAMOTO, S. and SATO, M. (1990). Magnetic Correlations in $YBa_2Cu_3O_{6+x}$ at Superconducting Concentrations, Phys. Rev. B **41**, 6547-6552.

SIEMENSMEYER, K., KAKURAI, K., STEINER, M., JYRKKIÖ, T. A., HUIKU, M. T. and CLAUSEN, K. N. (1990). Neutron Scattering Investigation of the Ordered State of the Nuclear Spins in Cu at 60 nK. J. Appl. Phys. **67**, 5433-5435.

SMITH, H.G. , BERLINER, R., JORGENSEN, J.D., NIELSEN, M. and TRIVISONNO, J. (1990) Pressure Effects on the Martensitic Transformation in Metallic Lithium, Phys. Rev. B **41**, 1231-1234.

STENUM, B., ELLEGAARD, O., SCHOU, J. and SØRENSEN, H. (1990). Thickness Dependence of the Sputtering Yield from Solid Deuterium by Light keV Ions, Nucl. Instr. Method B **48**, 530-533.

WOLNY, J., PYTLIK, L. and LEBECH, B. (1990). A Continuous Transition from Twins to 'Quasi-Crystals'. J. Phys.: Condens. Matter **2**, 785-795.

WULFF, M., ERIKSSON, O., JOHANSSON, B., LEBECH, B., BROOKS, M.S.S., LANDER, G.H., REBIZANT, J., SPIRLET, J.C. and BROWN, P.J. (1990). Experiment and Theory of Actinide Intermetallic Magnetism: A Test Case of $NpCo_2$, Europhys. Lett. **11**, 269-274.

3.2 Conferences

ALMDAL, K., KOPPI, K.A., ROSEDALE, J.H., BATES, P.S. and MORTENSEN, K., The Order-Disorder Transition and Fluctuation Effects in Asymetric PEP-PEE Diblock Copolymers, Gordon Symposion on Polymeric Physics, Newport, R.I., USA (July).

ALS-NIELSEN, J., X-Ray Study of Liquid Surfaces. First Liquid Matter Conference, European Physical Society, Lyon, France (July).

ALS-NIELSEN, J., In-situ Studies of the Structure of Langmuir Films. Gordon Conference on Complex Fluids, Volterra, Italy (September).

ALS-NIELSEN, J., X-Ray and Neutron Scattering Methods in Soft Matter Sciences. IX Schuola Nazionale Cibernetica et Biofisica, Univ. of Ancona and Rome, Italy (September).

ANDERSEN, N.H., LEBECH, B., MANGELSCHOTS, I. and WISNIEWSKI, A., Neutron Powder Diffraction and Gas Volumetry Studies of the Crystal Structure and Oxidation Properties of $Nd_{1.85}Ce_{0.15}CuO_{4+y}$ (NCCO). Danish Physical Society, Spring Meeting, Nyborg, Denmark (May).

ANDERSEN, N.H., LEBECH, B., MANGELSCHOTS, I. and WISNIEWSKI, A., Neutron Powder Diffraction and Gas Volumetry Studies of the Crystal Structure and Oxidation Properties of $Nd_{1.85}Ce_{0.15}CuO_{4+y}$. Powder Diffraction, Satellite Meeting of the XVth Congress and General Assembly of the International Union of Crystallography, Toulouse, France (July).

ANDERSEN, N.H., LEBECH, B. and POULSEN, H.F., Structural Phase Diagram, Oxygen Diffusion and Equilibrium Pressure of $YBa_2Cu_3O_{6+x}$. Danish Physical Society, Spring Meeting, Nyborg, Denmark (May).

ANDERSEN, N.H., LEBECH, B. and POULSEN, H.F., Structural Phase Diagram and Equilibrium Oxygen Partial Pressure of $YBa_2Cu_3O_{6+x}$. E-MRS 1990 Spring Conference, Strassbourg, France (May-June).

ANDERSEN, N.H., LEBECH, B. and POULSEN, H.F., Structural Phase Diagram and Equilibrium Oxygen Partial Pressure of $YBa_2Cu_3O_{6+x}$. XVth Congress and General Assembly of the International Union of Crystallography, Toulouse, France (July).

ANDERSEN, N.H., LEBECH, B. and POULSEN, H.F., Study of the Structural Phase Diagram, Oxygen Bulk In-Diffusion, and Equilibrium Partial Pressure of $YBa_2Cu_3O_{6+x}$. 3rd International Symposium on Superconductivity (ISS'90), Sendai, Japan (November).

BAUER, R., HANSEN, S., BEHAN, M., JONES, G., MORTENSEN, K. and SÆRMARK, T., Small-Angle Scattering Studies on Coated Microvesicles. VIII International Meeting on Small-Angle Scattering, Leuven, Belgium (August).

BERNASCONI, A.,SLEATOR, T., POSSELT, D. and OTT, H.R., Influence of Oxidation and of H_2-Exchange Gas on the Thermal Properties of Silica Aerogels. International Conference on Low-Temperature Physics LT-19, Brighton, U.K. (August).

BOHR, J., Epitaxial Clusters in Single Crystal Host. 5th International Symposium on Small Particles & Inorganic Clusters. Konstanz, Germany (September).

BOHR, J., Magnetism and Synchrotron Radiation. Annual meeting of the German Neutron Scattering Society, Berlin, Germany (October).

BOHR, J., BRODDIN, D. and LOISEAU, A., Homogeneous Annihilation of the 2q Phase in $Cu_{.78}Pd_{.22}$. 10th General Conference of the Condensed Matter Division of the European Physical Society, Lisbon, Portugal (April).

BOHR, J., BRODDIN, D. and LOISEAU, A., Homogeneous Annihilation of the 2q Phase in $Cu_{.78}Pd_{.22}$. Spring Meeting, Nyborg, Denmark (May).

BOHR, J., GRÅBÆK, L., ANDERSEN, H.H., JOHANSEN, A., JOHNSON, E. and SARHOLT-KRISTENSEN, L. Krypton Inclusions in Aluminium Studied by X-ray Diffraction. Fundamental Aspects of Inert Gases in Solids. NATO Advanced Research Workshop, Bonas, France (September).

CASTÁN, T. and LINDGÅRD, P.-A. Pinning Effects on Domain Growth: A Monte Carlo Simulation Study. The Danish Physical Society Spring Meeting (May).

CLAUSEN, K.N., The Risø Cold Source. International workshop on Cold Neutron Sources. Los Alamos, New Mexico, USA (March).

ELDRUP, M., PEDERSEN, J. SKOV, HORSEWELL, A., JENSEN, K. O. and EVANS, J. H., Comparison of Results from Different Experimental Techniques (SANS, TEM, PAT, SEM) Applied to Bulk Cu and Ni Containing Krypton. Fundamental Aspects of Inert Gases in Solids. Nato Advanced Research Workshop. Bonas, France (September).

ELLEGAARD, O., SCHOU, J., STENUM, B., SØRENSEN, H. and PEDRYS, R., Energy Distributions and Sputtering Yields from Subspikes in Ion-Bombarded Volatile Solids. IISC 8, 8th International Workshop on Inelastic Ion Surface Collisions. Wr. Neustadt, Austria (September).

ELLEGAARD, O., SCHOU, J., SØRENSEN, H. and STENUM, B., Sputtering of Volatile Solids from Nonoverlapping Subspikes. Danish Physical Society, Spring Meeting, Nyborg, Denmark (May).

FALCÃO, A.N. and MARGAÇA, F.M.A., Neutron Guides and Small-Angle Neutron Scattering. A Simulation Study. VII National Physics Conference, Lisbon, Portugal (September).

FEIDENHANS'L, R., Surface Structure Determination Using Synchrotron X-rays. Complementary Applications of Diffraction by Neutrons and X-ray Synchrotron Radiation. International Satellite Conference of the IUCr XVth Congress. Alpe d'Huez, France (July).

FEIDENHANS'L, R., Structure of Oxygen on Cu Surfaces. Workshop at the 3rd Topsøe Summer School on Surface Science, Danish Technical University, Denmark (August).

FEIDENHANS'L, R., GREY, F., JOHNSON, R.L., MOCHRIE, S.G.J., BOHR, J. and NIELSEN, M., Chemisorption of Oxygen on Cu(110). XVth Congress and General Assembly. International Union of Crystallography, Bordeaux, France (July).

GREY, F., Two-dimensional Liquid Pb Studied by X-ray Diffraction. HASYLAB Annual Users Meeting, Hamburg, Germany (January).

GREY, F., Epitaxial Rotation and Rotational Phase Transitions. NATO Summer School on Phase Transitions in Thin Films, Erice, Italy (June).

GREY, F., The Commensuration of Surface Structures Studied by Surface X-ray Diffraction. Yamada Conference on Surface as a New Material, Osaka, Japan (July).

GREY, F., Surface X-Ray Diffraction Studies at HASYLAB. The Photon Factory, Tsukuba, Japan and the Electrotechnical Laboratory, Tsukuba, Japan (July).

GREY, F., A Symmetry Principle for Epitaxial Rotation. Workshop at the 3rd Topsøe Summer school on Surface Science, Danish Technical University, Denmark (August).

GREY, F., FEIDENHANS'L, R., ZEGENHAGEN, J., JOHNSON, R.L. and NIELSEN, M., Si(111)'5.6x5.6'-Cu: A Silicide Precursor. XVth Congress and General Assembly. International Union of Crystallography. Bordeaux, France (July).

GRÅBÆK, L., BOHR, J., JOHNSON, E., ANDERSEN, H.H., JOHANSEN, A. and SARHOLT-KRISTENSEN, L., X-ray Scattering from Facets at Lead Precipitates in Aluminium. Danish Physical Society, Spring Meeting, Nyborg, Denmark (May).

GRÅBÆK, L., BOHR, J., JOHNSON, E., ANDERSEN, H.H., JOHANSEN, A. and SARHOLT-KRISTENSEN, L., X-Ray Studies of the Melting of Lead Precipitates in Aluminium. Fundamental Aspects of Inert Gases in Solids. NATO Advanced Research Workshop, Bonas, France (September).

HANSEN, S. and PEDERSEN, J. SKOV, A Comparison of Three Different Methods for Indirect Fourier Transformation. VIII International Meeting on Small-Angle Scattering. Leuven, Belgium (August).

HOWARD, B.K. and BOHR, J., Magnetic Structures of the Rare Earth Alloy HoEr. Danish Physical Society, Spring Meeting, Nyborg, Denmark (May).

KJÆR, K., Structural Studies of Langmuir Monolayers on Water. XVth Congress of the International Union of Crystallography, Bordeaux, France (July).

KJÆR, K., The Structure of Amfiphilic Monolayers on Water. MODECS Internatmøde om "Grænsefladestruktur og Grænsefladeegenskaber" (Interfacial Structures and Interfacial Properties). Roskilde, Denmark (September).

KJÆR, K., ALS-NIELSEN, J., KENN, R. M., BÖHM, C., TIPPMANN-KRAYER, P., PETERSON, I. R., BIBO, A. M., HELM, C. A., MÖHWALD, H., LEVEILLER, F., JACQUEMAIN, D., WEINBACH, S., LEISEROWITZ, L. and DEUTSCH, M., X-Ray Scattering Studies of Fatty Acid Films on Water and on $CdCl_2$ Solutions. Third European Conference on Organized Organic Thin Films, Mainz University, Germany (October).

KROMANN, R., FOSSUM, J., ANDERSEN, N.H., FRELTOFT, T. and VASE, P., Measurements of Texture in YBACUO Thin Films. Danish Physical Society, Spring Meeting, Nyborg, Denmark (May).

KROMANN, R., de REUS, R., BILDE-SØRENSEN, J., ANDERSEN, N.H., FRELTOFT, T. and VASE, P., Study of Microstructure in Laser Ablated YBCO Thin Films. Danish Physical Society, Solid State Section, Topical Meeting on High Temperature Superconductivity, The Technical University of Denmark, Lyngby, Denmark (December).

LANDER, G.H., BROOKS, M.S.S., LEBECH, B., BROWN, P.J., VOGT, O. and MATTENBERGER, K., Measurements of Anisotropy Constant in US with Polarised Neutrons. 35th Annual Conference on Magnetism and Magnetic Materials, San Diego, California, U.S.A. (October).

LEBECH, B., WULFF, M. and LANDER, G.H., Spin and Orbital Moments in Actinide Compounds. 35th Annual Conference on Magnetism and Magnetic Materials, San Diego, California, U.S.A. (October).

LINDGÅRD, P.-A., Theory of the Magnetic Ordering in Cu in a Field: an Ideal Frustrated Antiferromagnet. International Conference on Magnetic Phase Transition, Osaka, Japan (April).

MARGAÇA ,F.M.A., FALCÃO, A.N., SEQUEIRA, A.D. and SALGADO, J.F., Optical Effects on Neutron Guide Tubes. VIII International Meeting on Small Angle Scattering, Leuven, Belgium (August).

MORTENSEN, K., Micro-Phase Separation in Bilayer Membranes. NATO and CEC Advanced Research Workshop, Cargese, France (September).

MOURITSEN, O.G., SHAH, P.J., ANDERSEN, J.V., POULSEN, H.F. and BOHR, H., Computor Simulations of Phase Separation and Ordering Processes in Low-Dimensional Systems. IV Nordic Symposion on Computor Simulations in Natural Sciences, Sandefjord, Norway (August).

PEDERSEN, J. SKOV and ELDRUP, M., A Small Angle Neutron Scattering Study of Krypton Precipitates in Copper. Danish Physical Society. Spring Meeting. Nyborg, Denmark (May).

PEDERSEN, J. SKOV and ELDRUP, M., A Small Angle Neutron Scattering Study of Krypton Precipitates in Copper. Short Range Order in Ill-Ordered Materials. INSTN-CEN, Saclay, France (July).

PEDERSEN, J. SKOV, POSSELT, D. and MORTENSEN, K., Analytical Treatment of the Resolution Function for Small-Angle Scattering. VIII International Meeting on Small-Angle Scattering. Leuven, Belgium (August).

PEDERSEN, J. SKOV and RIEKEL, C., Resolution Function for Small-Angle X-ray Scattering Calculated Using Gaussian Approximations in Position-Angle-Wavelength Space. VIII International Meeting on Small-Angle Scattering. Leuven, Belgium (August).

POSSELT, D., Properties and Characterization of Silica Aerogel, 6.th Danish Meeting on Zeolites. Odense University, Denmark (April).

POSSELT, D., KJEMS, J.K., BERNASCONI, A., SLEATOR, T. and OTT, H.R., Low Temperature Thermal Properties of Silica Aerogel. Danish Physical Society, Spring Meeting, Nyborg, Denmark (May).

POULSEN, H.F., ANDERSEN, N.H., ANDERSEN, J.V., BOHR, H. and MOURITSEN, O.G., Dynamic Scaling of Oxygen Ordering in $YB_2Cu_3O_{7-x}$. Danish Physical Society, Solid State Section, Topical Meeting on High Temperature Superconductivity. The Technical University of Denmark, Lyngby, Denmark (December).

SCHERRENBERG, R.L., REYNAERS, H.R., VLAK, W.A.H.M., MORTENSEN, K. and GONDARD, C., Small-Angle Scattering on Poly(Vinylchloride). VIII International Meeting on Small-Angle Scattering. Leuven, Belgium (August).

SCHOU, J., SØRENSEN, H., STENUM, B. and ELLEGAARD, O., Sputtering Yields and Energy Distributions from Nonoverlapping Subspikes in Ion-Bombarded Volatile Solids. The Gordon Conference on Particle-Solid Interactions, Plymouth, New Hampshire, U.S.A. (July).

SCHOU, J., STENUM,B., ELLEGAARD, O., SØRENSEN, H. and PEDRYS, R., Sputtering of Frozen Gases by Particle Bombardment. IISC 8, 8th International Workshop on Inelastic Ion Surface Collisions. Wr. Neustadt, Austria (September).

SLEATOR, T., BERNASCONI, A., FELDER, E., POSSELT, D. and OTT, H.R., Specific Heat of Silica Aerogels at Very Low Temperatures. International Conference on Low-Temperature Physics LT-19,Brighton, U.K. (August).

STENUM, B., SCHOU, J., SØRENSEN, H. and GÜRTLER, P., Luminescence from Pure and Impure Solid Hydrogens. Danish Physical Society, Spring Meeting, Nyborg, Denmark (May).

STENUM, B., SCHOU, J., SORENSEN, H. and ELLEGAARD, O., Electronic Sputtering of Thin Volatile Films on Metals. 3rd Topsøe Summer School, Technical University of Denmark, Lyngby, Denmark (August).

VAKNIN, D., KJÆR, K., ALS-NIELSEN, J. and LÖSCHE, M., A Neutron Reflectometer for Gas-Liquid Interface Studies. Third European Conference on Organized Organic Thin Films, Mainz University, Germany (October):

VIVES E. and LINDGÅRD P.-A. Melting of a Surface Layer and the Influence of a Substrate Interaction. The Danish Physical Society Meeting, Nyborg, Denmark (May).

VIVES, E. and LINDGÅRD, P.-A. Substrate Influence in Two Dimensional Solids and Liquids: a Monte Carlo Simulation Study. The Nordic Symposium on Computer Simulation in Natural Science, Oslo, Norway (August).

ÖSTERBERG, R., BOIVE, T., MALMENSTEN, B., NILSSON, U., STIGBRAND, T. and MORTENSEN, K., Intramolecular Movement in Complement Proteins. A Small-Angle Scattering Study Using Monoclonal Antibodiesas Markers. VIII International Meeting on Small-Angle Scattering. Leuven, Belgium (August).

3.3 Lectures

ALS-NIELSEN, J., Liquid Surfaces Studied by Synchrotron X-Ray Spectrometry University Dortmund, F.R.G. (June).

ALS-NIELSEN, J., Synchrotron Radiation and Condensed Matter Physics, a Survey. Præsentationsmøde af synkrotronstråleforskning (Science Research Council Introduction Meeting on Synchrotron Radiation Research). Niels Bohr Institute, Roskilde, Denmark (February).

ANDERSEN, N.H., Superconductivity and Oxygen Phase Properties of $YBa_2Cu_3O_{6+x}$. Workshop on Oxygen in Ceramic High-T_c Superconductors. The Technical University of Denmark, Lyngby, Denmark (May).

ANDERSEN, N.H., Superledning ved høje temperaturer (Superconductivity at High Temperatures). High School Summer Course on Physics, Sorø, Denmark (June).

ANDERSEN, N.H., The Phases of $YBa_2Cu_3O_{7-x}$ for Varying x and Temperature Studied by Neutron Scattering. Danish Physical Society, Solid State Section, Topical Meeting on High Temperature Superconductivity, The Technical University of Denmark, Lyngby, Denmark (December).

BOHR, J., Prediction of the 3-Dimensional Structures of Proteins Using Neural Networks and a Novel Computational Folding Algorithm. AT & T Bell Laboratories, New Jersey, U.S.A. (January).

BOHR, J., Epitaxial Phenomena: 1. Inclusions - Melting Studies, 2. Rotations - A Geometrical Principle, University of Illinois at Urbana-Champaign, Illinois, U.S.A. (July).

BOHR, J., Epitaxial Phenomena: 1. Inclusions - Melting Studies, 2. Rotations - A Geometrical Principle, Advance Photon Source Project, Argonne National Laboratory, Chicago, U.S.A. (July).

BOHR, J., X-Rays and Magnetic Structures; and Physics of Inclusions. Præsentationsmøde af synkrotronstråleforskning (Science Research Council Introduction Meeting on Synchrotron Radiation Research). Niels Bohr Institute, Roskilde, Denmark (February).

CLAUSEN, K. N., Nuclear Magnetic Order in Cu: New Type of Antiferromagnetism in an Ideal fcc System. AT&T Bell Labs. Murray Hill, NJ, USA (March).

CLAUSEN, K. N., Nuclear Magnetic Order in Cu: New Type of Antiferromagnetism in an Ideal fcc System. NIST, Washington, USA (March).

CLAUSEN, K. N., Neutron Scattering Facilities and Research at Risø, Exemplified by a Study of Short Range Order and Diffusion in Fast Ion Conductors. Seminar über Kristall- und Strukturchemie, Institut für Anorganische Chemie Der Technische Hochschule, Aachen (June).

FEIDENHANS'L, R., A Model Catalyst: Oxygen on Copper. Præsentationsmøde af synkrotronstråleforskning (Science Research Council Introduction Meeting on Synchrotron Radiation Research). Niels Bohr Institute, Roskilde, Denmark (February).

GREY, F., Two-Dimensional Liquids. Præsentationsmøde af synkrotronstråleforskning (Science Research Council Introduction Meeting on Synchrotron Radiation Research). Niels Bohr Institute, Roskilde, Denmark (February).

KJÆR, K., Amphiplic Monolayers on Water. Præsentationsmøde af synkrotronstråleforskning (Science Research Council Introduction Meeting on Synchrotron Radiation Research). Niels Bohr Institute, Roskilde, Denmark (February).

KJÆR, K., Røntgenspredning fra Monomolekylære Film på Vandoverflader (X-Ray Scattering from Monomolecular Films on Water Surfaces). CISMI, University of Copenhagen, Denmark.

LEBECH, B., Magnetic Ordering in Iron Monogermanides. Charles University, Prague, Czechoslovakia (February).

LINDGÅRD, P.-A., Introduction to Winter School in Modern Physics, Copenhagen, Denmark (January).

LINDGÅRD, P.-A., Kinetics of Domain Growth in Quenches Across a First-Order Line in a Dipolar Coupled Model. Kyoto University, Japan (April).

LINDGÅRD, P.-A., New Universality Classes in Domain Growth. Kyushu University, Japan (April).

LINDGÅRD, P.-A., Magnetic Propertics of the Ideal fcc Antiferromagnet Cu at Nano Kelvin Temperatures. Institute Laue Langevin, Grenoble, France (May).

MORTENSEN, K., Neutron Scattering in Biophysics. Biological Physics Seminar Series, Technical university of Denmark, Lyngby, Denmark (February).

NIELSEN, M., Solid Surface Structures: Experimental Methods. Præsentationsmøde af synkrotronstråleforskning (Science Research Council Introduction Meeting on Synchrotron Radiation Research). Niels Bohr Institute, Roskilde, Denmark (February).

POSSELT, D., Low Temperature Properties of Silica Aerogel, Institut für Physik, Johannes Gutenberg-Universität, Mainz, Germany (July).

POSSELT, D., Low Temperature Thermal Properties of Silica Aerogel, Physikalisches Institut der Universität Würzburg, Germany (July).

POULSEN, H.F., Høj temperatur superledere. (High T_c Super Conductors). University Extension, Roskilde, Denmark (March).

3.4 Organization of Conferences, School

WINTER SCHOOL IN MODERN PHYSICS

29-30 January 1990, H. C. Ørsted Institute, Copenhagen.

The school offered a series of lectures, from neural networks to high T_c superconductivity, giving an elementary introduction to several very active fields of physics in which disorder and complexity play an essential role. There were six lecturers and 50 participants.

Organization/Commitee:

HEDEGÅRD, P., H. C. Ørsted Institute, Copenhagen, Denmark
LINDGÅRD, P.-A., Risø National Laboratory., Denmark.

COURSE IN SURFACE SCIENCE

R. FEIDENHANS'L together with J.K. Nørskov, I. Chorkendorff and K.W. Jakobsen from the Laboratory of Applied Physics, the Technical University (DtH) of Denmark, gave a course in Surface Physics at the DtH. The course consisted of two lectures of 70 minutes duration every week together with exercises. R. Feidenhans'l was lecturing four weeks in total eight lectures about Surface Crystallography, Phase Transitions at Surfaces, and Epitaxy and Growth.

NEUTRON SCATTERING MEETING AT RISØ

April 26, and 27 1990.

Within the 'Large Scale Installation Programme' the EEC has approved the project 'Cold Neutron Facilities at Risø'.

This project will make the neutron–scattering facilities at DR3 available to users from the ECC–countries. In this connection a meeting of potential users was held at Risø April 26 and 27, where the joint proposal to EEC was worked out. In total 32 scientists from the other EEC–countries participated. The programme for the meeting contained: 1) A presentation of the facilities at Risø, 2) The Scientific Program (shown below), which had the form of a seminar, where the participants presented their recent work and future experiments to be performed at the neutron–scattering instruments at Risø, and finnally 3) a Panel Discussion with the following subjects: 'Beam time administration', 'Special equipment', and 'Support for users'. During the meeting the participants completed their individual contributions to the application to EEC, which was later approved.

SCIENTIFIC PROGRAM

THURSDAY APRIL 26, 1990

9:15–9:45	Jørgen Kjems, Welcome. The present and future neutron scattering facilities at DR3.
9:15–9:45	Coffee break.
10:00–11:00	Visit to DR3 and the neutron guide hall.
11:00–12:00	Further discussion of the neutron scattering instruments.
12:00–13:00	Lunch at Risø.
13:00–15:00	Parallel sessions 1 and 2.
15:00–15:30	Coffee break.
15:30–17:30	Parallel sessions 1 and 2.

FRIDAY APRIL 27, 1990

9:15–10:30	Plenary session.
10:30–12:30	Panel discussion. Chairman: Professor A.R Mackintosh **Subjects:** The beam time administration. Program for special equipment (excl. diffractometers). Support for users, technical assistance, running expences etc.
12:30–13:30	Lunch at Risø.
13:30–15:00	This afternoon is devoted to work on completion of users part of application to EEC.
15:00	End of meeting.

SESSION 1	SESSION 2
Magnetism	**Non Magnetic Materials**
R.A Cowley Neutron Scattering from Rare Earth Metals	*S.J. Johnson* Specular Reflection of Neutron to Probe Phospholipid Structure
J. Bohr Magnetic Structures of Rare Earth Metals.	*E.L. Carbarcos* SANS Studies on Micellar Solutions of Undecylammonium Chloride in Presence of Sodium Chloride.
B.D. Rainford Magnetic Neutron Scattering from Rare Earth Alloys and Compounds.	*J.P. Bradshaw* Neutron Scattering Studies of Enveloped Virus Structure.
M. Loewenhaupt Magnetic Excitations in Low-Symmetry Systems.	*K. Mortensen* Phase Transitions in Bilayer Lamellar Lipid Membranes Incorporated with Cholesterol.
O. Moze Crystal-Field and Exchange Effects in Supermagnets.	*C.G. McCracken* Hydrogen Occlusion in Aluminium - Lithium Based Alloys.
G.H. Lander Neutron Experiments on Actinide Intermetallics	*R.L. McGreevy* Neutron Scattering Studies of Thermally Induced Disorder.
A. Loidl Itinerant Heavy-Fermion Magnetism.	*H.G. Brokmeier* Phase Development and Texture of Ti-Al at High Temperatures.
K.N. Clausen Nuclear Magnetism in Cu.	*P. Duran* Preparation and Microstructural Characterization in Superconducting Ceramics.
G.G. Lonzarich Highly-Correlated Electron Systems.	*P.J. Withers* Strain Measurements in Two Phase Metal Matrix Composites.
M. Steiner 1-D Magnets.	*S. Skolianos* Orientation of Fibres and Residual Stresses in Al-based Composites.
J.M. Coey Magnetic and Structural Properties of Interstitial Alloys.	*D. Juul Jensen* Texture Development in two Phase Metal Matrix Composites.
	F. Carsughi Investigation on He-bubbles Coarsening in Implanted Metals.

Bibliographic Data Sheet Risø-R-582

Title and author(s)

PHYSICS DEPARTMENT ANNUAL PROGRESS REPORT

1 January - 31 December 1990

Eds. J. Als-Nielsen, J. Skov Pedersen and B. Lebech

ISBN	ISSN
87-550-1703-7	0106-2840
	0107-8348

Dept. or group	Date
Physics Department	January 1991

Groups own reg. number(s)	Project/contract no.

Pages	Tables	Illustrations	References
127	9	79	104

Abstract (Max. 2000 char.)

Research in the Physics Department covers the field of condensed matter physics. The principal activities of the department are presented in this Progress Report for the period from 1 January to 31 December 1990.

The condensed matter physics research is predominantly experimental utilising diffraction of neutrons and X-rays. The research topics range from studies of two- and three-dimensional structures, magnetic ordering, heavy fermions, phase transitions in model systems to studies of texture and recrystallization kinetics with a more applied nature. In the field high T_c superconductors neutron and X-ray diffraction are used both for studying the basic mechanism responsible for the superconductivity and in the analysis of the solid state syntheses of the materials.

Descriptors INIS/EDB

MAGNETISM; PROGRESS REPORT; RISOE NATIONAL LABORATORY; SOLID STATE PHYSICS; SUPERCONDUCTIVITY

Available on exchange or request from:
Risø Library, Risø National Laboratory (Risø Bibliotek, Forskningscenter Risø)
P.O. Box 49, DK-4000 Roskilde, Denmark
Phone (+45) 42 37 12 12, ext. 2268/2269 · Telex 43 116 · Telefax (+45) 46 75 56 27

Sales distributors:
G.E.C. Gad Strøget
Vimmelskaftet 32
DK-1161 Copenhagen K, Denmark

Available on exchange from:
Risø Library,
Risø National Laboratory,
P.O. Box 49, DK-4000 Roskilde, Denmark
Phone +45 42 37 12 12 ext. 2268/2269
Telex 43 116, Telefax +45 46 75 56 27

ISBN 87-550-1703-7
ISSN 0106-2840
ISSN 0107-8348